TORNADOES IN THE BRITISH ISLES: CLIMATOLOGY, FORMATION ENVIRONMENTS, AND STORM DYNAMICS

A thesis submitted to the University of Manchester
for the degree of Doctor of Philosophy
in the Faculty of Engineering and Physical Sciences

2015

By
Kelsey J. Mulder
School of Earth, Atmospheric and Environmental Sciences

[Blank page]

Contents

Word Count: 43,716

List of Figures

Abstract

Tornadoes in the British Isles: Climatology, formation environments, and storm dynamics

Kelsey J. Mulder

A thesis submitted to the University of Manchester
for the Degree of Doctor of Philosophy, 2015

This thesis was funded by a scholarship from the Faculty of Engineering and Physical Sciences, University of Manchester and is presented in an alternative thesis format. The thesis consists of three separate journal articles which form a coherent research project.

Paper 1 is a climatology of tornadoes in the British Isles from 1980–2012. The climatology included interannual variability, seasonality, diurnal cycle, intensity, location of occurrence, sounding-derived environmental parameters, and parent storm types of tornadoes. One finding from Paper 1 was that the most common parent storm type in the British Isles was linear storms, for example, storms forming along cold fronts. This finding motivated Papers 2 and 3, which studied vortexgenesis in a tornadic narrow cold-frontal rainband (NCFR), a storm type common to the British Isles, which occurred 29 November 2011. This NCFR caused seven tornadoes across Wales and England. Paper 2 compares the differences in WRF simulation runs of the NCFR based on initialization time, planetary boundary layer scheme, microphysics scheme, and land surface scheme. Out of 96 simulations, the most realistic (most similar to observed radar reflectivity) run was chosen for a case study in Paper 3. Paper 3 analyzes vortices along the NCFR to determine mechanisms dominating their formation and maturation.

Declaration

The University of Manchester
PhD by published work Candidate Declaration

Candidate Name: Kelsey J. Mulder

Faculty: Engineering and Physical Sciences

Thesis Title: Tornadoes in the British Isles: Climatology, formation environments, and storm dynamics

Declaration to be completed by the candidate:

I declare that no portion of this work referred to in this thesis has been submitted in support of an application for another degree or qualification of this or any other university or other institute of learning.

Signed: Date: October 11, 2015

Copyright

Acknowledgements

I'd like to dedicate my thesis to Grandma Jeanne, Grandpa Mac, and Grandpa Rod, all who passed away during my PhD. I know you all would be so proud of me and, honestly, that kept me going through the hardest of times.

Thanks first and foremost to my supervisors Dave and Geraint for your patience, encouragement, critiques, and for looking at endless drafts of papers. Thanks also to my internal reviewer, Paul Connolly, for attending every viva and reading often lengthy end of year reports. Thanks Alan Blyth for serving as external reviewer. Thanks also to TORRO for graciously providing me with your data. Without you, this thesis wouldn't be possible. Thanks also to everyone in Simon 3.16 for your support and helping with the most inane tasks and solving ridiculous NCL, IDL, WRF, RIP, and general PhD problems. I am incredibly thankful to Mom, Dad, Steve, and all my friends (and their horses, dogs, cats, and hamsters) for supporting me, providing a good laugh, and allowing me a bit of a distraction when I needed it.

There is one friend I have to list by name because of her unsurpassed help. Jessica Erlingis, I don't think I could have done this without you. It was so nice to commiserate on PhD-related grievances and spend hours on Skype writing out equations, drawing diagrams, and generally discussing our research. I'm so lucky that you're going through your PhD at the same time as me. You've encouraged great ideas and have kindly helped me through PhD Panic because, fortunately or unfortunately, you're going through it at the same time.

For all my friends who wanted me to include weird words and phrases in my thesis, here you go:

- Creme de la creme
- Natitude

- Ginger
- Metamorphosis
- Splenetic
- Narwhal
- Uterus
- Gay marriage
- Poppycock
- Frabjous
- Tyrannosaurus Rex
- Cattywampus
- Plethora
- Longhorn
- Spongebob
- Discursive
- Cakes
- Antidisestablishmentarianism
- Peaches
- Shoe
- Efrain's

If your word/phrase isn't on that list, I'm afraid you'll have to keep reading. Also, you all owe me a beer.

Chapter 1

Introduction

Tornadoes have been reported on every continent except Antarctica (Snow and Wyatt, 1997; Goliger and Milford, 1998). The science of tornadoes has been well developed in the United States including storm morphologies (e.g., Gallus Jr. et al., 2008; Duda and Gallus Jr., 2009; Smith et al., 2012), techniques useful for forecasting (e.g., Rasmussen and Blanchard, 1998; Evans and Doswell, 2001; Shafer et al., 2009; Calhoun et al., 2014), storm dynamics (e.g., Fujita, 1955; Lemon and Doswell, 1979; Trapp and Weisman, 2003; Straka et al., 2007; Markowski et al., 2008; Markowski and Richardson, 2014), and modeling (e.g., Klemp and Rotunno, 1983; Lee and Wilhelmson, 1997b; Atkins and St. Laurent, 2009; Markowski and Richardson, 2014). The same level of progress has not been achieved in the British Isles, although efforts have been made with studies on tornadoes by creating climatologies (Lacy, 1968; Elsom and Meaden, 1984; Meaden, 1985a; Elsom, 1985; Reynolds, 1999; Tyrrell, 2003; Holden and Wright, 2004; Kirk, 2007, 2014), using observations to detail synoptic and mesoscale processes leading to tornadoes (e.g., Clark, 2009, 2011, 2012; Clark and Parker, 2014), and storm-scale model simulations to determine the origin of strong winds within vortices (e.g., Smart and Browning, 2009).

A tornado is "a rotating column of air, in contact with the surface, pendant from a cumuliform cloud, and often visible as a funnel cloud and/or circulating debris/dust at the ground" (Glickman, 2000). This definition, which points to cumuliform clouds as the source of tornadoes, requires that tornadoes form from deep, moist convection. Deep, moist convection requires three ingredients: moisture, lift, and instability, or the rapid decrease of temperature with height

(Doswell et al., 1996). Two further ingredients are necessary for producing tornadoes. The first is a low cloud base. A low cloud base is a proxy for moisture. Additionally, a funnel cloud from a low cloud base is more likely to reach the ground, therefore becoming a tornado by definition, than a funnel cloud from a higher cloud base, which has a greater vertical distance to travel. The second necessary ingredient for producing tornadoes is wind shear, or the change of wind speed and direction with height. Change of wind speed with height creates horizontal rotation, known as horizontal vorticity. Change of wind direction with height creates vertical rotation, known as vertical vorticity. This preexisting vorticity is required to form tornadoes by processes described later in this chapter.

The ingredients required for tornado production are the same everywhere. However the magnitude of each of the ingredients can differ depending on any given location's climate. A common way of comparing tornadic environments is the CAPE (convective available potential energy, used as a measure of instability)–shear parameter space. The CAPE–shear parameter space has been used as a forecasting tool in the United States (Johns and Doswell, 1992). For example, supercells (storm with a persistent, rotating updraft) are favored in high-CAPE, low-shear and low-CAPE, high-shear environments (Weisman and Klemp, 1982). Tornadoes in the British Isles have been noted in low-CAPE, high-shear environments (e.g., Smart and Browning, 2009). Tornadoes occurring in low-CAPE, high shear environments have resulted in high false alarm rates (tornado warnings were issued, but no tornado occurred) for forecasters in the United States (Dean and Schneider, 2008). Further research on the magnitudes of the ingredients required to create tornadoes in different locations worldwide, for example low-CAPE, high-shear environments, will help increase understanding of tornadoes under all conditions and in all locations.

This thesis focuses on tornadoes in the British Isles, which, for our purposes, includes England, Scotland, Wales, Northern Ireland, The Republic of Ireland, Isle of Man, and Channel Islands. The remainder of this introduction will provide the background necessary to present my research questions. First, previous research on UK tornado environments is summarized. Second, a tornado classification system is introduced. Third, mechanisms leading to vortexgenesis for supercells, quasi-linear convective systems, and localized convective and shear vortices are discussed. Fourth, a brief introduction to the gaps in the research

on tornadogenesis in narrow cold-frontal rainbands is presented. Fifth, research questions and a description of the remaining chapters in this thesis are provided.

1.1 British Isles tornado environments

It is difficult to reliably remotely sense tornadoes. Although rotation within a storm can be detected by Doppler radar, not all of these rotations, or vortices, produce tornadoes. Additionally, the vortices must be located near the radar to be detected. Therefore, we rely on tornado reports submitted by trained spotters and the public. The Tornado and Storm Research Organisation (TORRO), founded in 1974, has collected these reports and has centuries of data. There are over 30 known tornadoes in the British Isles before 1660, the first being reported in 1054 AD (Rowe, 1999). Tornado reports have been collected to modern day, providing a vast database to help pinpoint when and where the British Isles are at risk for tornadoes.

Because tornado climatologies rely on tornado reports, there is a chance for tornado under- or overreporting. For example, in areas of low population density, there is a chance a tornado would not damage any structures or be seen by an observer. Therefore the tornado may go unreported. Conversely, it is possible for multiple reports to be submitted for the same tornado, resulting in overreporting. Another source of error in tornado reports is intensity. Tornado intensity can be estimated based on the damage by the tornado, but is inherently subjective. TORRO implemented the tornado intensity scale (T scale), which is based on the Beaufort wind scale and consists of eleven ratings, compared to the Fujita scale (F scale), which consists of six ratings (Meaden, 1985b; Elsom et al., 2001; Kirk, 2014). To convert between the F scale to the T scale, the following equation can be used, rounding down to the nearest integer: $F \approx 0.5T$ (Brooks and Doswell III, 2001; Meaden and Chatfield, 2007). Determining the intensity of tornadoes requires site-visits or assumptions based on damage photos, which leaves room for error. Analyzing many years of data and updating climatologies periodically helps increase confidence in trends of tornado occurrence in spite of potential tornado reporting errors.

Many tornado climatologies have been conducted previously in the British Isles: Lacy (1968, study period 1963–1966) and Meaden (1985a, study period 1970–1979) covering England, Scotland, and Wales; Elsom and Meaden (1984,

study period 1960–1982), Elsom (1985, study period 1950–1984), Reynolds (1999, study period 1960–1989), Holden and Wright (2004, study period 1995–1999), Kirk (2007, study period 1980–2004), and Kirk (2014, study period 1981–2010) covering the United Kingdom; and Tyrrell (2003, study period 1950–2001) covering Ireland. Studies with tornadoes before 1950 are not listed or summarized here because of increased reporting and recording errors. To summarize previous findings:

- The average annual number of tornadoes ranged from 10.3 (Tyrrell, 2003) to 47.2 (Kirk, 2014) per year. These numbers varied due to locations considered, years analyzed, and whether waterspouts were included.

- Spring and summer (Holden and Wright, 2004), summer and autumn (Elsom and Meaden, 1984; Tyrrell, 2003), autumn (Reynolds, 1999; Kirk, 2007, 2014), autumn and winter (Meaden, 1985a), and winter (Lacy, 1968) were cited as the seasons with the most tornadoes. These differences have to do with different time periods and areas covered as well as inclusion or exclusion of waterspouts.

- Tornado outbreaks of 10 or more tornadoes in one day were most common in autumn and winter (Elsom and Meaden, 1984; Elsom, 1985; Meaden, 1985a; Reynolds, 1999)

- Tornadoes occurred most frequently in the afternoon (Elsom and Meaden, 1984; Elsom, 1985; Meaden, 1985a; Reynolds, 1999; Tyrrell, 2003; Kirk, 2014).

- Between 1950–2010, tornadoes in the UK were between T0–T7 (F0–F3) in intensity (Elsom and Meaden, 1984; Meaden, 1985a; Reynolds, 1999; Tyrrell, 2003; Kirk, 2007, 2014). The strongest tornado known in the UK occurred in 1666 and is believed to be T8/9 (F4; Brown et al., 2012). In all studies analyzed, the most common intensity was T2 (F1) with over 90% of tornadoes being between T0–T3 (F0–F1) intensity (Elsom and Meaden, 1984; Meaden, 1985a; Reynolds, 1999; Tyrrell, 2003; Kirk, 2007, 2014).

- The spatial distribution of tornadoes in the British Isles was previously analyzed by determining frequencies by county or region (Elsom, 1985;

Reynolds, 1999; Holden and Wright, 2004; Kirk, 2007), plotting touchdown locations on a map (Elsom and Meaden, 1984; Tyrrell, 2003; Holden and Wright, 2004; Kirk, 2014), and plotting spatially smoothed gridded tornado frequencies (Meaden, 1985a). England was found to have the most tornadoes in the United Kingdom (Elsom and Meaden, 1984; Elsom, 1985; Meaden, 1985a; Reynolds, 1999; Holden and Wright, 2004; Kirk, 2007, 2014). Southern and eastern (Elsom, 1985; Elsom and Meaden, 1984; Reynolds, 1999; Meaden, 1985a; Kirk, 2007, 2014), northwestern (Elsom, 1985; Meaden, 1985a; Reynolds, 1999; Kirk, 2007), and central (Elsom and Meaden, 1984) England and southern Wales (Meaden, 1985a; Reynolds, 1999; Kirk, 2007) were cited as the most common locations for tornadoes to occur. Southeast and Northwest England were cited as having more strong (T3 or higher) tornadoes (Meaden, 1985a)

Previous climatologies concurred on the seasonality of outbreaks, diurnal occurrence of tornadoes, intensity, and spatial distribution of tornadoes. However, there has not been a gridded analysis of the locations most likely to experience tornadoes since the 1980's (Meaden, 1985a). There was also no consensus on the seasonality of tornadoes in the British Isles. Although Lacy (1968) and Holden and Wright (2004) examined the temperature, dew point, wind speed, wind direction, and pressure associated with tornado days in the British Isles, an environmental sounding analysis to determine the magnitude of the ingredients necessary for producing tornadoes has not been previously conducted. Anecdotally, there was evidence that most tornadoes in the British Isles, especially from outbreaks, formed from linear storms (Lacy, 1968; Elsom, 1985; Meaden, 1985a). However there has been no parent storm analysis in the British Isles to date, which would be useful from a forecasting perspective.

1.2 Tornado classification

Tornadoes are classified into three types, based on the type of storm from which they are produced: supercells (Type I from Fig. 1.1), quasilinear convective systems (QLCS, Type II from Fig. 1.1), and localized convective and shear vortices (Type III from Fig. 1.1) (Agee, 2014). A supercell is a storm with a persistent, rotating updraft. The QLCS category includes all storms with a linear or near-linear appearance such as squall lines, bows (a linear storm with segment bowing

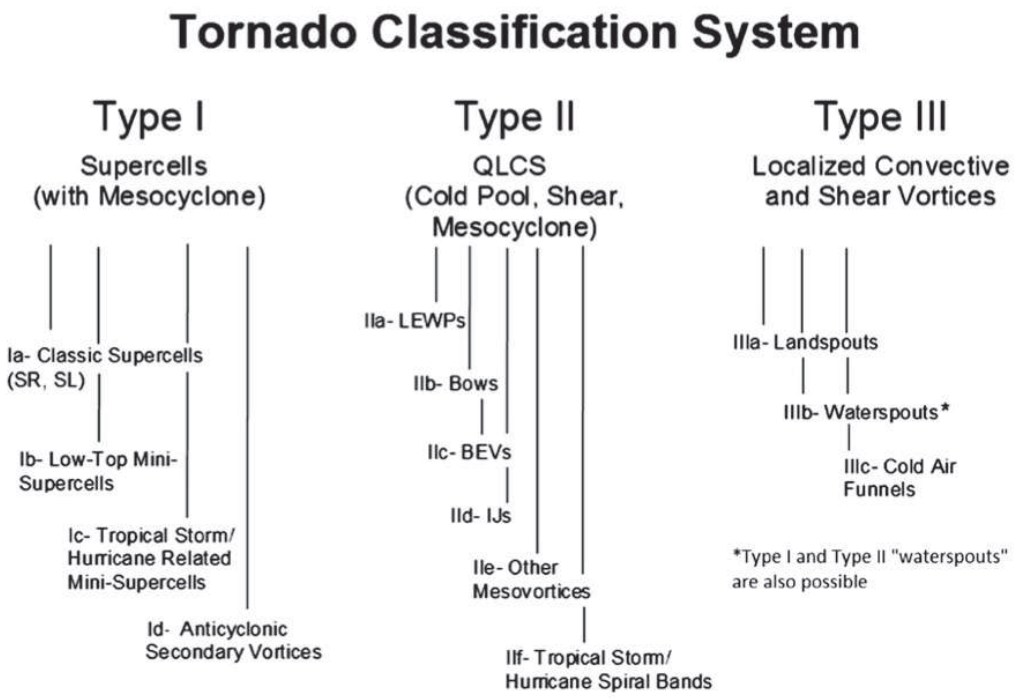

Figure 1.1: Taxonomy of tornado types. From Agee (2014)

forward), and narrow cold-frontal rainbands (Weisman and Davis, 1998; Agee and Jones, 2009). Localized convective and shear vortices, such as landspouts, are tornadoes not characterized as either supercell or QLCSs.

The reason for classifying tornadoes by parent storm type is because each type tends to produce different strengths of tornadoes, occur in different storm environments, and has different mechanisms of tornadogenesis (Agee and Jones, 2009). For example, tornadoes from supercells tend to produce more damage than those produced from QLCSs (Trapp et al., 2005; Agee and Jones, 2009; Grams et al., 2012). Localized convective and shear vortices tend to produce weak tornadoes (Agee and Jones, 2009). Discrete supercells tend to occur in higher CAPE environments than QLCSs (Thompson et al., 2012). Vortices in supercells typically descend from above and are detectable from radar data with greater lead-time than QLCS tornadoes, whose vortices ascend from the surface and provide a mean lead time of five minutes (Trapp et al., 1999). Therefore, from a forecasting perspective, there are different challenges in forecasting associated with differences in the classification of tornadoes. The processes leading to tornadogenesis in each tornado type is detailed in the sections below.

1.3 Supercell tornadogenesis

The process by which supercell tornadoes form requires three steps (Fig. 1.2 Davies-Jones, 2014; Markowski and Richardson, 2014). In the first step, the mesocyclone (a 2–10 km in diameter cyclonically rotating vortex with strongest vorticity located 3–7 km above ground) forms (labeled as the gray rounded arrows in Fig. 1.2a). Horizontal vorticity in the direction parallel to the low-level horizontal velocity (called streamwise vorticity, horizontal vorticity vector is shown as the white arrow at the surface with associated rotation shown as the yellow arrow in Fig. 1.2a), caused by vertical wind shear, is already present ahead of the developing supercell. This streamwise vorticity gets tilted upwards into vertical vorticity (the white vorticity vector along the red line in Fig. 1.2a becomes vertical) into the updraft (shown as the red line in Fig. 1.2a), causing the entire updraft to rotate (Markowski and Richardson, 2014, Fig. 1.2a). This tilting alone cannot cause a tornado because appreciable vertical vorticity does not occur close to the ground, as seen by the white vertical vorticity vector not becoming vertical in Fig. 1.2a until midlevels (Davies-Jones and Markowski, 2012; Markowski and Richardson, 2014). Even abrupt tilting of horizontal vorticity would cause deceleration before tilting. Therefore, not enough vertical vorticity would be available at the surface to form a tornado.

In the second step, downdraft air (shown as the blue line in Fig. 1.2a) acquires horizontal vorticity (the white line shows the vorticity vector along the blue downdraft air in Fig. 1.2a) due to a temperature gradient between cold air from the storm due to rain evaporating and hail and snow melting and warm environmental air (Dahl et al., 2014; Markowski and Richardson, 2014). As the downdraft air approaches the ground, the horizontal vorticity tilts upwards because of the surrounding wind, creating vertical vorticity near the ground (seen as the white vorticity vector tilts from horizontal into the vertical along the blue downdraft line in Fig. 1.2a). Near-surface vertical vorticity is required to produce a tornado.

In the third step, the cool, negatively buoyant downdraft parcels are stretched by perturbation pressure gradient force-induced suction, caused by the mesocyclone, increasing vertical vorticity by conservation of angular momentum (Markowski and Richardson, 2014, Shown as the pink arrows in Fig. 1.2b). Supercells with stronger mesocyclones and warmer downdrafts are more likely to cause tornadoes (Markowski and Richardson, 2014, Fig. 1.2b). Stronger mesocyclones (associated

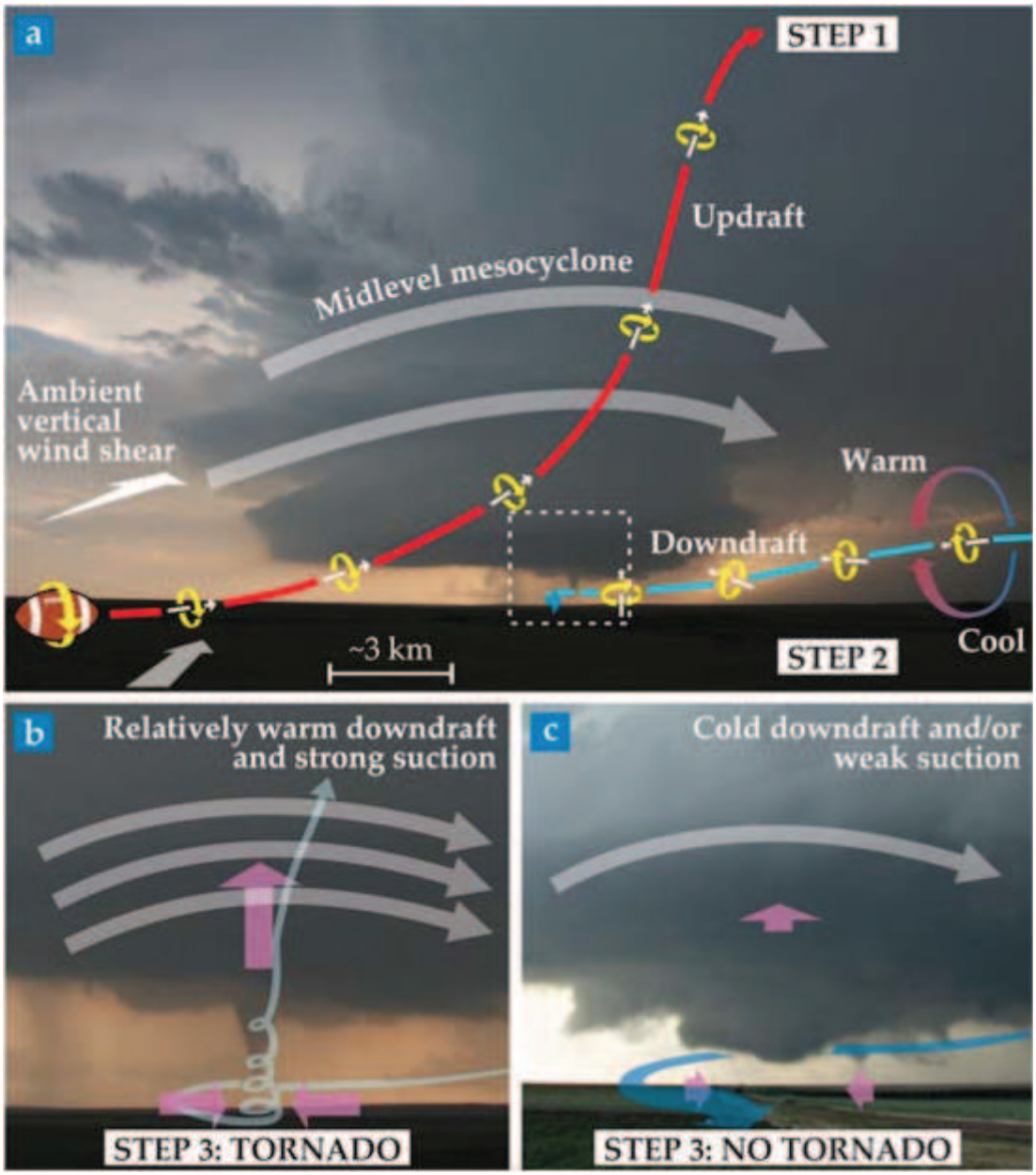

Figure 1.2: The three steps in the formation of supercell tornadoes. (a) Step 1: Horizontal streamwise vorticity (direction of the vorticity vector shown as white arrows, direction of spin shown in yellow arrows) is tilted into the vertical by the updraft (shown as the red line). This creates the rotating mesocyclone. Step 2: Baroclinically-induced horizontal vorticity is formed in downdraft and is tilted upwards as it moves toward the ground, forming near-surface vertical vorticity (blue line). (b) Step 3: In a supercell with a strong mesocyclone and relatively warm downdraft, perturbation pressure gradient-induced suction pulls parcels upwards, increasing vertical vorticity by conservation of angular momentum. This panel is zoomed in to the area of the white dashed box from (a). (c) If the supercell has a weak mesocyclone, it will have less suction. Additionally, cold downdraft air will be more negatively buoyant, therefore will take more energy to acquire upward motion. Both of these instances make tornadogenesis less likely. From Markowski and Richardson (2014)

with stronger vertical wind shear, shown as the gray arrows in Fig. 1.2b) produce more suction, therefore increasing the amount of vertical vorticity at the surface. Conversely, supercells with weaker mesocyclones (shown as the single gray arrow in Fig. 1.2c) are less likely to produce tornadoes. Warmer downdrafts produce parcels that are less negatively buoyant, and therefore are easier to accelerate vertically, thereby increasing vertical vorticity. However, there has to be enough temperature difference to create baroclinically-induced horizontal vorticity described in Step 2. Therefore the temperature of the downdraft cannot be too cold nor too warm (Markowski and Richardson, 2014).

1.4 QLCS tornadogenesis

There are different hypotheses for how vortices are formed in bow echoes, or bow-shaped lines of convection. One hypothesis is that horizontal vorticity is created by a temperature gradient between warm, environmental air and air cooled by evaporation and melting of rain and snow (Trapp and Weisman, 2003, vorticity shown as black, bold vortex lines in Fig. 1.3). This horizontal vorticity forms similarly to the second step of supercell tornadogenesis (Markowski and Richardson, 2014). The horizontal vorticity is tilted by the downdraft (black vectors), caused by the rain core (blue hatching), creating cyclonic (red orb and solid red line) and anticyclonic (purple orb and solid purple line) vertical vortices on the south and north sides of the downdraft, respectively (Fig. 1.3). After the vortices are formed, stretching of planetary vorticity enhances the cyclonic and reduces the anticyclonic vorticity (dashed red and purple lines in Fig. 1.3, respectively, Trapp and Weisman, 2003).

Another hypothesis of vortex formation is similar to the hypothesis proposed by Trapp and Weisman (2003). Preexisting horizontal vorticity (vortex lines and direction of rotation shown as yellow lines in Fig. 1.4) are either created by temperature gradients (Atkins and St. Laurent, 2009) or vertical shear (Weisman and Davis, 1998). The horizontal vorticity is then tilted upwards by an updraft (red lines in Fig. 1.4, Weisman and Davis, 1998; Atkins and St. Laurent, 2009). This process produces vortex couplets (green circles with direction of rotation shown by the green arrows in Fig. 1.4) with the anticyclonic vortex to the south of the downdraft and the cyclonic vortex to the north of the downdraft, opposite of the couplets presented by Trapp and Weisman (2003). This mechanism was mostly

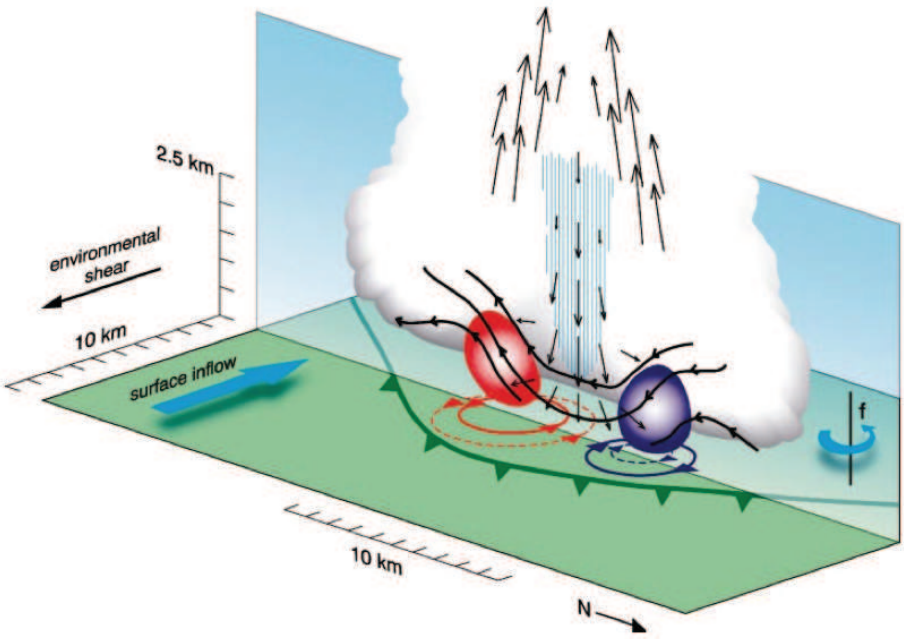

Figure 1.3: One hypothesis on formation of bow-echo vortices. Horizontal crosswise vorticity aloft (seen as the black, bold vortex lines) is tilted downward by the downdraft (black vectors) in the rain core (blue hatching), creating cyclonic (red orb and solid red line) and anticyclonic (purple orb and solid purple line) vortices. The vortex couplet straddles the downdraft along the gust front (barbed green line). Stretching of planetary vorticity enhances the cyclonic vorticity (dashed red line) and reduces the anticyclonic vorticity (dashed purple line). From Trapp and Weisman (2003).

seen early in the bow-echo life cycle in US bow echoes (Atkins and St. Laurent, 2009). A similar mechanism forming vortex couplets was found near simulated (Straka et al., 2007) and observed (Markowski et al., 2008) supercell low-level mesocyclones in the US with the cyclonic vortex being collocated with the hook echo (Straka et al., 2007; Markowski et al., 2008).

Another hypothesis of bow echo vortexgenesis produces only a cyclonic vortex rather than vortex couplets. Vorticity comes from two different sources. First, trajectories indicate that low-level warm air ahead of the front acquire horizontal streamwise vorticity from vertical wind shear and are tilted upwards into the vortex (not shown in Fig. 1.5), similar to Step 1 in supercell tornadogenesis (Markowski and Richardson, 2014). Additionally, horizontal vorticity (vortex lines and direction of rotation shown as yellow lines in Fig. 1.5) is generated

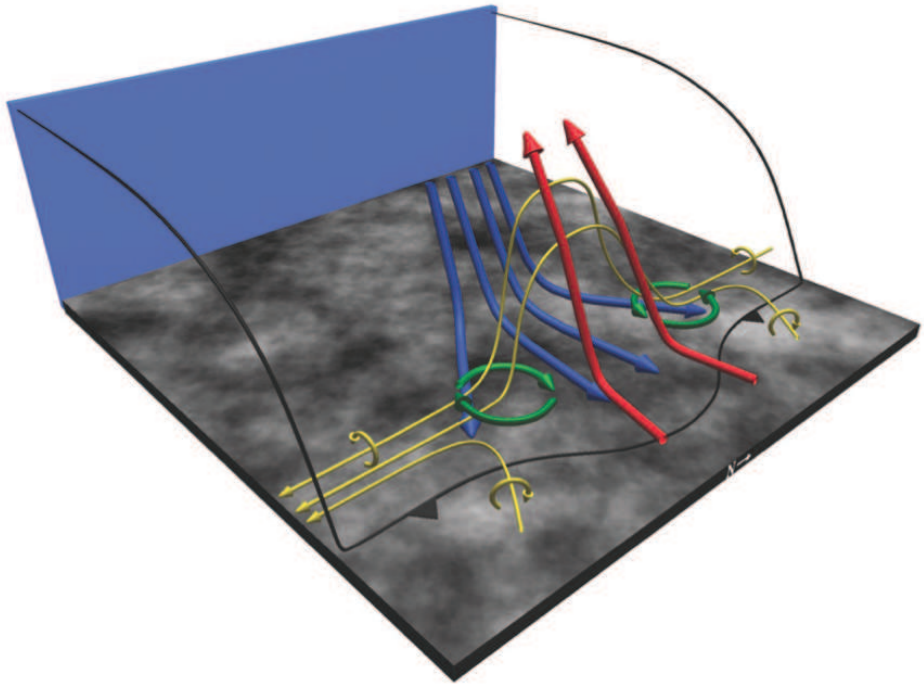

Figure 1.4: Bow-echo vortex couplet formation where the cyclonic vortex is located to the north and anticyclonic to the south. Southward pointing vortex lines (gold lines) behind the gust front (black barbed line) are tilted upwards by a localized updraft (red lines) straddling the downdraft (blue lines), therefore creating a cyclonic northern vortex and anticyclonic southern vortex (green circles). From Atkins and St. Laurent (2009).

due to temperature gradients in the downdraft, are tilted upwards by the updraft (Atkins and St. Laurent, 2009, updraft shown in red lines, resulting vertical vorticity shown as spiraling blue line in Fig. 1.5), similar to Step 2 in supercell tornadogenesis (Markowski and Richardson, 2014). Stretching by the updraft strengthens the vertical vorticity (Atkins and St. Laurent, 2009), similar to Step 3 in supercell tornadogenesis (not shown in Fig. 1.5, Markowski and Richardson, 2014).

1.5 Localized convective and shear vortices

In localized convective and shear vortices, the vortex formation is dictated by the up- or downdraft forming from non-supercell storms (or a storm without a persistent rotating updraft) or by preexisting shear. One mechanism by which

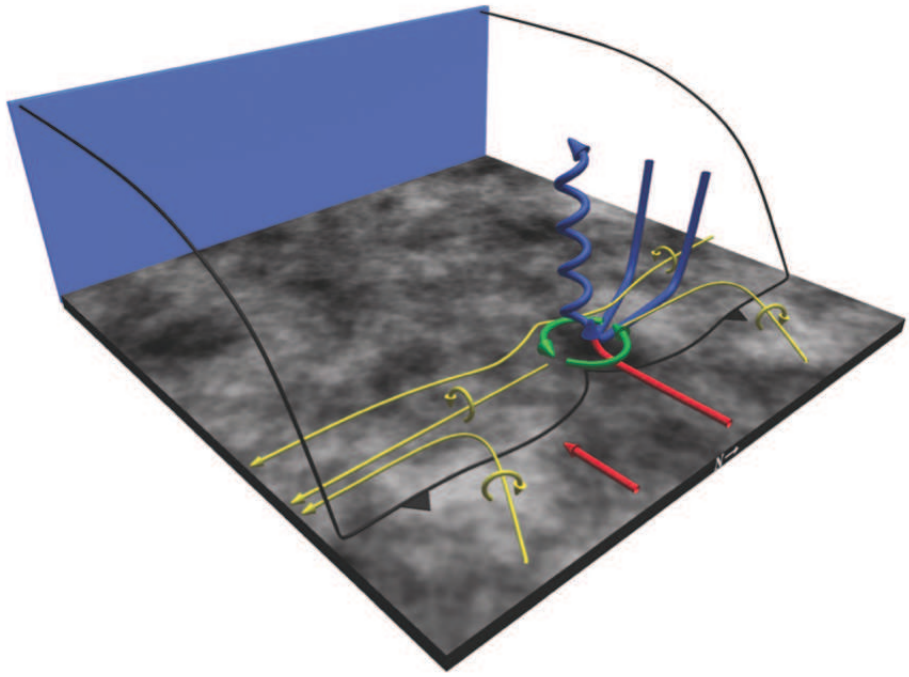

Figure 1.5: Another hypothesis on formation of bow-echo vortices, only producing a cyclonic vortex, similar to supercell tornadogenesis. Horizontal crosswise vorticity at low levels (shown as vortex lines in gold) in the downdraft (blue lines) are tilted upwards by the updraft (red lines) creating a vortex (green circle) along the gust front (black barbed line). Subsequent stretching by the updraft strengthens the vortex. From Atkins and St. Laurent (2009).

these tornadoes form is by stretching of preexisting vertical vorticity by an updraft early in the development of a thunderstorm by conservation of angular momentum (Brady and Szoke, 1989; Wakimoto and Wilson, 1989). Unlike for the hypotheses for both supercells and bow echoes, tornadogenesis in these shear vortices does not require tilting. Often, the preexisting vorticity is cited as being created by horizontal shearing instability (HSI; e.g., Wakimoto and Wilson, 1989; Lee and Wilhelmson, 1997b), or the concentration of vertical vorticity caused by perturbations (Glickman, 2000), discussed more below.

Vortex development by HSI has been described, using results from an idealized simulation, by Lee and Wilhelmson (1997b) as a six step process. First, the wind shift along a boundary, such as a surface cold front, provides a zone of horizontal shear known as a vertical vortex sheet. Second, the HSI rolls the vortex sheet into separate vortices because of inhomogeneities, such as lobe and

cleft instability (shown as the breaking waves along the line in Fig. 1.6 I), intersections of horizontal convective rolls with the cold front, friction, or temperature variations (Carbone, 1982; Lee and Wilhelmson, 1997b) along the line (vortices shown as black circles in Fig. 1.6 II). Third, the individual vortices interact and merge into larger vortices (Fig. 1.6 III). The individual larger vortices deepen as vorticity is advected upward by the vortex and storm updraft (shown as vertical black lines in Fig. 1.6 III). Fourth, the vortex strengthens to tornadic strength by stretching due to conservation of angular momentum (Fig. 1.6 IV). The vortices are maintained by vorticity advection and tilting of horizontal vorticity, but tilting of baroclinically-induced horizontal vorticity was not found to be a significant source of vortex production (Lee and Wilhelmson, 1997b). Fifth, cold pools (shaded area at the surface in Fig. 1.6 V) are formed due to evaporation of precipitation (hashed lines) and formation of a downdraft (downward pointing black lines in Fig. 1.6 V) and outflow increases convergence, thus increasing vortex stretching (Fig. 1.6V). Sixth, the tornado dissipates (shown as the slanted, spiral black lines in Fig. 1.6 VI) as the downdraft strengthens and the negatively buoyant cold pool surrounds the circulation, creating downward, diffluent motion (Fig. 1.6 VI).

Conversely to the model from an idealized simulation presented by Lee and Wilhelmson (1997b), real-data simulations (e.g., Wheatley and Trapp, 2008) and observations (e.g., Carbone, 1983) found that a vortex sheet was formed by the tilting of horizontal vorticity, not by preexisting vertical vorticity due to wind shear along a boundary. The vortex sheet was rolled up into vortices by HSI and the vortices were intensified by stretching, similar to the process hypothesized by Lee and Wilhelmson (1997b).

In idealized simulations, Lee and Wilhelmson (1997c) found that higher CAPE increased tornadic potential by encouraging stronger vortices, whereas Smart and Browning (2009) found no correlation between CAPE and circulation intensity. Narrow cold-frontal rainbands with larger forward motion (Clark, 2013; Clark and Parker, 2014), a larger temperature difference across the front (Clark, 2013), and larger horizontal wind shear across the front (Wakimoto and Wilson, 1989; Lee and Wilhelmson, 1997a; Kawashima, 2011; Clark, 2013; Clark and Parker, 2014) are more likely to produce tornadoes. The finding that increased horizontal wind shear across the line increases tornadic potential supports the notion that a vortex sheet caused by a wind-shift line plays a role in NCFR vortexgenesis.

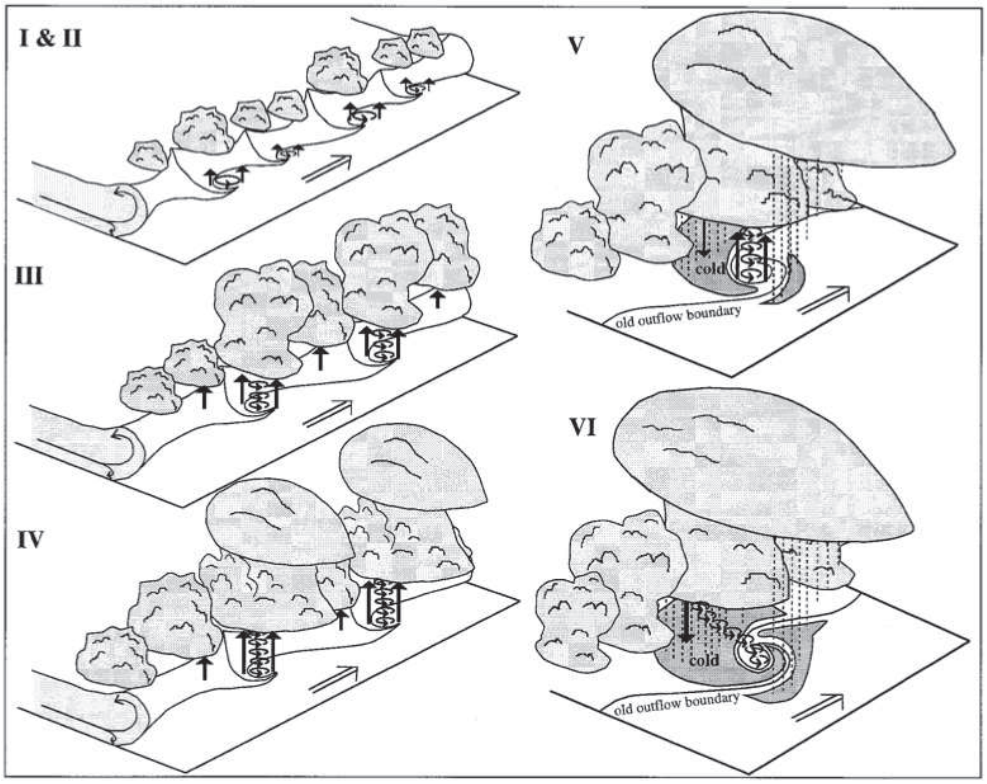

Figure 1.6: Schematic showing the hypothesis of nonsupercell vortexgenesis arising from horizontal shearing instability (HSI) with black lines showing horizontal and vertical motion. (I) and (II) Perturbations form along a vortex sheet (or transition zone of horizontal shear) along a surface boundary, such as a cold front, trigger HSI, which causes the vortex sheet to roll up into vortices. (III) The vortices interact and merge into larger vortices, deepening by vorticity advection. (IV) Stretching strengthens the vortices to tornadic strength. (V) A cold pool and downdraft form. (VI) The downdraft dominates storm motion and cold pool air surrounds circulation, dissipating the tornado (spiraling black lines). From Lee and Wilhelmson (1997b).

1.6 NCFRs

Narrow cold-frontal rainbands (NCFRs, Houze et al., 1976) have been associated with damaging winds and tornadoes (e.g., Smart and Browning, 2009; Clark and Parker, 2014). The linear nature of the convection suggests that NCFRs belong to the QLCS category of tornadoes. Many different radar reflectivity signatures have been associated with tornadoes along NCFRs such as hooks (radar reflectivity resembling a hook, e.g., Carbone, 1982; Clark, 2011, Fig. 1.7a), bulges or bow echoes (radar reflectivity with the center bulging or bowing ahead of

the rest of the line, e.g., Smart and Browning, 2009; Clark, 2011; Clark and Parker, 2014, Fig. 1.7b), and "core and gap" structure (two lines of higher radar reflectivity, separated by a gap, e.g., Hobbs and Persson, 1982; Jorgensen et al., 2003, Fig. 1.7c). Some of these reflectivity signatures are associated with different tornado types as listed above: hook echoes with supercells, bow echoes with QLCS, and core and gap with HSI and localized convective and shear vortices (Smart and Browning, 2009; Kawashima, 2011; Clark and Parker, 2014). The different reflectivity signatures associated with both NCFRs and other different storm types begs the question, what formation mechanism causes tornadoes in NCFRs?

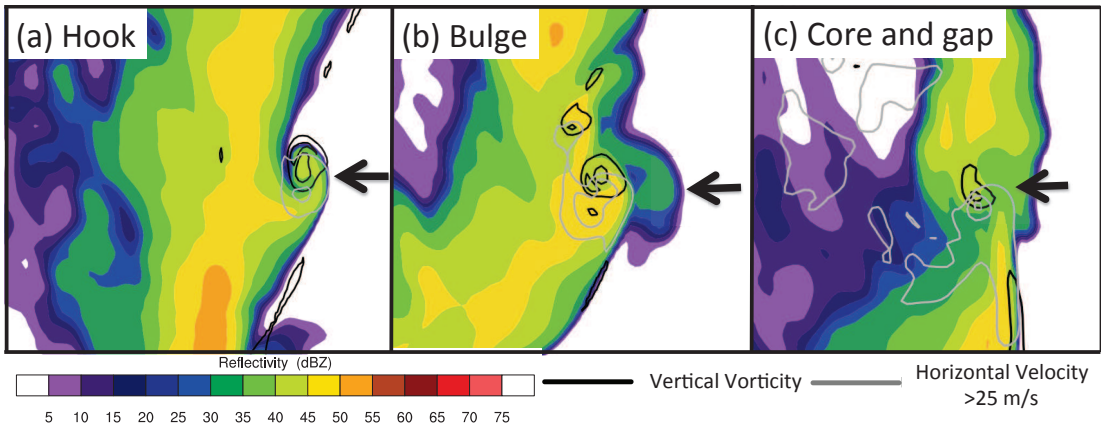

Figure 1.7: Modeled radar reflectivity (colored contours) showing examples of (a) a hook echo, (b) a bulge or bow echo, and (c) core and gap structure. Vertical vorticity (black contours) and horizontal vorticity (gray contours) are also shown. More details on the simulation and the results can be found in Chapter 4.

1.7 Research questions

There are a number of discrepancies or gaps in the literature presented above, which motivated the research questions investigated in this thesis. This section will detail the discrepancies, list the research questions, and outline the remainder of the thesis.

Although many previous tornado climatologies have been conducted in the British Isles, there is no consensus on the seasonality of tornadoes. Additionally, probability analysis of where and how likely tornadoes are to occur in the British

Isles has not been conducted since the 1980's (Meaden, 1985a). Additionally, a study using environmental soundings comparing tornadic and nontornadic environments has not been conducted in the British Isles. Finally, a tornado parent storm type analysis has not been conducted in the British Isles. To address these discrepancies, the following research questions are addressed in Chapter 2:

1. Where, when, and from what storm types do British Isles tornadoes form? What sounding parameters distinguish tornadic from nontornadic environments? Which areas of the British Isles are most susceptible to tornadoes?

Chapter 2, which is formatted as a journal-style paper, addresses these research questions by using tornado report data from 1980–2012 and details the probability of tornadoes spatially across the British Isles, interannual variability, annual and diurnal cycles of tornado activity, parent storm types of tornadic storms, and the environmental conditions derived from proximate soundings (such as instability and shear) of tornadic and nontornadic storms.

The results of Chapter 2 are useful for a variety of purposes. The spatial probability analysis of tornado occurrence is useful for understanding the most likely locations for tornado occurrences, which helps with public awareness, forecaster knowledge, and decision-makers such as insurance agencies. The interannual variability, annual, and diurnal cycles is similarly useful for awareness and preparedness. Parent storm and proximity sounding analyses are useful to help forecasters diagnose potentially tornadic environments.

Chapter 2 was published under the title, *Climatology, Storm Morphologies, and Environments of Tornadoes in the British Isles: 1980–2012* in the June 2015 issue of *Monthly Weather Review*. David Schultz is listed as co-author on Chapter 2. However, the work was all completed by me, under his guidance.

One finding from Chapter 2 was that linear storms, such as narrow cold-frontal rainbands, are the most common parent storm type for tornadoes in the British Isles. Additionally, it is tricky to predict where along these storms tornadoes will occur, making tornadoes produced by linear storms a challenging forecasting problem. Therefore, Chapters 3 and 4 focused on the dynamics of vortices along a narrow cold-frontal rain band that traversed northern Wales and England on 29 November 2011. Chapters 3 and 4 were based upon a simulation using the Advanced Research Weather and Forecasting Model (WRF-ARW, Skamarock et al., 2008).

When analyzing a case study, it is important to produce a realistic simulation, which begs the following research question:

2. Which initialization time and combination of parameterizations lead to the most accurate simulation of a modeled NCFR?

Therefore, Chapter 3 summarizes the results of 96 different combinations of planetary boundary layer scheme, microphysics scheme, land surface scheme, and initialization times for the 29 November 2011 narrow cold-frontal rainband to ensure the simulation in Chapter 4 was as close to reality as possible. Even though Chapter 3, *Sensitivity Tests of a WRF-Simulated Tornadic Narrow Cold-Frontal Rainband in the United Kingdom*, is formatted like a journal-style paper, is not intended for publication because it is provided as a technical document further explaining the methodology in Chapter 4. David Schultz is also listed as co-author for Chapter 3, but the work was completed by me, under his guidance.

Finally, because many radar reflectivity signatures, such as core and gap, hook, and bow echoes, have been associated with NCFR tornadoes and each of the signatures is associated with different hypotheses of vortexgenesis, it is unclear which hypothesis of vortexgenesis applies, especially in an NCFR exhibiting many of the reflectivity signatures listed above (e.g., Smart and Browning, 2009). Additionally, tilting has been noted as contributing to vortexgenesis and the generation of strong winds in NCFRs associated with HSI (e.g., Carbone, 1983; Smart and Browning, 2009), contrary to the model of HSI-induced vortices (Lee and Wilhelmson, 1997b). Therefore, Chapter 4 of this thesis addresses the following research questions:

3. What is the mechanism creating vortexgenesis in NCFRs with different radar reflectivity signatures? Is it possible for many mechanisms to be present? Could tilting also be involved in vortexgenesis with HSI present?

To address these research questions, Chapter 4, *The case for multiple growth mechanisms of vortices along a tornadic cold front*, analyzed the simulated narrow cold-frontal rainband chosen in Chapter 3. Vortices associated with a wave, hook, bowing segment, core and gap, and broken S radar reflectivity signatures were analyzed at vortexgenesis and at vortex maturity (when strongest horizontal winds occurred near the surface). Analysis includes cross sections and backwards trajectories to determine the magnitude of stretching and tilting required for both

vortexgenesis and vortex maturity. This study challenges previous conceptual models for vortexgenesis that suggest contrary vortexgenesis and vortex maturity mechanisms. Additionally, understanding the origin of vorticity in NCFR tornadoes may help future forecasts, especially in the British Isles, where tornadoes from this type of parent storm are common.

Chapter 4 is aimed to be published in *Monthly Weather Review*, but has not been submitted yet because I wanted comments from my internal and external reviewers first. Again, David Schultz is listed as co-author on Chapter 4. However, the work was all completed by me, under his guidance.

The thesis ends with Chapter 5, which summarizes the conclusions from Chapters 2, 3, and 4 and suggests future work.

Chapter 2

Paper 1: Climatology, Storm Morphologies, and Environments of Tornadoes in the British Isles: 1980–2012

[Blank page]

Climatology, Storm Morphologies, and Environments of Tornadoes in the British Isles: 1980–2012

KELSEY J. MULDER AND DAVID M. SCHULTZ

Centre for Atmospheric Science, School of Earth, Atmospheric and Environmental Sciences, University of Manchester, Manchester, United Kingdom

(Manuscript received 14 September 2014, in final form 12 December 2014)

ABSTRACT

A climatology is developed for tornadoes during 1980–2012 in the British Isles, defined in this article as England, Scotland, Wales, Northern Ireland, Republic of Ireland, Channel Islands, and the Isle of Man. The climatology includes parent storm type, interannual variability, annual and diurnal cycles, intensities, occurrence of outbreaks (defined as three or more tornadoes in the same day), geographic distribution, and environmental conditions derived from proximity soundings of tornadoes. Tornado reports are from the Tornado and Storm Research Organization (TORRO). Over the 33 years, there were a mean of 34.3 tornadoes and 19.5 tornado days (number of days in which at least one tornado occurred) annually. Tornadoes and tornado outbreaks were most commonly produced from linear storms, defined as radar signatures at least 75 km long and approximately 3 times as long as wide. Most (78%) tornadoes occurred in England. The probability of a tornado within 10 km of a point was highest in the south, southeast, and west of England. On average, there were 2.5 tornado outbreaks every year. Where intensity was known, 95% of tornadoes were classified as F0 or F1 with the remainder classified as F2. There were no tornadoes rated F3 or greater during this time period. Tornadoes occurred throughout the year with a maximum from May through October. Finally, tornadoes tended to occur in low-CAPE, high-shear environments. Tornadoes in the British Isles were difficult to predict using only sounding-derived parameters because there were no clear thresholds between null, tornadic, outbreak, and significant tornado cases.

1. Introduction

Although tornadoes in the British Isles have been labeled as ''freak'' occurrences by the media (Elsom 1985), the United Kingdom has been cited as having more tornadoes per area than any other country in the world (Reynolds 1999). In fact, over 30 tornadoes are known to have occurred in Britain before 1660 (Rowe 1999).

Deaths are not common in British Isles tornadoes (Elsom and Meaden 1984), but injuries and damage to property have been observed. For example, the F2 Birmingham tornado on 28 July 2005 resulted in 19 injuries and approximately £40 million ($68 million) in damages (Russell 2010). Because tornadoes pose a threat to human health and property, the knowledge of when, why, where, and under which conditions tornadoes occur has great relevance.

Although tornadoes have been reported on every continent except Antarctica, the conditions under which tornadoes are produced may not be the same everywhere (Brooks 2009). This makes tornado climatologies conducted in countries outside of the United States, for example, important. Temporal analysis of tornadoes has been conducted before in the British Isles (Table 1). These climatologies reported average annual occurrence of tornadoes ranging from 10.3 tornadoes per year (Ireland, 1999–2001; Tyrrell 2003) to 47.2 tornadoes and waterspouts per year (United Kingdom, 1981–2010; Kirk 2014). This statistic varies depending on the study period and whether waterspouts were included. This article updates the knowledge of tornado occurrence in the British Isles by using a 33-yr study period excluding waterspouts.

Another common analysis of the studies summarized in Table 1 was seasonality. The results depended on the

Denotes Open Access content.

Corresponding author address: Kelsey J. Mulder, Centre for Atmospheric Science, School of Earth, Atmospheric and Environmental Sciences, University of Manchester, Simon Building, Oxford Road, Manchester, M13 9PL, United Kingdom.
E-mail: kelsey.mulder@manchester.ac.uk

DOI: 10.1175/MWR-D-14-00299.1

TABLE 1. Selected results from previous tornado climatologies conducted in the British Isles.

Study	Location	Years	Avg annual No. of tornadoes	Avg annual No. of tornado days	Waterspouts included?	Tornado season	Season determined from tornado numbers or days?
Lacy (1968)	England, Scotland, and Wales	1963–66	19.5	9.0	No	Winter	Days
Elsom and Meaden (1984)	United Kingdom	1960–82	32.1	12.7	No	Summer and autumn	Days
Elsom (1985)	United Kingdom	1950–84	27.7	16.1	No	—	—
Meaden (1985a)	England, Scotland, and Wales	1970–79	≈ 32	18	Yes	Summer and autumn Autumn and winter	Days Numbers
Reynolds (1999)	United Kingdom	1960–89	33.2	15.8	No	Autumn	Numbers
Tyrrell (2003)	Ireland	1950–2001	10.3 (1999–2001)	—	No	Summer and autumn	Numbers
Holden and Wright (2004)	United Kingdom	1995–99	24.4	—	No	Spring and summer	Numbers
Kirk (2007)	United Kingdom	1980–2004	45.7*	22.6*	Yes	Autumn	Numbers
Kirk (2014)	United Kingdom	1981–2010	47.2 36.5	24.3 18.9	Yes No	Summer Autumn	Days Numbers
This article	British Isles	1980–2012	34.3	19.5	No	Summer Summer and autumn	Days Numbers

* Kirk (2007) originally reported a mean of 51.4 tornadoes and 24.2 tornado days per year. These numbers were revised to 45.7 tornadoes and 22.6 tornado days per year in Kirk (2014) after correcting database errors.

study period and whether tornado numbers or tornado days (number of days in which at least one tornado occurs) were used. The season with the most tornadoes has been cited as autumn (Reynolds 1999; Kirk 2007, 2014), summer and autumn (Tyrrell 2003), autumn and winter (Meaden 1985a), and spring and summer (Holden and Wright 2004). Using tornado days, tornado season has been cited as winter (Lacy 1968), summer and autumn (Elsom and Meaden 1984; Meaden 1985a), and summer (Kirk 2014). Using both tornado day and tornado number analysis, this article will address the discrepancy in seasonality.

An analysis of the types of storms and environmental parameters conducive to producing tornadoes has not been conducted by the studies in Table 1. The only research on environmental conditions associated with tornadic storms have been case studies (e.g., Bolton et al. 2003; Clark 2012) or were based on reanalysis data over short periods and large areas (e.g., Brooks et al. 2003b; Romero et al. 2007). This article addresses these gaps in the research by including storm type and proximity sounding analyses. Additionally, this article assesses the probability of tornadoes spatially in the British Isles, furthering the gridded tornado frequencies presented in Meaden (1985a).

Section 2 discusses the Tornado and Storm Research Organization (TORRO), the organization from which the tornado occurrence data come. Section 3 describes the data and methods used in this study. The type of parent storms producing tornadoes is analyzed in section 4. Spatial patterns in tornado occurrence are presented in section 5, including an analysis of probability of tornado occurrence and how those probabilities change throughout the year. Section 6 examines the interannual variability, annual cycle, diurnal cycle, and occurrence of outbreaks. Section 7 details the intensity of tornadoes. Section 8 describes the environmental conditions in which tornadoes occur using proximity soundings. The results are summarized in section 9.

2. TORRO

The data used in this climatology come from TORRO, a U.K.-based, nonprofit organization founded in 1974 (Elsom and Meaden 1984; Meaden 1985b; Elsom et al. 2001). TORRO collects severe weather reports from the media and over 350 observers in the United Kingdom, Republic of Ireland, and elsewhere around the world

(Elsom et al. 2001). The public can also submit reports through the TORRO website (http://www.torro.org.uk). Although TORRO collects reports worldwide, its contributors are concentrated in the British Isles, which is the subset of data used in this article. TORRO staff, ranging from amateur meteorologists to doctoral researchers, work on a volunteer basis. To help distribute work within the organization, TORRO is broken into three divisions: Tornado, Thunderstorm and Severe Weather, and Severe Weather Forecast.

Besides collecting severe weather reports, TORRO conducts site investigations to verify tornado reports and classify the damage using the tornado intensity scale (T scale). In 1972, Terence Meaden, the founder of TORRO, created the T scale, a tornado intensity classification scale, similar to the Fujita scale used in the United States (Elsom et al. 2001; Kirk 2014). The T scale has twice as many classifications as the Fujita scale, making it useful for European tornadoes, which tend to be less intense than American tornadoes (Meaden 1985b). To convert between the Fujita (F) and T scales, the equation $F \approx 0.5T$ and rounded down to the nearest integer can be used (Brooks and Doswell 2001; Meaden et al. 2007).

TORRO designates tornado reports as either probable, meaning a tornado likely occurred but no hard evidence has been cited, or definite, meaning a tornado has been confirmed. The distinction between probable and definite is determined on a case-by-case basis with the final word lying with the head of the Tornado Division of TORRO. The amount of information available on the report determines the designation of probable or definite. For example, a tornado would be classified as definite if a site survey was completed and damage was concluded to be attributable to a tornado. If there was no site survey, but a photo or video of the tornado was available, the report would also be considered definite. Reports coming from a knowledgeable, educated observer would likely become definite after more investigation. If only photos of damage were available, classification depends on the damage portrayed. For example, twisted trees or a narrow swath of damage would help designate a tornado as definite. In the absence of a site investigation or photographic or video evidence, an environmental situation conducive to tornadoes would designate the report as probable. This article uses both definite and probable reports, similar to Elsom and Meaden (1984) and Kirk (2014).

3. Data and methods

This climatology uses tornado reports collected by TORRO during 1980–2012 over England, Scotland, Wales, Northern Ireland (together considered the United Kingdom), the Republic of Ireland, the Channel Islands, and the Isle of Man (Fig. 1). For the purpose of this article, this area is considered the British Isles. As our period of analysis falls after the founding of TORRO, the data used herein are not based on historical reports, but instead from observer and media reports.

Waterspouts are excluded from this article because they are not as reliably reported as land-based tornadoes. Additionally, we want to document land-based tornadoes because these are more threatening to life and property. Cases that originated on land and moved over water or originated on water and moved over land were included in the analysis because they were over land for part of their duration. Some reports include multiple tornadoes in the same location, occurring as part of the same parent storm or boundary. These reports are considered one tornado case (Rauhala et al. 2012). To control for outbreaks (a day in which three or more tornadoes occur), tornado-day analysis was also conducted.

Some cases in the TORRO database are incomplete, containing uncertain location, time of occurrence, or intensity. Any uncertain information was left out of the analysis, although the case remained in the dataset to prevent the tornado dataset from becoming too limited. Therefore, there are different numbers of tornadoes included in different analyses. These numbers are reported along with the results.

An unusually large outbreak, which was omitted from some analyses, occurred on 23 November 1981 when 104 tornadoes were reported across the British Isles (hereafter called the 1981 Outbreak). The size of the outbreak was unusual for the British Isles (discussed in section 6d). One reason so many tornadoes were reported were the appeals made for further reports. According to Rowe (1985), reports of 35 tornadoes came from press cuttings, 30 came after meteorologist Michael Hunt called for reports on Anglia Television, and the remaining 39 came from TORRO's appeals in provincial newspapers. As a result of the appeals, it is possible that some tornado reports are not valid or are reporting the same tornado. It is also possible that there were indeed 104 tornadoes on that day, but a similar appeal process has not been followed for subsequent tornado cases. Therefore, in most analyses in the present paper, results are presented both including and excluding the 1981 Outbreak, in case this event was overreported.

There were 1241 tornado cases over 642 tornado days (including the 1981 Outbreak) over the 33 years. The data used herein differ slightly from Kirk (2014), who analyzed 1416 tornado cases on 729 tornado days. First, we included data from 1980, 2011, and 2012, and

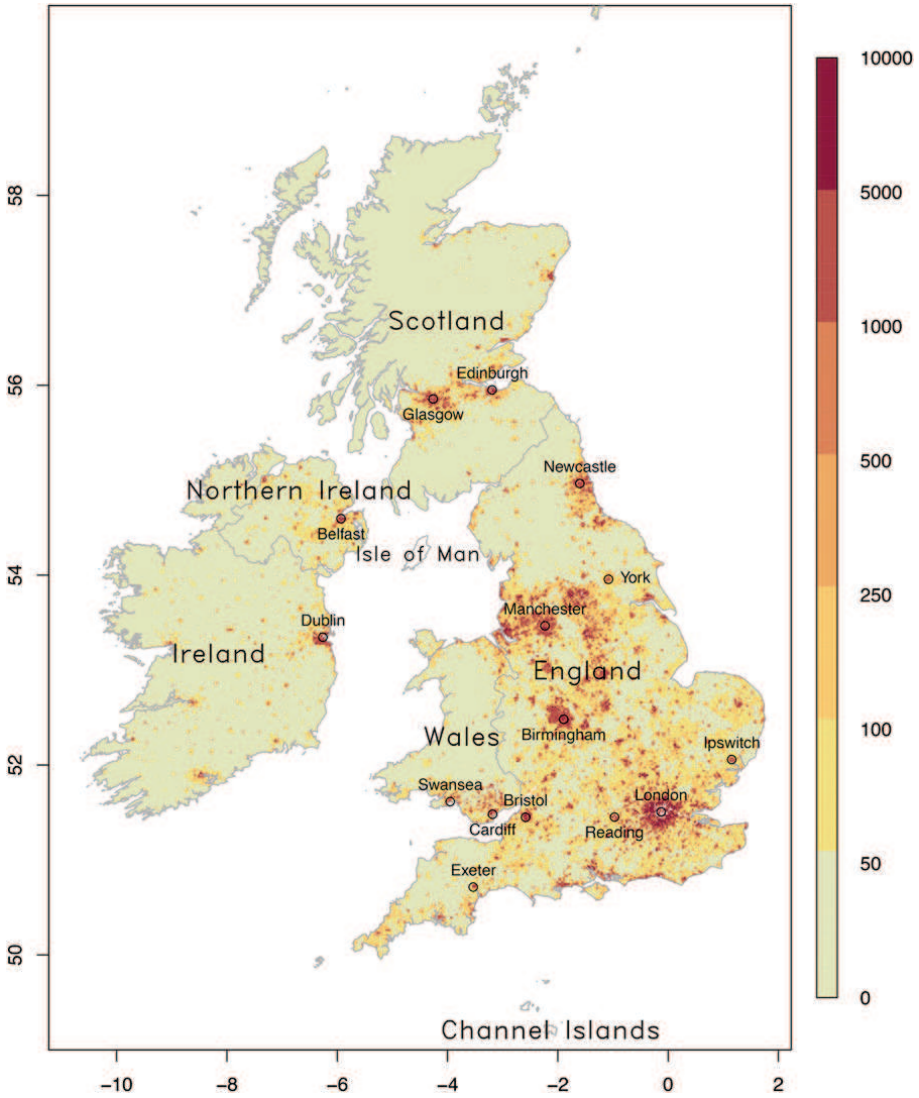

FIG. 1. Map of the British Isles and locations described in the text and 2000 population density in people per square kilometer.

included the Republic of Ireland. Second, we excluded tornadoes occurring only over water. Third, we excluded the 1981 Outbreak from some analyses. Fourth, we omitted uncertain data from analysis.

4. Parent storm analysis

To determine the type of storm from which tornadoes were produced, the Met Office 1-km grid spacing Nimrod radar 5-min composite rainfall rates were used. Radar data were only available starting in April 2004, so a subset of 254 tornadoes with known locations, dates, and times during April 2004–December 2012 (20% of all 1241 tornado cases) were included in this analysis.

Parent storms were categorized manually based on the classification scheme in Gallus et al. (2008) (Fig. 2). All morphologies had at least 2.5 mm h^{-1} peak rainfall rate. Because of the small sample of tornadoes, broken lines, bow echoes, and all squall lines with or without stratiform rain were collectively classified as linear (Fig. 2). Linear morphologies were defined by being at least 3 times as long as wide and at least 75 km long, following Gallus et al. (2008). Other morphologies were isolated cell, nonlinear, cluster, and unassigned. Isolated cells were defined as cells with high rainfall rates completely separated from each other. Clusters, like isolated cells, had discrete regions of high rainfall rates but were connected by weak rainfall rates. Nonlinear morphologies differed from clusters due to their lack of discrete cells and large size (approximately 70 km wide). If the case did not fit into a category, belonged to multiple categories, or could not be classified because of poor

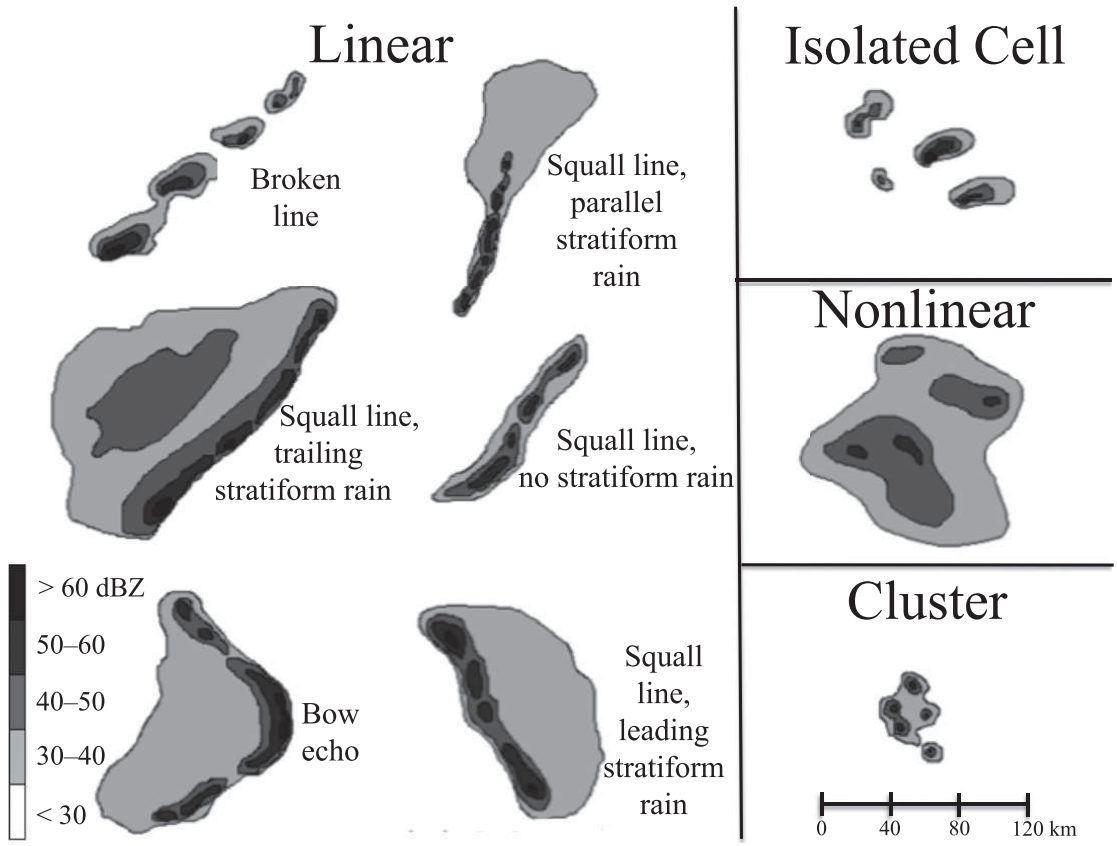

FIG. 2. Classification scheme for parent storm analysis, adapted from Gallus et al. (2008).

radar coverage, it was classified as unassigned (Doswell 1991).

The most common category of storm morphology, with 42% of all tornadoes in the British Isles, was the linear category (Fig. 3). In contrast, in the United States during 1998–2000, 18% of tornadoes were produced from linear systems, with 79% produced from isolated cells (Trapp et al. 2005). Other morphologies in the British Isles were isolated cells (28%), nonlinear systems (11%), and clusters of cells (9%). The remaining 10% were unassigned. In winter and autumn, the most common storm morphology was linear storms (52% and 62%, respectively; Fig. 4). In summer, 42% of tornadoes were produced by isolated storms, the most common storm morphology. In spring, the most common storm morphology was isolated cells (31%) followed by nonlinear storms (23%); linear storms were least common in spring compared to the other seasons (14%; Fig. 4).

5. Spatial distribution of tornadoes

To analyze the spatial distribution of tornadoes, gridded point observations of tornado touchdown locations ($n = 1091$) were smoothed temporally and spatially using Gaussian smoothers. The method is the same as Brooks et al. (2003a) and is summarized below. Touchdown locations were used because only 20% of cases had track information. Additionally, because 83% of track lengths were less than or equal to 5 km, incorporating track length would produce similar results. Tornadoes from the 1981 Outbreak were omitted from the spatial analysis because they distorted the spatial distribution of tornadoes on and near that day.

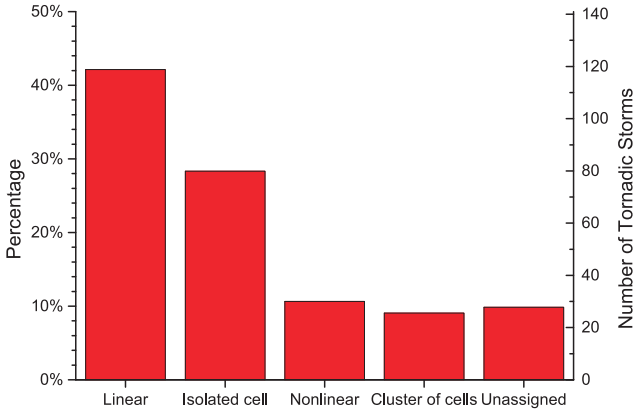

FIG. 3. Histogram of parent storm type for tornadic storms in the British Isles, based on the classification scheme in Fig. 2. Left side y axis in percentage of total 254 tornadic storms; right-side y axis in number of tornadic storms.

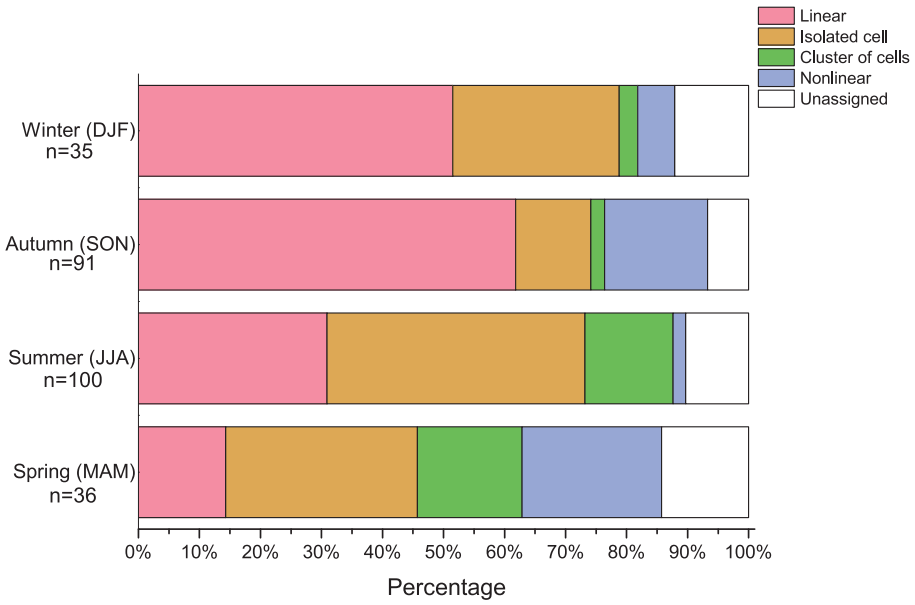

FIG. 4. Percentage of tornadic storms classified as each parent storm type in the British Isles by season based on the classification scheme in Fig. 2.

First, tornado point observations were transferred to a grid box with Lambert conformal conic map projection (standard parallels of 43° and 62°N). Grid spacing was 0.125°, or approximately 10-km by 10-km grid size. Second, the mean unsmoothed frequency of tornado occurrence on the day of interest m, was calculated for each grid box every day of the year by

$$m = \frac{M}{N}, \tag{1}$$

where M is the number of years in the period with at least one tornado in the grid box and N is the number of years in the dataset ($N = 9$ for 29 February, $N = 33$ for all other days). Third, the data were temporally smoothed using

$$f_n = \sum_{k=1}^{366} \frac{m}{\sqrt{2\pi}\sigma_t} \exp\left[-\frac{1}{2}\left(\frac{n-k}{\sigma_t}\right)^2\right], \tag{2}$$

where f_n is the mean time-smoothed frequency of tornadoes on the day of interest n, k is the day of the year, and σ_t is the temporal smoothing parameter. Fourth, f_n is smoothed spatially to find $p_{x,y,n}$, the probability of a tornado occurring within the grid box (x, y) on day n by

$$p_{x,y,n} = \sum_{j=1}^{J} \sum_{k=1}^{I} \frac{f_n}{2\pi\sigma_x^2} \exp\left[-\frac{1}{2}\left(\frac{d_{i,j}}{\sigma_x}\right)^2\right], \tag{3}$$

where I is the number of grid boxes in the x direction, J is the number of grid boxes in the y direction, $d_{i,j}$ is the Euclidean distance between the location of interest (x, y) and the data location (i, j), and σ_x is the spatial smoothing parameter. A 15-day temporal smoothing parameter was used, the same as used in Brooks et al. (2003a). Brooks et al. (2003a) used a 120-km spatial smoothing parameter for their 80-km by 80-km grid size. Because of our smaller grid size, a 50-km spatial smoothing parameter was chosen. The results were plotted as smoothed contours to help detect important spatial patterns.

Maximum annual cumulative probability of a tornado in a 10-km grid box was maximum in England (Fig. 5), where 78% of cases occurred. Local probability maxima were typically near cities. More specifically, probabilities of tornadoes within 10 km of a point were locally higher southwest of London between London and Reading (up to 6.0%), northeast of London to Ipswich (up to 4.0%), from Bristol north to Manchester (up to 5.0%), and along the south coast of Wales near Swansea (up to 3.0%). Scotland, Northern Ireland, the Republic of Ireland, and the Channel Islands had local maxima up to 2.0% chance of a tornado occurring within 10 km of a point.

The area of highest tornado probability varied by location throughout the year (Fig. 6). February through April, tornado probabilities were small (up to 0.02%) and localized across England. In May through September, the probability of tornadoes filled in across England and locally increased to up to 0.03%. In October through December, the maximum tornado probability moved to southern England before low probabilities become scattered across England again in January.

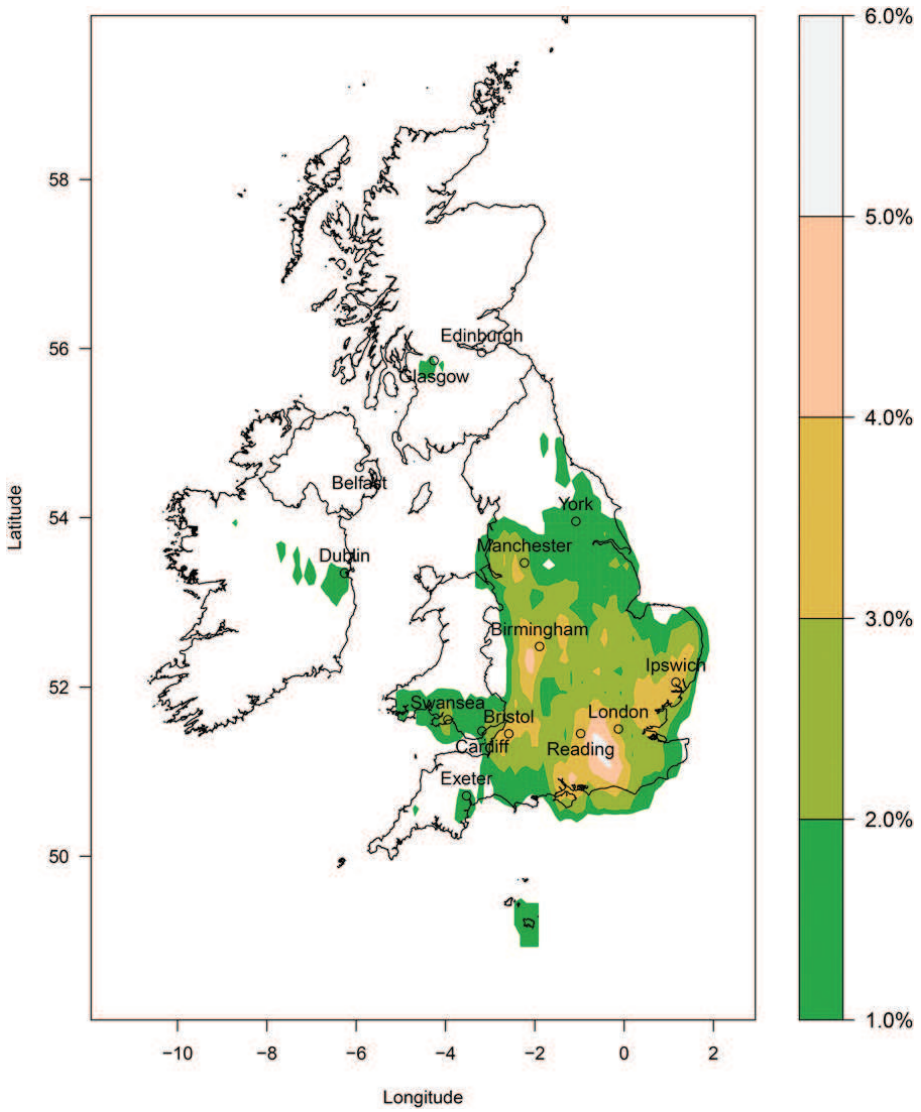

FIG. 5. Cumulative percent probability of a tornado occurring in a 10-km grid box across the British Isles per year, using a 15-day temporal and 50-km spatial smoothing parameter.

The migration of maximum tornado probability, up to 0.04%, in the British Isles south toward coastal areas and relatively warm seawater is similar to the migration of maximum tornado probability from the Great Plains to the southeastern United States (referred to as ''Dixie Alley'') during November through February (Brooks et al. 2003a; Gagan et al. 2010; Dixon et al. 2011; Smith et al. 2012). Perhaps the spatial change in tornado probabilities in the British Isles is due to local, seasonal conditions favorable to deep, moist convection. For example, Holley et al. (2014) found that highest convective available potential energy (CAPE) values in September through January (over the study period 2002–12) were along the south coast of England.

The overall spatial patterns of tornado probabilities could be affected by secular differences. This is especially apparent in Fig. 5, where higher probabilities mirrored the population density in the United Kingdom (Fig. 1) and in Fig. 6 where areas of higher probability lingered near cities throughout the year. Tornado probabilities were near zero in central and eastern Wales, most of Scotland, the Republic of Ireland, and Northern Ireland throughout the year (Fig. 6). These patterns were likely present because of the few people present to witness and therefore report a tornado. An additional challenge in the British Isles is that tornado occurrence data are not actively collected through the Met Office or Irish Meteorological Service. Although tornado occurrence data are collected for tornado warning verification in the United States, tornado warnings are not issued in the United Kingdom (Rauhala and Schultz 2009) or the Republic of Ireland (http://www.met.

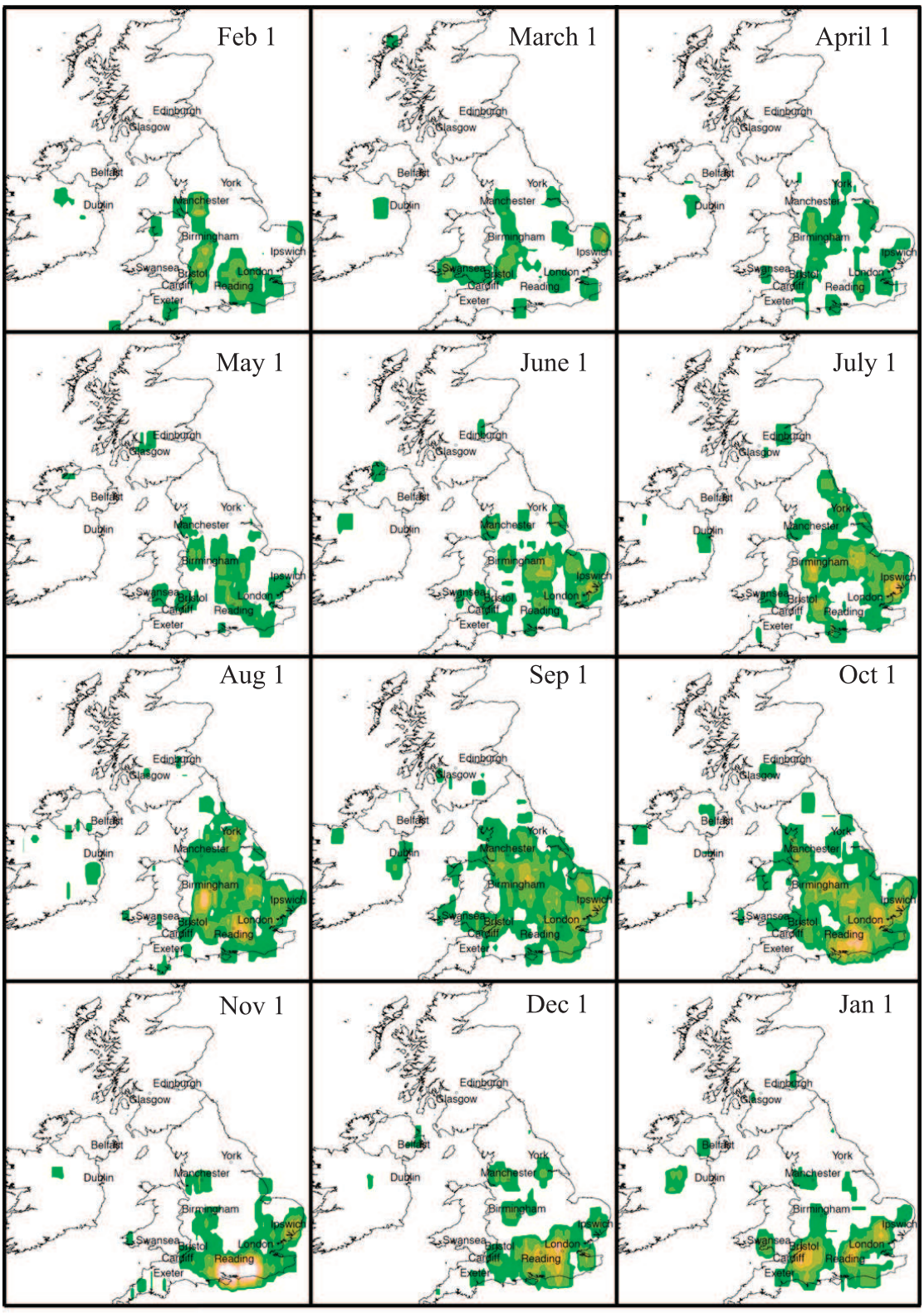

FIG. 6. Change in tornado percent probabilities on the first day of every month using a 15-day temporal and 50-km spatial smoothing parameter.

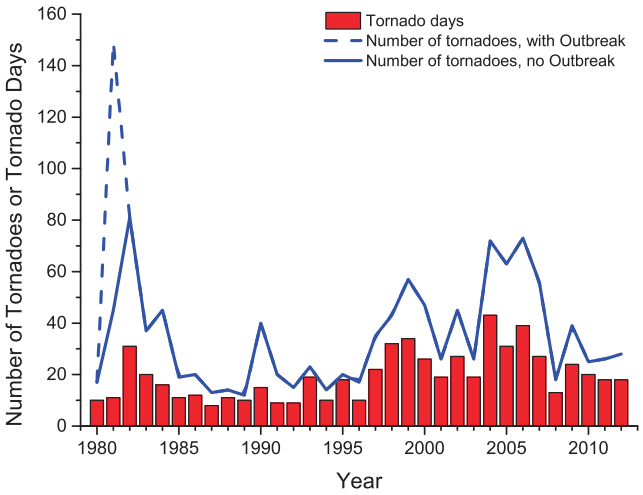

FIG. 7. Histogram of number of tornadoes and tornado days per year during 1980–2012. Number of tornadoes including the 1981 Outbreak are shown as a dashed line ($n = 1235$). Number of tornadoes not including the 1981 Outbreak are shown as a solid line ($n = 1131$). Tornado days are shown as columns ($n = 642$).

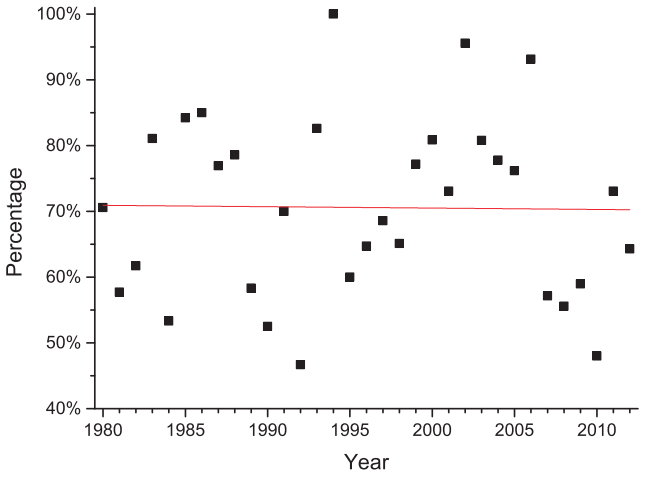

FIG. 8. Scatterplot of the percentage of all tornado cases that are definite (as opposed to probable) by year, 1980–2012. The best-fit line is also shown.

ie/nationalwarnings/warnings-explained.asp). Instead, wind and rain (and thunderstorm, in the Republic of Ireland) warnings are issued because these hazards pose a greater risk, partially because of their more common occurrence and larger area affected. Additionally, hazards from wind and rain occur simultaneously with tornado threats.

6. Temporal analysis

The following sections discuss when tornadoes and outbreaks occur in the British Isles.

a. Annual variation

The number of tornadoes by year, including the 1981 Outbreak, ranged from 12 in 1989 to 149 in 1981 with a mean of 37.4 and a median of 26 tornadoes per year. Not including the 1981 Outbreak, the maximum annual tornado occurrence was 81 in 1982 with a mean of 34.3 and a median of 26 tornadoes per year. A mean of 19.5 and median of 18 tornado days occurred annually with a minimum of 8 in 1987 and a maximum of 43 in 2004. The mean tornado numbers and days per year were lower than that of Kirk (2007) because waterspouts were not included in this article. The mean tornado numbers and days differed from that of Kirk (2014) because this article included different years (Table 1) and handled the data differently.

There was evidence of a stepwise increase in tornado cases between 1980–96 and 1997–2012 (Fig. 7). The mean number of tornadoes per year, not including the 1981 Outbreak, increased from a mean of 26.6 and a median of 20.0 in 1980–96 to a mean of 42.4 and a median of 41.0 in 1997–2012. The means did not differ significantly when including the outbreak ($p = 0.31$), but significantly differed when the outbreak was omitted ($p < 0.01$). Mean annual tornado days differed significantly ($p = 0.02$) between 1980 and 1996 with a mean of 13.5 and a median of 11.0 and 1997–2012 with a mean of 25.8 and a median of 25. The increase in tornado cases could be explained by increased awareness and interest in tornadoes due to the popular film *Twister* released in July 1996 in the United Kingdom.

There did not appear to be a difference in the percentage of definite (versus probable) tornadoes during 1980–2012 (Fig. 8), indicating that social media and the prevalence of phones with cameras, which have gained popularity in the past five years, have not necessarily led to an observed increase in reporting or verification of tornadoes. In fact, there was a significant decrease in the mean percentage of definite tornadoes in the last five years studied ($p = 0.02$).

All previous U.K. tornado climatologies including 20 years or more of data, not including waterspouts, cite a mean of between 27 and 37 tornadoes per year (Table 1). These means are comparable to the means found herein, providing evidence that the dataset has stabilized since the 1997 step function increase.

England averaged 2.2 tornadoes per year per 10 000 km^2, more than the 1.3 per year per 10 000 km^2 in the United States (including Alaska and Hawaii, 1991–2010; NCDC 2014). Because the frequency of occurrence of tornadoes in the United States is higher east of the Rocky Mountains, the country as a whole averaged fewer tornadoes per area compared to England. For comparison, Oklahoma, in "Tornado Alley," had an average of 3.5 tornadoes per year per 10 000 km^2. Including the rest of the British Isles, there were 1.2

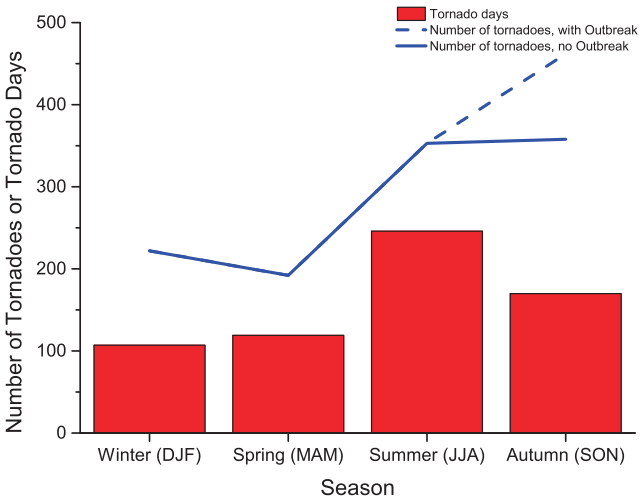

FIG. 9. Histogram of the number of tornadoes and tornado days by season. Number of tornadoes is shown both including the 1981 Outbreak (dashed line, $n = 1229$) and not including the 1981 Outbreak (solid line, $n = 1125$). Tornado days are shown as columns ($n = 642$).

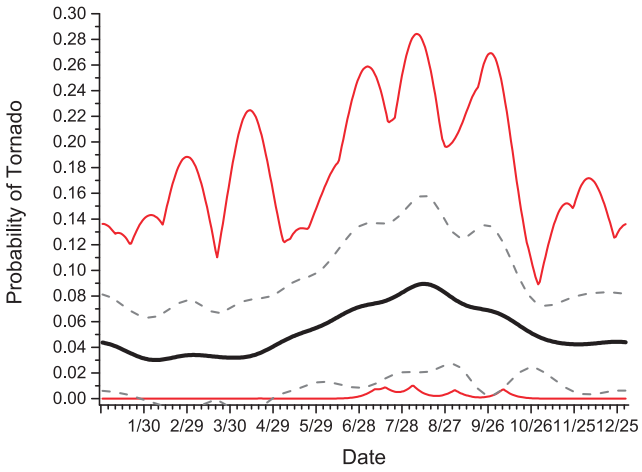

FIG. 10. Probability of a tornado day occurring anywhere in the British Isles by temporally smoothing tornado occurrence data using a 15-day moving window. Probabilities are expressed as a decimal between 0 and 1. The bold black line is the mean, dashed lines are the mean plus and minus one standard deviation, and the red solid lines are maximum and minimum values.

tornadoes per year per 10 000 km^2, comparable to the value for the entire United States.

b. *Monthly distribution*

Tornado season in the British Isles depends upon the inclusion of the 1981 Outbreak and the use of tornado numbers or tornado days. With the outbreak, the season with the highest number of tornadoes (37.6%) was autumn (Fig. 9), consistent with Reynolds (1999), Kirk (2007), and Kirk (2014) (Table 1). Removing the outbreak, there were nearly equal tornado numbers in the summer and autumn (31.4% and 31.8%, respectively), consistent with Tyrrell (2003) (Table 1). Conversely, the season with the highest proportion of tornado days (38.3%) was summer (Fig. 9), consistent with Kirk (2014) (Table 1).

Smoothing all tornado occurrence data with known dates ($n = 1183$) temporally following Eq. (2) yielded the probability of a tornado day occurring anywhere in the British Isles any day of the year, represented as a decimal between 0 and 1 (Fig. 10). The probability of a tornado day doubled from 0.04 in January to 0.08 in August, which makes May through October appear to constitute a "tornado season." For comparison, the decimal probability of tornadoes in the United States increased from almost 0.2 to approximately 0.9 from 1 January to mid-June (Fig. 11). The nearly fivefold increase in tornado probabilities indicates a more distinct tornado season in the United States compared to the twofold increase in the British Isles. Additionally, the probability of tornado days in the British Isles from September to December was nearly constant (Fig. 10). Although there is a slight seasonality to tornado days, tornadoes occur year-round in the British Isles.

c. *Diurnal distribution*

Of the 669 tornadoes in the British Isles for which the time of occurrence was known, including the 1981 Outbreak, 77.6% occurred during the daytime between 0800 and 2000 UTC (Fig. 12). There was a maximum in tornado occurrence in the late morning and afternoon with 57.5% of tornadoes touching down between 1100

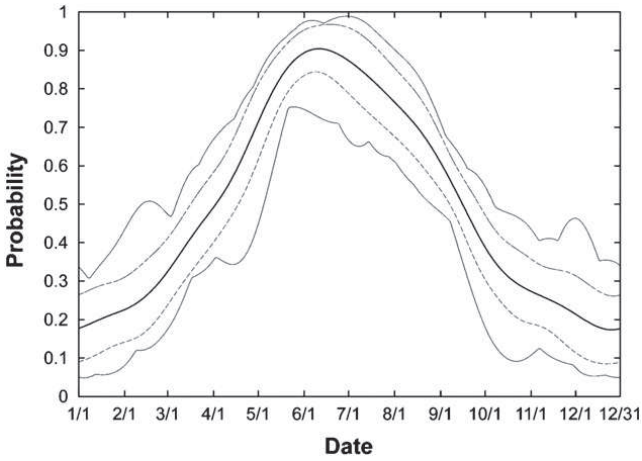

FIG. 11. Probability of a tornado day anywhere in the United States, smoothing tornado touchdown data during 1980–99 using a 15-day moving window. Probabilities are expressed as a decimal between 0 and 1. Similar to Fig. 10, the bold black line is the mean, dashed lines are the mean plus and minus one standard deviation, and the thin solid lines are maximum and minimum values [from Brooks et al. (2003a)].

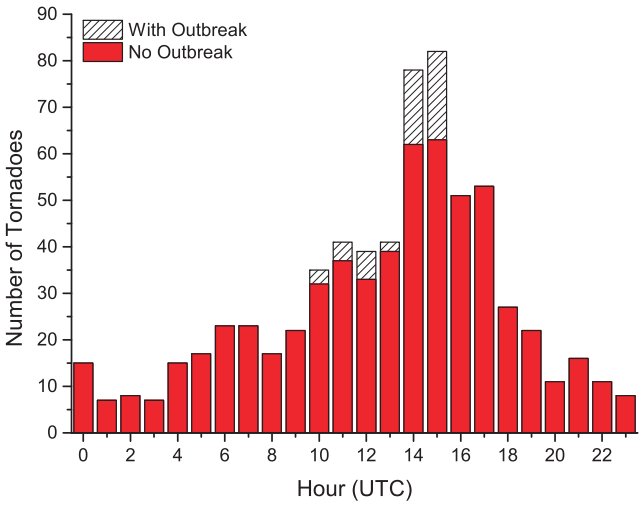

FIG. 12. Histogram of diurnal distribution of tornado cases including the 1981 Outbreak (hashed columns, $n = 669$) and not including the 1981 Outbreak (solid columns, $n = 619$).

and 1759 UTC, the same percentage as Kirk (2014). Excluding the 1981 Outbreak, 54.6% of tornadoes occurred between 1100 and 1759 UTC, resembling the distribution including the outbreak.

By season, an afternoon peak in tornado activity occurred in spring, summer, and autumn (Figs. 13a, 13b, and 13c, respectively). In the winter, tornadoes occurred consistently through the day and night, except for a dip before midnight and at 0100 UTC (Fig. 13d). The British Isles are between 49° and 60° latitude so there are less than 8 h of daylight in the winter. Because tornadoes were reported throughout the night, especially in winter, there likely was not a reporting bias toward daytime tornadoes.

d. Tornado outbreaks

There was a mean of 2.5 and a median of 2 tornado outbreaks (3 or more tornadoes in a day) per year with 12.8% of tornado days being outbreak days (Fig. 14). Omitting the 1981 Outbreak, all tornado outbreaks consisted of fewer than 30 tornadoes and 90.2% of outbreaks had fewer than 10 tornadoes. The probability of exceedance of a 29-tornado outbreak was 0.3%, meaning a 104-tornado outbreak would be unlikely and rare, although still possible.

Tornado outbreaks, 51% of which were produced by linear storms, occurred year-round with a maximum of

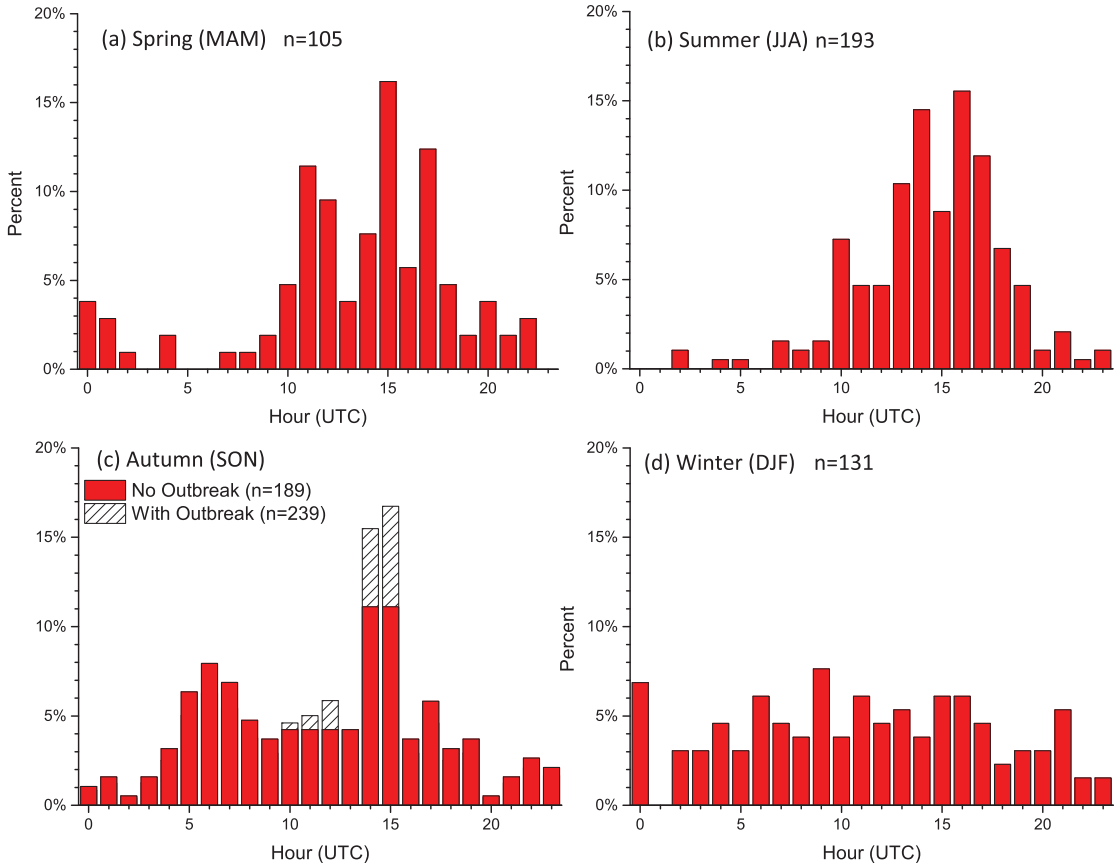

FIG. 13. Histogram of diurnal distribution of tornado cases in (a) spring, (b) summer, (c) autumn, and (d) winter. In autumn, the distribution is shown both including the 1981 Outbreak (hashed columns) and without the 1981 Outbreak (solid columns).

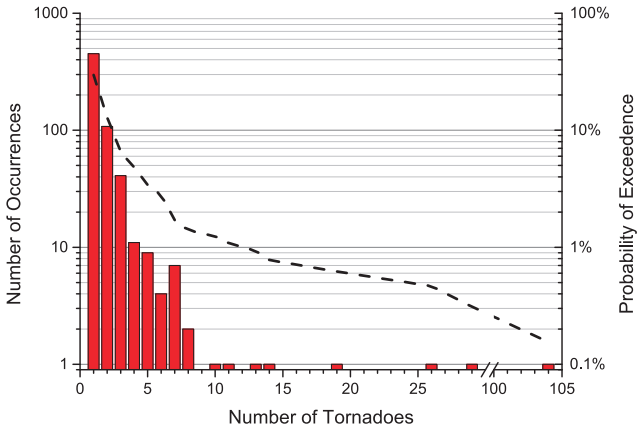

FIG. 14. Number of tornadoes occurring on each of the 642 tornado days, defined as 0000–2359 UTC during 1980–2012. Number of occurrences is on the left-side y axis. The probability of exceedance, presented as percent probability, is shown as the dashed black line corresponding to the right-side y axis.

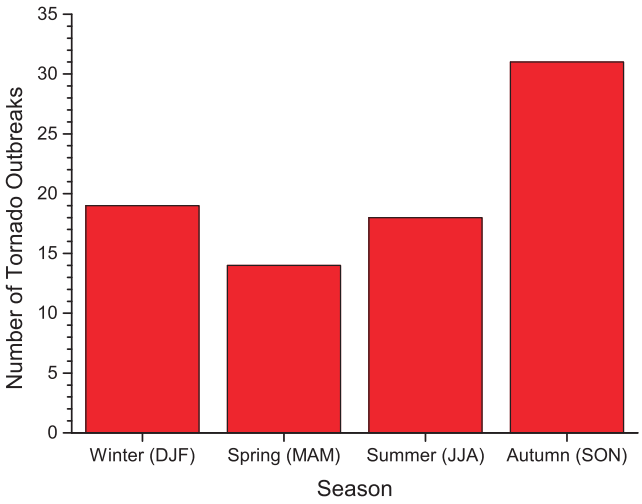

FIG. 15. Histogram of number of tornado outbreaks, defined as three or more tornadoes in one day, by season in which they occurred. There are a total of $n = 82$ outbreaks, including the 1981 Outbreak.

13 outbreaks in November and a minimum of 3 in May. Seasonally, outbreaks most commonly occurred in autumn than the rest of the year, when the number of outbreaks was nearly constant (Fig. 15).

7. Intensity

Tornadoes ranged from T0 to T5 (F0–F2) in intensity, a maximum intensity less than the United States (Fig. 16). Of the 608 tornadoes with known intensities, 95% ($n = 577$) were between T0 and T3 intensity (F0–F1), comparable to the 90% of tornadoes between T1 and T3 intensity that Kirk (2014) found. Only 5% of tornadoes ($n = 29$) during the study period were significant [T4–T5 or F2 intensity, after Hales (1988)].

Figure 16 is a log–linear graph showing the number of tornadoes of each T-scale rating by decade. Each decade was normalized to 100 T2 tornadoes to more easily compare the slopes of tornado intensity. The slope was nearly log–linear in the United States (Fig. 16), which Brooks and Doswell (2001) hypothesized to signify a nearly complete tornado dataset. In the British Isles, there were too few weak tornado cases for the slope to be log–linear. The T0 and T1 (F0) tornado cases increased from 31% in the 1980s to 43% in the 1990s to 56% in the 2000s. The increase of weak tornado cases signified less underreporting of weak tornadoes; however, the British Isles tornado dataset still appears less complete than that of the United States, assuming that log–linear implies completeness of the dataset.

Brooks and Doswell (2001) also discussed the differences in slopes of log–linear intensity graphs for different regions in the United States and different countries worldwide (their Figs. 3 and 4, respectively). They speculated that differences in slopes relate to the type of storms from which tornadoes are produced: steep slopes representing regions dominated by nonsupercell tornadoes and less steep slopes representing regions dominated by supercell tornadoes. The slope of the British Isles log–linear intensity graph in each decade was steeper than that of the United States (Fig. 16), suggesting that the British Isles was dominated by nonsupercell tornadoes.

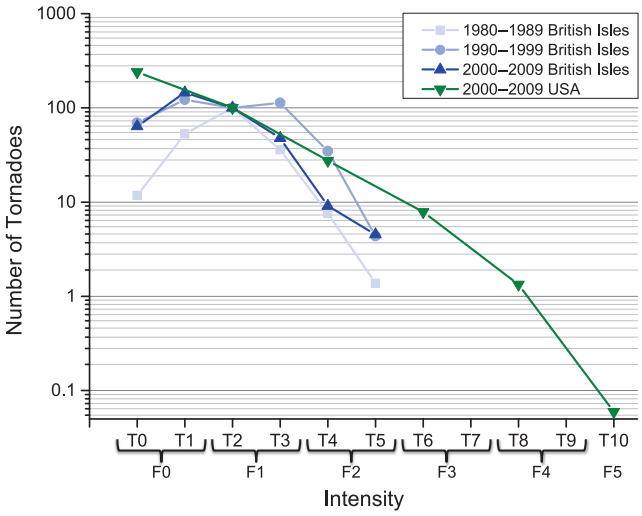

FIG. 16. Tornado cases by the tornado intensity (T) scale for the British Isles and the United States by decade. Conversion to the Fujita (F) scale is also shown. U.S. F-scale ratings were converted to the T scale by $T \approx 2F$. Tornadoes with intensity information were used for the British Isles ($n = 569$, including the 1981 Outbreak) and United States ($n = 14\,116$). Tornado numbers were scaled to 100 T2 tornadoes to easily compare slopes.

One reason the British Isles had weaker tornadoes than the United States is because British Isles tornadoes most commonly came from linear storms, which tend to be weaker than tornadoes from isolated cells, especially supercells (Trapp et al. 2005; Grams et al. 2012). Indeed, of the 228 cases included in the parent storm analysis where intensity information was known, 5% of tornadoes from isolated cells were significant, whereas only 2% of tornadoes from linear storms were significant. However, we cannot verify whether the parent storms in section 4 were supercells because Doppler velocity data were unavailable. Another reason for weaker tornadoes in the British Isles is the weaker instability compared to environmental soundings of tornadoes in the United States, discussed further in section 8.

8. Environmental parameters derived from proximity soundings

To determine environments conducive to tornadoes in the British Isles, sounding-derived parameters were calculated for tornadic and nontornadic (null) convective storms using upper-air observations provided by the University of Wyoming. We adopted the same proximity criteria as in Brooks (2009): soundings within 3 h and 180 km of the case. Because the date, time, and location of the tornado were required, tornado cases without those data were omitted, leaving 659 tornadoes, 53% of all tornado cases, for the proximity analysis. After applying the proximity criteria and removing duplicate soundings, 438 tornado-case soundings remained.

All hourly surface SYNOPs in the British Isles during 1980–2012 reporting current thunderstorm or hail, which ensured the timing and location of the event was known, were chosen as potential null cases ($n = 938$). After applying the same proximity criteria as tornado cases to station locations and removing duplicate soundings, 773 null case soundings remained.

Because we wanted to study the air mass producing the null or tornadic convective thunderstorm, soundings showing an airmass change (e.g., postfrontal soundings in the case of storms occurring in the prefrontal environment) were omitted. To help identify postfrontal soundings, Met Office surface analyses were cross checked for front locations, when available. Additionally, if observations that affected calculations of parameters (discussed shortly) were missing, the sounding was also omitted. After removing soundings not representing the null or tornadic environment or incomplete soundings, 393 null and 188 tornadic soundings remained. Of the tornadic soundings, 46 represented outbreak days and 7 represented significant tornado environments.

Parameters calculated in the radiosonde analysis were low-level (0–1 km) and deep-layer (0–6 km) bulk shear (i.e., the vector difference in wind between levels), convective available potential energy (CAPE) with virtual temperature correction (Doswell and Rasmussen 1994), convective inhibition with virtual temperature correction (CIN), height of the lifting condensation level (LCL), and height of the level of free convection (LFC). CAPE, CIN, LCL height, and LFC height were calculated from a mean temperature and dewpoint temperature from the bottom 500 m of the sounding (http://weather.uwyo.edu/upperair/indices.html). Parameters were analyzed separately for null, tornado, outbreak, and significant tornado soundings to compare environments.

There was no significant difference in low-level shear between null, tornado, outbreak, and significant tornado cases ($p > 0.05$, Fig. 17a). Similarly, Clark (2013) found that differences in 0–1-km and 0–3-km shear between tornadic and nontornadic cold season convective lines in the United Kingdom were not significant. Although Craven and Brooks (2004) suggested 10 m s^{-1} of low-level shear as a threshold for significant tornadoes in the United States, only 3 of the 7 (43%) significant tornadoes in the British Isles occurred in environments exceeding that threshold. An alternative threshold cannot be given because the differences between these groups were not statistically significant ($p > 0.05$).

Mean deep-layer bulk shear was 20.5 m s^{-1} for tornado cases and 23.3 m s^{-1} for null cases (Fig. 17b). The mean deep-layer shear in tornado cases was significantly less than that for null cases ($p = 0.01$). Although significant tornadoes appeared to have higher deep-layer shear than null, tornado, and outbreak cases, these relationships were not statistically significant ($p > 0.05$) due to the small sample size of significant tornadoes. All but one deep-layer shear value for significant tornadoes was higher than 20 m s^{-1}, the threshold Craven and Brooks (2004) cited for significant tornadoes. Although 42% of all tornado soundings had a deep-layer shear greater than 20 m s^{-1}, 7.8% of all tornado soundings with greater than 20 m s^{-1} deep-layer shear were associated with significant tornadoes. In contrast, 0.9% of all tornado events with less than 20 m s^{-1} deep-layer shear were associated with significant tornadoes, suggesting that significant tornadoes rarely occur in the British Isles with less than 20 m s^{-1} deep-layer shear.

Mean CAPE in tornado and outbreak cases was significantly higher than in null cases ($p < 0.01$, $p = 0.02$, respectively, Fig. 17c). However, zero CAPE did not preclude tornado cases. Significant tornadoes all had nonzero CAPE with a mean of 81.6 J kg^{-1} and a median of 39.7 J kg^{-1}, larger than a mean of 99.7 J kg^{-1} and a median of 18 J kg^{-1} for all tornado cases. However,

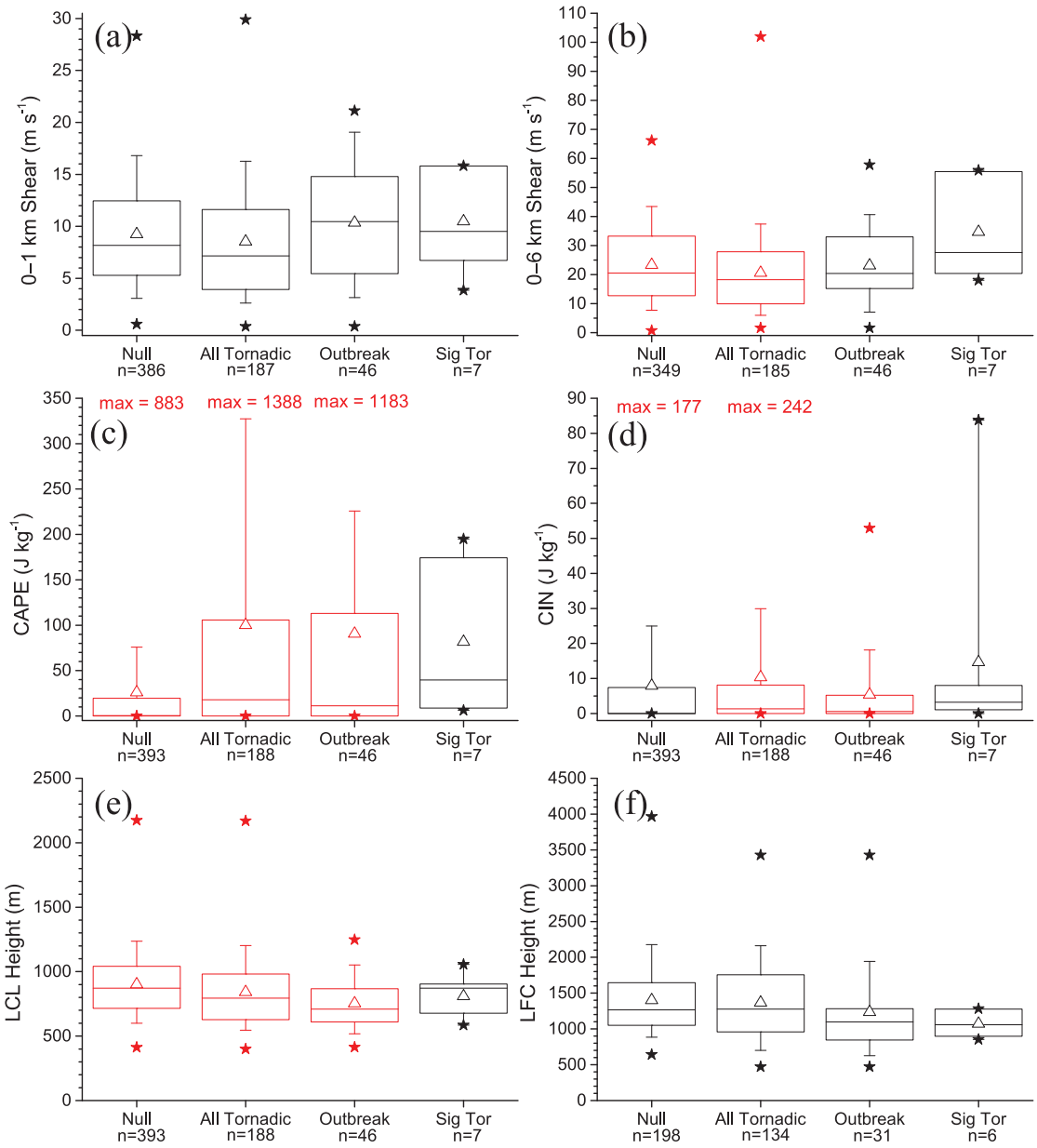

FIG. 17. Selected parameters from proximity radiosondes representing convective storms without a tornado (null), tornadic storms (all tornadic), tornadic storms that occurred on an outbreak day (outbreak), and tornadic storms that produced a T4+ or F2 tornado (sig tor). The top and bottom of the boxes represent the 75th and 25th percentile, respectively. The bar in the middle of the box is the 50th percentile. The triangle is the mean. The whiskers above and below the box represent the 90th and 10th percentile, respectively. Stars represent the maximum and minimum values in the dataset. Red coloring represents statistically significant differences in means ($p < 0.05$). Black coloring represents differences in means that are not significant ($p > 0.05$). More details on results of statistical tests appear in the text. The parameters shown are (a) low-level (0–1 km) bulk shear, (b) deep-layer (0–6 km) bulk shear, (c) mixed-layer CAPE with the virtual temperature correction, (d) CIN with the virtual temperature correction, (e) LCL height, and (f) LFC height.

because of the small sample size, CAPE in significant tornado cases did not differ statistically significantly from that for all tornado cases ($p > 0.05$). In the continental United States, significant tornado mean-layer CAPE values were higher than in the British Isles and can exceed 4000 J kg^{-1} with a median just over 1000 J kg^{-1} (Grams et al. 2012, cases from 2000 to 2008) compared to a median of 39.7 J kg^{-1} for significant tornadoes in the British Isles.

Null, tornado, and outbreak cases did not appear to have separate parameter space when combining CAPE and deep-layer shear (Fig. 18). Although high

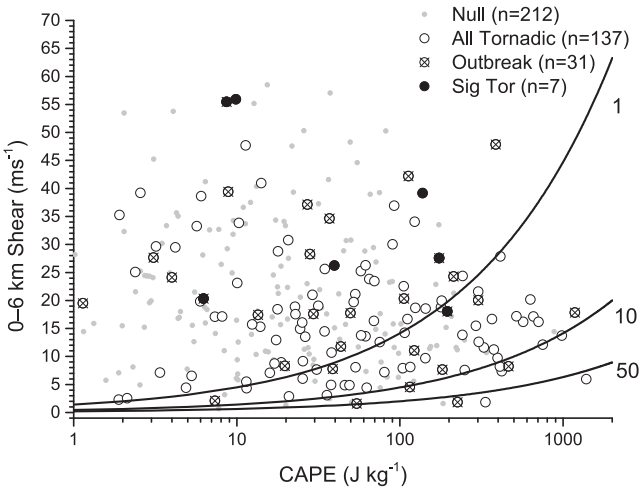

FIG. 18. Mixed-layer CAPE with the virtual temperature correction plotted against deep-layer (0–6 km) bulk shear for null, all tornado, outbreak, and significant tornado cases. Only nonzero CAPE cases are shown. Lines of constant bulk Richardson numbers of 1, 10, and 50 are shown as black lines.

deep-layer shear and nonzero CAPE appeared to discern significant tornadoes, there were too few cases to make a definitive classification. Additionally, there did not appear to be a threshold of bulk Richardson number (BRN, defined as a unitless ratio of CAPE to deep-layer shear; Glickman 2000) between null, tornado, outbreak, and significant tornado cases with 99% of null and 82% of tornado cases with a BRN less than 10. Weisman and Klemp (1982) found that supercells are favored with BRN between 10 and 50 and multicellular storms for BRN greater than 45. BRN values less than 10 were found to have too strong of shear for storm development (Weisman and Klemp 1982). Because the majority of tornadic storms in the British Isles occur with BRN less than 10, perhaps these thresholds are not relevant. Additionally, the low-CAPE, high-shear tornado environment could explain the lower intensity of tornadoes compared to the United States.

There was no significant difference in mean CIN between the null and tornado cases ($p = 0.25$, Fig. 17d). Conversely, tornadic supercells east of the Rocky Mountains in the United States had less CIN than nontornadic cases (Davies 2004). CIN values in British Isles tornado cases, with a mean of 10 J kg^{-1}, were smaller than those in the United States, with a mean of 30 J kg^{-1} (Grams et al. 2012). Tornado outbreaks in the British Isles had less mean CIN than in all tornado cases ($p = 0.02$). However, because the difference in means was small, CIN is not a useful forecasting parameter for tornado outbreaks.

The mean LCL heights in tornado and outbreak cases were lower than in null cases ($p = 0.01$ and $p = 0.01$, respectively, Fig. 17e). Additionally, outbreak mean LCL heights were lower than that for all tornado cases ($p < 0.01$). However, there were no significant differences between mean significant tornado LCL heights and all tornado cases ($p > 0.05$). In contrast, in the contiguous United States, significant tornadoes tended to have lower LCLs than all other cases with 75% of significant tornado cases occurring with LCL heights less than 1200 m AGL (during 1997–99; Craven and Brooks 2004). In 90% of tornado and 88% of null cases in the British Isles, LCL heights were less than 1200 m, making the 1200 m AGL threshold for significant tornadoes suggested by Craven and Brooks (2004) of little forecasting use in the British Isles. We do not suggest an alternative threshold for LCL height to distinguish between null and tornado cases because the difference in means was small, even though it was statistically significant.

The mean LFC height did not differ significantly between null and tornado cases ($p > 0.05$, Fig. 17f). Although outbreak and significant tornado cases appeared to have lower LFC heights than all tornado cases, these were also not statistically significant ($p > 0.05$). Similar to LCL heights, LFC heights tended to be lower in the British Isles than in the United States, where the median LFC height for supercells with F0–F1 tornadoes was 1871 m and nontornadic supercells had a median LFC height of 2338 m (Davies 2004). In the British Isles, 84% of null and 82% of tornado cases were below 1871 m.

Because of the lack of clear thresholds, forecasting tornadoes in the British Isles based solely on sounding-based parameters is more difficult than doing so in the United States. The exception is that significant tornadoes are unlikely in deep-layer shear of less than 20 m s^{-1}.

9. Summary

This paper analyzed 1241 tornadoes during 1980–2012 in the British Isles to determine when, where, from what parent storm, and in what environment tornadoes form, finding the following:

- There were a mean of 34.3 and a median of 26 tornadoes, a mean of 19.5 and a median of 18 tornado days, and a mean of 2.5 and a median of 2 outbreaks per year over the 33 years.
- Tornadoes were most common in summer and autumn, whereas tornado days were most common in summer. However, tornadoes occurred throughout the year, so the British Isles tornado season was not as well defined as the United States.
- Tornado outbreaks were most common in autumn.
- The most common storm morphology producing tornadoes in the British Isles was linear storms

(42%), contrary to the United States, where only 18% of tornadoes were produced from linear storms (Trapp et al. 2005).
- Tornado outbreaks were produced by linear storms 51% of the time. Outbreaks consisted of relatively few tornadoes with 90.2% consisting of 3–10 tornadoes.
- Tornadoes in the British Isles were weaker than those in the United States, likely because linear storms tend to produce weaker tornadoes than supercells (Trapp et al. 2005; Grams et al. 2012) and because of the weaker instability in the British Isles compared to that in the United States.
- Tornadoes in the British Isles are more difficult to forecast using sounding-based parameters than they are in the United States because of the lack of clear thresholds between null and tornadic events. The exception is in forecasting significant tornadoes, which are unlikely to occur in deep-layer shear less than $20\,m\,s^{-1}$.

Acknowledgments. We thank TORRO for providing tornado occurrence data, specifically Terence Meaden and Paul Brown. We thank the Department of Atmospheric Science, University of Wyoming for their radiosonde archive, the National Climatic Data Center Storm Events Database for U.S. tornado data, the British Atmospheric Data Centre and the Met Office for providing Nimrod system radar data, the Met Office Integrated Data Archive System for providing SYNOPs and surface analysis charts, and the European Environment Agency for the population density data. We thank Bogdan Antonescu and Hugo Ricketts for their help on the radiosonde analysis and Jonathan Fairman for assistance with the Nimrod radar dataset. We thank Pieter Groenemeijer, David Smart, Peter Kirk, and two anonymous reviewers for their comments that improved this manuscript. We also thank Mulder's Ph.D. committee, Geraint Vaughan and Paul Connolly. Mulder was funded by a scholarship from the Faculty of Engineering and Physical Sciences, University of Manchester. Partial funding for Schultz was provided by the U.K. Natural Environment Research Council to the University of Manchester for the Diabatic Influences on Mesoscale Structures in Extratropical Storms (DIAMET) project (Grant NE/I005234/1) and the Tropopause Folding, Stratospheric Intrusions and Deep Convection (TROSIAD) project (Grant NE/H008225/1).

REFERENCES

Bolton, N., D. M. Elsom, and G. T. Meaden, 2003: Forecasting tornadoes in the United Kingdom. *Atmos. Res.,* **67–68,** 53–72, doi:10.1016/S0169-8095(03)00083-8.

Brooks, H. E., 2009: Proximity soundings for severe convection for Europe and the United States from reanalysis data. *Atmos. Res.,* **93,** 546–553, doi:10.1016/j.atmosres.2008.10.005.

——, and C. A. Doswell III, 2001: Some aspects of the international climatology of tornadoes by damage classification. *Atmos. Res.,* **56,** 191–201, doi:10.1016/S0169-8095(00)00098-3.

——, ——, and M. P. Kay, 2003a: Climatological estimates of local daily tornado probability for the United States. *Wea. Forecasting,* **18,** 626–640, doi:10.1175/1520-0434(2003)018<0626:CEOLDT>2.0.CO;2.

——, J. W. Lee, and J. P. Craven, 2003b: The spatial distribution of severe thunderstorm and tornado environments from global reanalysis data. *Atmos. Res.,* **67–68,** 73–94, doi:10.1016/S0169-8095(03)00045-0.

Clark, M. R., 2012: Doppler radar observations of non-occluding, cyclic vortex genesis within a long-lived tornadic storm over southern England. *Quart. J. Roy. Meteor. Soc.,* **138,** 439–454, doi:10.1002/qj.924.

——, 2013: A provisional climatology of cool-season convective lines in the UK. *Atmos. Res.,* **123,** 180–186, doi:10.1016/j.atmosres.2012.09.018.

Craven, J. P., and H. E. Brooks, 2004: Baseline climatology of sounding derived parameters associated with deep moist convection. *Natl. Wea. Dig.,* **28,** 13–24.

Davies, J. M., 2004: Estimations of CIN and LFC associated with tornadic and nontornadic supercells. *Wea. Forecasting,* **19,** 714–726, doi:10.1175/1520-0434(2004)019<0714:EOCALA>2.0.CO;2.

Dixon, P. G., A. E. Mercer, J. Choi, and J. S. Allen, 2011: Tornado risk analysis: Is Dixie Alley an extension of Tornado Alley? *Bull. Amer. Meteor. Soc.,* **92,** 433–441, doi:10.1175/2010BAMS3102.1.

Doswell, C. A., III, 1991: Comments on "Mesoscale convective patterns of the southern high plains." *Bull. Amer. Meteor. Soc.,* **72,** 389–390.

——, and E. N. Rasmussen, 1994: The effect of neglecting the virtual temperature correction on CAPE calculations. *Wea. Forecasting,* **9,** 625–629, doi:10.1175/1520-0434(1994)009<0625:TEONTV>2.0.CO;2.

Elsom, D. M., 1985: Tornadoes in Britain: Where, when and how often. *J. Meteor. (UK),* **10,** 203–211.

——, and G. T. Meaden, 1984: Spatial and temporal distributions of tornadoes in the United Kingdom 1960-1982. *Weather,* **39,** 317–323, doi:10.1002/j.1477-8696.1984.tb06727.x.

——, ——, D. J. Reynolds, M. W. Rowe, and J. D. C. Webb, 2001: Advances in tornado and storm research in the United Kingdom and Europe: The role of the Tornado and Storm Research Organisation. *Atmos. Res.,* **56,** 19–29, doi:10.1016/S0169-8095(00)00084-3.

Gagan, J. P., A. Gerard, and J. Gordan, 2010: A historical and statistical comparison of "Tornado Alley" to "Dixie Alley." *Natl. Wea. Dig.,* **34,** 145–155.

Gallus, W. A., Jr., N. A. Snook, and E. V. Johnson, 2008: Spring and summer severe weather reports over the Midwest as a function of convective mode: A preliminary study. *Wea. Forecasting,* **23,** 101–113, doi:10.1175/2007WAF2006120.1.

Glickman, T., Ed., 2000: *Glossary of Meteorology.* 2nd ed. Amer. Meteor. Soc., 855 pp.

Grams, J. S., R. L. Thompson, D. V. Snivley, J. A. Prentice, G. M. Hodges, and L. J. Reames, 2012: A climatology and comparison of parameters for significant tornado events in the United States. *Wea. Forecasting,* **27,** 106–123, doi:10.1175/WAF-D-11-00008.1.

Hales, J. E. J., 1988: Improving the watch/warning program through use of significant event data. Preprints, *15th Conf. on*

Severe Local Storms, Baltimore, MD, Amer. Meteor. Soc., 165–168.

Holden, J., and A. Wright, 2004: UK tornado climatology and the development of simple prediction tools. *Quart. J. Roy. Meteor. Soc.,* **130,** 1009–1021, doi:10.1256/qj.03.45.

Holley, D. M., S. R. Dorling, C. J. Steele, and N. Earl, 2014: A climatology of convective available potential energy in Great Britain. *Int. J. Climatol.,* **34,** 3811–3824, doi:10.1002/joc.3976.

Kirk, P. J., 2007: UK tornado climatology 1980–2004. *J. Meteor. (UK),* **32,** 158–172.

——, 2014: An updated tornado climatology for the UK: 1981–2010. *Weather,* **69,** 171–175, doi:10.1002/wea.2247.

Lacy, R. E., 1968: Tornadoes in Britain during 1963–6. *Weather,* **23,** 116–124, doi:10.1002/j.1477-8696.1968.tb07358.x.

Meaden, G. T., 1985a: A study of tornadoes in Britain with assessments of the general tornado risk potential and the specific risk potential at particular regional sites. TORRO, and Health and Safety Executive, H.M. Nuclear Installations Inspectorate, Bradford-on-Avon, United Kingdom, 131 pp.

——, 1985b: TORRO, The Tornado and Storm Research Organization: The main objectives and scope of the network. *J. Meteor. (UK),* **10,** 182–185.

——, S. Kochev, L. Kolendowicz, A. Kosa-Kiss, I. Marcinoniene, M. V. Sioutas, H. Tooming, and J. Tyrrell, 2007: Comparing the theoretical versions of the Beaufort scale, the T-Scale and the Fujita scale. *Atmos. Res.,* **83,** 446–449, doi:10.1016/j.atmosres.2005.11.014.

NCDC, cited 2014: U.S. tornado climatology. [Available online at http://www.ncdc.noaa.gov/climate-information/extreme-events/us-tornado-climatology.]

Rauhala, J., and D. M. Schultz, 2009: Severe thunderstorm and tornado warnings in Europe. *Atmos. Res.,* **93,** 369–380, doi:10.1016/j.atmosres.2008.09.026.

——, H. E. Brooks, and D. M. Schultz, 2012: Tornado climatology of Finland. *Mon. Wea. Rev.,* **140,** 1446–1456, doi:10.1175/MWR-D-11-00196.1.

Reynolds, D. J., 1999: A revised U.K. tornado climatology, 1960–1989. *J. Meteor. (UK),* **24,** 290–321.

Romero, R., M. Gayà, and C. A. Doswell III, 2007: European climatology of severe convective storm environmental parameters: A test for significant tornado events. *Atmos. Res.,* **83,** 389–404, doi:10.1016/j.atmosres.2005.06.011.

Rowe, M., 1985: Britain's greatest tornadoes and tornado outbreaks. *J. Meteor. (UK),* **10,** 212–220.

——, 1999: 'Work of the devil': Tornadoes in the British Isles to 1660. *J. Meteor. (UK),* **24,** 326–338.

Russell, A., 2010: Wild weather: The 2005 Birmingham tornado. [Available online at http://news.bbc.co.uk/local/birmingham/hi/people_and_places/newsid_8973000/8973381.stm.]

Smith, B. T., R. L. Thompson, J. S. Grams, C. Broyles, and H. E. Brooks, 2012: Convective modes for significant severe thunderstorms in the contiguous United States. Part I: Storm classification and climatology. *Wea. Forecasting,* **27,** 1114–1135, doi:10.1175/WAF-D-11-00115.1.

Trapp, R. J., S. A. Tessendorf, E. S. Godfrey, and H. E. Brooks, 2005: Tornadoes from squall lines and bow echoes. Part I: Climatological distribution. *Wea. Forecasting,* **20,** 23–34, doi:10.1175/WAF-835.1.

Tyrrell, J., 2003: A tornado climatology for Ireland. *Atmos. Res.,* **67–68,** 671–684, doi:10.1016/S0169-8095(03)00080-2.

Weisman, M. L., and J. B. Klemp, 1982: The dependence of numerically simulated convective storms on vertical wind shear and buoyancy. *Mon. Wea. Rev.,* **110,** 504–520, doi:10.1175/1520-0493(1982)110<0504:TDONSC>2.0.CO;2.

[Blank page]

Chapter 3

Paper 2: Sensitivity Tests of a WRF Simulated Tornadic Narrow Cold Frontal Rainband in the United Kingdom

[Blank page]

Sensitivity Tests of a WRF Simulated Tornadic Narrow Cold Frontal Rainband in the United Kingdom

Kelsey J. Mulder * and David M. Schultz

Centre for Atmospheric Science, School of Earth, Atmospheric and Environmental Sciences, University of Manchester, United Kingdom

ABSTRACT

This article tested parameterization schemes for the Advanced Research Weather and Forecasting Model to simulate a narrow cold frontal rain band (NCFR). The NCFR occurred on 29 November 2011 and produced seven observed tornadoes in Wales and northern England. The parameters tested were initialization time, planetary boundary layer scheme, microphysics scheme, and land-surface scheme. The most accurate simulation, when compared to radar reflectivity and near-surface temperature, relative humidity, wind speed, wind direction, and sea-level pressure, and considering computational expense used 2-way nesting and was initialized at 1200 UTC 29 November 2011 using the Mellor-Yamada-Janjic planetary boundary layer, Thompson microphysics, and Five-Layer Thermal Diffusion land-surface schemes.

1. Introduction

In the British Isles, the most common parent storm type for tornadoes is linear convection (Mulder and Schultz 2015). Although tornadoes from linear storms tend to produce less damage than those from supercells (Trapp et al. 2005; Grams et al. 2012), tornadoes in the British Isles still threaten life and property. In addition, these tornadoes tend to develop under low-CAPE, high-shear environments (e.g., Smart and Browning 2009; Mulder and Schultz 2015), environments in which high false alarm rates have been noted in the United States (Dean and Schneider 2008). Therefore, it is important to understand the dynamics of vortexgenesis and tornadogenesis in linear storms, particularly in low-CAPE, high-shear environments.

To help improve knowledge of the origin of vorticity in linear convection, a case study was conducted on a tornadic narrow cold frontal rainband (NCFR) that traversed Wales and northern England (Chapter 4 of this thesis). To conduct the case study, it was important to ensure the simulation modeling the NCFR was realistic. Therefore, we tested different combinations of parameterizations and initialization times to identify the simulation most closely resembling the observed radar reflectivity. The parameters tested were planetary boundary layer scheme, microphysics scheme, and land-surface scheme. The purpose of this paper is to present the results of sensitivity tests in modeling the NCFR on 29 November 2011. This will be accomplished by analyzing the shape and extent of the NCFR from radar reflectivity the NCFR at 1300, 1400, 1500, and 1600 UTC. Additionally, temperature at 2 meters above ground level, relative humidity at 2 meters above ground level, wind speeds at 10 meters above ground level, and sea-level pressure will be compared at 1500 UTC. These parameters were analyzed at 1300, 1400, and 1600 UTC as well with similar results, however to prevent repetition and save space, the analysis shown herein will only be for 1500 UTC.

The NCFR on 29 November 2011 produced at least seven observed tornadoes ranging from T1 to T4 (or F0 to F2) in Wales and northern England (Fig. 1). Previous studies on tornadic linear convection have concerned either bow echoes (e.g., Trapp and Weisman 2003) or exhibited a broken-S pattern (e.g., McAvoy et al. 2000; Clark 2011), bulge (Clark 2011; Clark and Parker 2014), or core and gap structure (e.g., Jorgensen et al. 2003; Smart and Browning 2009; Kawashima 2011). The NCFR in this case produced tornadoes from radar reflectivity exhibiting an S pattern (tornadoes 2 and 5), bulge (tornado 6), and core and gap (tornado 7) (circled and annotated in Fig. 1). However, there was no radar reflectivity signature associated with tornadoes 1, 3, and 4.

It is possible that there was a small wave, hook, or bulge associated with these tornadoes, but the resolution of the radar was too coarse to capture it. An additional shortcoming with radar data is the possible shielding of radar beams due to mountainous terrain. This can yield unrealistic radar reflectivity values, especially over the Pennine Mountains in northwest England.

At 1300 UTC, the NCFR made landfall with leading stratiform precipitation (hereafter considered reflectivity

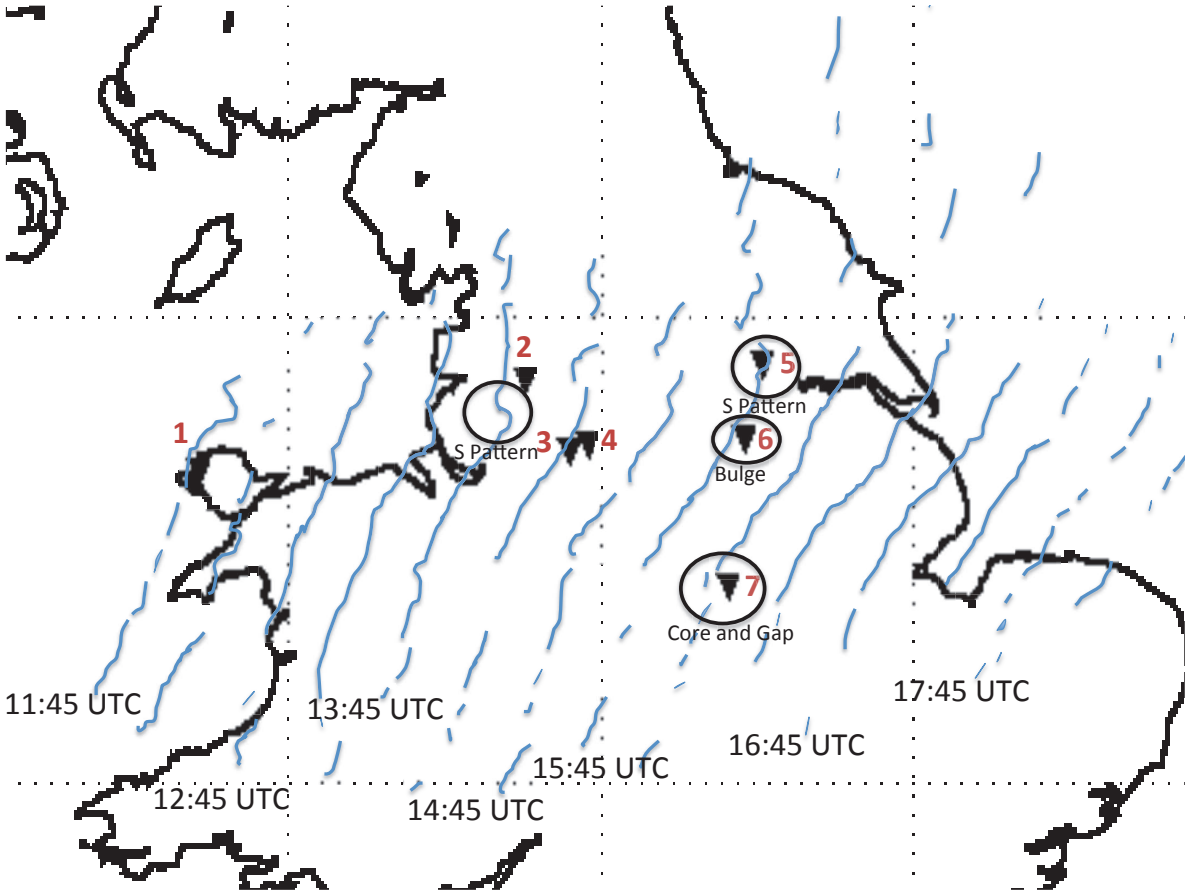

FIG. 1. Map of northern England and Wales showing the sequence of the 15 mm hr^{-1} instantaneous rain rate from Nimrod radar 5-minute composite rainfall rates every 30 minutes (solid blue lines) and the locations of the tornadoes (inverted black triangles). Although the contours of 15 mm hr^{-1} were typically thin, the thickness of the lines do not represent the thickness of the instantaneous rain rate contour, but instead the shape of the eastern edge of the 15 mm hr^{-1} contour.

between 25–40 dBZ, seen as the green reflectivity) ahead of the front to the south and trailing stratiform precipitation behind the front to the north (Fig. 2a). The NCFR at this time was irregular as the higher reflectivity (45–55 dBZ, yellow, orange, and red, hereafter considered the NCFR) appeared jagged with intermittent gaps in the line (Fig. 2a). The southern end of the NCFR was unorganized at this time.

The NCFR was more organized and nearly straight at 1400 UTC (Fig. 2b). There were few gaps between high reflectivity within the NCFR. There were two broken S patterns (McAvoy et al. 2000) along the line at this timestep (indicated by the black arrows in Fig. 2b). The southern and northern end of the NCFR had organized into broken linear convection between 1300 and 1400 UTC (Fig. 2b). Also at this time, the leading stratiform precipitation south of the NCFR from Fig. 2a organized into a line of convection (labelled as "Leading Convective Line" in Fig. 2b). The trailing stratiform precipitation west of the NCFR from 1300 UTC (Fig. 2a) was still present at 1400 UTC (Fig. 2b).

At 1500 UTC, the NCFR continued to be organized in a nearly straight line, except for a slight bulge in the middle of the NCFR (indicated by the blue arrow in Fig. 2c). The reflectivity in the NCFR became stronger at 1500 UTC with highest reflectivity up to 55 dBZ (Fig. 2). There were few gaps in the highest reflectivity, similar to the NCFR at 1400 UTC. The broken linear convection that developed north and south of the NCFR at 1400 UTC (Fig. 2b) was still present at 1500 UTC (Fig. 2c). However, only the northern broken S pattern from Fig. 2b was present at 1500 UTC (indicated by the black arrow in Fig. 2c). Additionally, the leading convective line appeared more linear (Fig. 2c). At 1500 UTC, the trailing stratiform precipitation became heavier, with areas of precipitation up to 45 dBZ (circled in Fig. 2c). The increase in precipitation

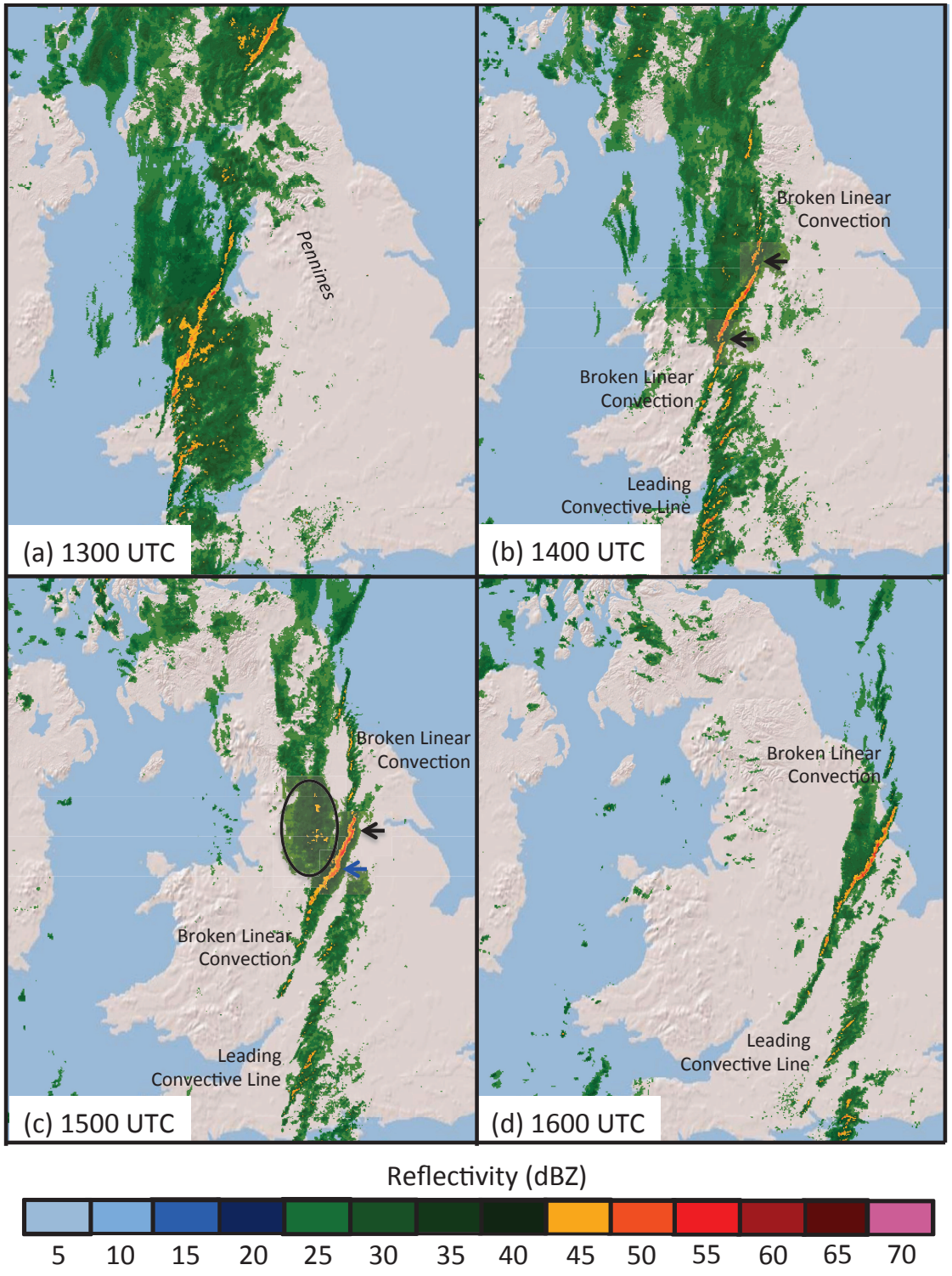

FIG. 2. Observed radar reflectivity from UK Met Office Nimrod radar 5-minute composite rainfall rates at (a) 1300 UTC, (b) 1400 UTC, (c) 1500 UTC, and (d) 1600 UTC 29 November 2011. The location of the Pennine Mountains are labelled in (a). The black arrows in (b) indicate the broken S signatures. The black arrow in (c) indicates the northern broken S signature from (b). The blue arrow in (c) indicates an area of bulging reflectivity. The circled region in (c) points out the area of orographically enhanced rainfall over the Pennines.

intensity was likely due to orographic enhancement of precipitation by the Pennies (labelled in Fig. 2a). The increase of precipitation due to orography has been noted before in both observed (e.g., Hill et al. 1981) and simulated (e.g., Colle et al. 2002; Jones 2013) cold fronts.

At 1500 UTC, the temperature across the cold front varied from 4–6°C (locally 0°C) behind the front and up to 14°C ahead of the front (Fig. 3a). Wind speeds were up to 35 knots behind the front, coming from the west northwest. Ahead of the front, wind speeds were up to 40 knots and coming from the southwest, oriented parallel to the front. Along and directly ahead of the front, relative humidity values were between 90–100% (Fig. 3b). Farther east and west of the front, humidity values were down to between 70–80%. The location of the front can be seen as a kink in the sea-level pressure contours (Fig. 3c).

The NCFR at 1600 UTC was still nearly linear (Fig. 2d). However, gaps between the highest reflectivity in the NCFR began to appear at this time (Fig. 2d). Neither the bulge nor the broken S pattern from 1500 UTC (Fig. 2c) were present at 1600 UTC (Fig. 2d). Additionally, only the broken linear convection north of the NCFR was still present at 1600 UTC (Fig. 2d). The leading convective line organized into broken linear convection at 1600 UTC (Fig. 2d). The trailing stratiform precipitation diminished between 1500 UTC (Fig. 2c) and 1600 UTC (Fig. 2d). This was likely because the NCFR and trailing stratiform precipitation had moved beyond the Pennines and therefore orographic enhancement of precipitation was no longer occurring.

The rest of this article will compare simulations using different parameterization combinations to the observed radar reflectivity from Fig. 2 and observed temperature, relative humidity, and sea-level pressure in Fig. 3. We begin in Section 2 by discussing the methods used in this analysis. Sections 3, 4, 5, and 6 discuss changes in the simulated radar reflectivity, 2-meter temperature, 2-meter relative humidity, and sea-level pressure based on changing initialization times, planetary boundary layer scheme, microphysics scheme, and land-surface scheme, respectively. This article concludes with a summary in Section 7.

2. Methods

The simulations were produced by the Advanced Research Weather and Forecasting Model version 3.4.1 (WRF-ARW, Skamarock et al. 2008) using European Centre for Medium-Range Weather Forecasting (ECMWF) initial data interpolated onto a Lambert conformal grid. There were 90 vertical levels. Four nested domains were used in the simulation. The largest domain, D01, had 25-km horizontal grid spacing to capture the synoptic scale processes and covered the North Atlantic Ocean, the United Kingdom, and part of Eastern Europe (Figure 4). The Kain–Fritsch cumulus parameterization scheme was used on D01 (Kain 2004), but was turned off on all nested domains where convection was explicitly represented. D02 had 5-km horizontal grid spacing to model the mesoscale. It covered the United Kingdom, Republic of Ireland, and northeastern Atlantic Ocean. D03, with 1-km horizontal grid spacing, was used to resolve the storm-scale features and was centered over England. D04 had 200-m horizontal grid spacing to resolve the vortices along the NCFR. Although four domains were calculated for the case study, only results from D03 are presented herein to show the shape and size of the modeled NCFR rather than the small-scale details, which will be detailed in Chapter 4 of this thesis.

The parameters tested in this article were initialization time, planetary boundary layer scheme, microphysics scheme, and land-surface scheme. One- versus two-way nesting was also tested, but the differences in the resulting simulations were minimal and therefore are not discussed herein. The final simulation was chosen out of 96 total simulations with different parameterization combinations. For brevity, outputs of all 96 simulations were not shown. The examples shown in this article were chosen so that the overall best simulation was the control simulation, compared to other simulations with only one parameter changed.

3. Initialization Time

Model initialization time can impact the output both if the model is initialized too early or too close to the time of analysis. Initializing the model with too much lead-time can introduce convection in the wrong place, for example, into the model that can propagate and worsen over time. On the other hand, the model requires time to spin-up from the initial conditions and analysis during the spin-up time can produce misleading results. Spin-up time depends on grid size and length of time steps. With finer grid spacing and shorter time-steps, the overall spin-up time is decreased. Therefore, the spin-up time between a global climate model and a storm-scale model are vastly different. Keeping all other parameters the same, the models were initialized at 1800 UTC 28 November, 0000 UTC 29 November, 0600 UTC 29 November, and 1200 UTC 29 November.

As the initialization time approached the time of analysis, the NCFR moved north in the domain (Fig. 5a compared with d), closer to where the NCFR was in observed radar reflectivity (Fig. 2). The 1800 UTC 28 November simulation valid at 1300 was essentially a line of broken linear convection (Fig. 5a). As the simulation progressed to 1600 UTC, a poorly-defined NCFR developed in southern England (circled in Fig. 5a), where the broken linear convection occurred in observed reflectivity (Fig. 2). The NCFR had many breaks and bulges in the reflectivity in all time steps from 1300 to 1600 UTC (Fig. 5). Unlike the

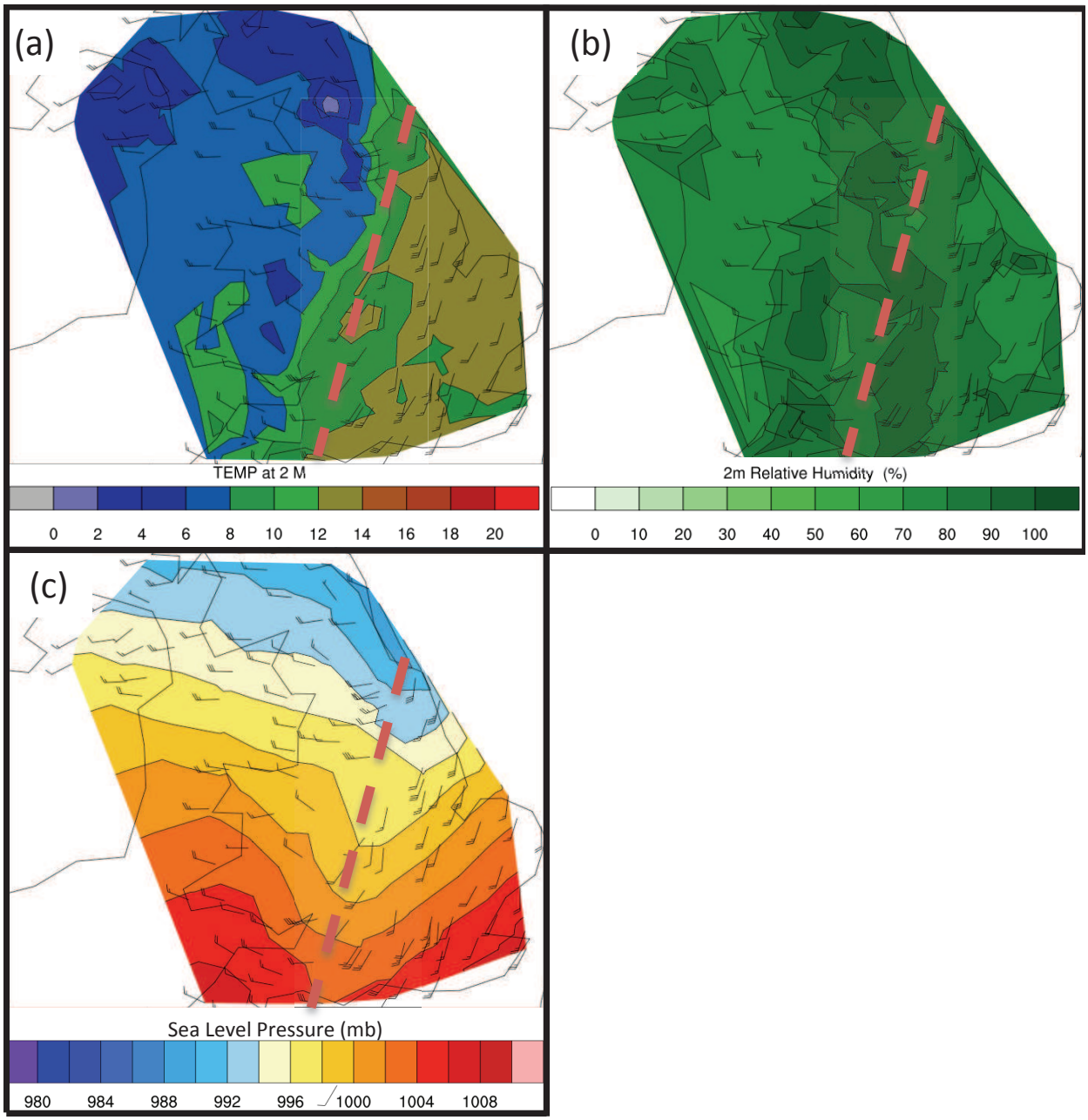

FIG. 3. Surface parameters interpolated from UK Met Office observations at 1500 UTC 29 November 2011. Parameters shown are (a) temperature at 2 meters above ground level in °C, (b) relative humidity at 2 meters above ground level in percent, and (c) sea-level pressure in millibars. Wind speed (knots) and direction at 10 meters above ground level are overlaid on (a), (b), and (c). The approximate location of the front is shown by the dashed red line.

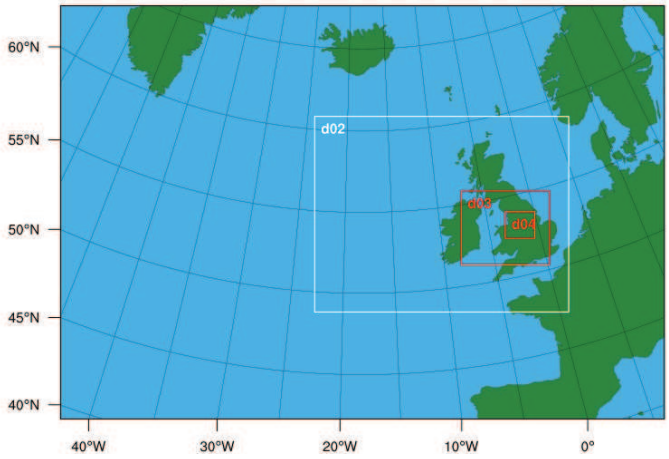

FIG. 4. Map showing the location and sizes of the WRF-ARW model domains described in the text. D01 (size of full image), D02 (white box), D03 (outer red box), and D04 (inner red box) had 25-km, 5-km, 1-km, and 200-m horizontal grid spacing, respectively.

observed reflectivity, the modeled broken linear convection was oriented nearly perpendicular to the line rather than parallel to the line in the observed reflectivity (examples shown by the arrows in Fig. 5a). The shape of the NCFR at 1600 UTC had few bulges (Fig. 5a), but there were gaps between lighter precipitation (40–50 dBZ) and the heaviest precipitation (50–60 dBZ). There was little stratiform precipitation associated with the NCFR, unlike observed reflectivity. The NCFR in the 1800 UTC simulation did not fully develop until 1500 or 1600 UTC. When the NCFR did develop, the shape was similar to observed reflectivity, although there were many gaps in the NCFR. Additionally, the NCFR was located too far south.

Similar to the 1800 UTC 28 November simulation, the 0000 UTC 29 November simulation produced broken linear convection at 1300 and 1400 UTC (Fig. 5b). At 1500 and 1600 UTC, an NCFR developed in southern England (Fig. 5b), again farther south than observed reflectivity (Fig. 2). The simulated NCFR initialized at 0000 UTC, valid at 1500 and 1600 UTC, had fewer breaks and bulges in the reflectivity than the simulation initialized at 1800 UTC, valid at the same times (circled in Fig. 5b). In the simulation initialized at 0000 UTC, the extent of the broken linear convection was farther north than that in the 1800 UTC simulation (Fig. 5b compared to a), closer to the location of the NCFR in the observed reflectivity (Fig. 2). However, the broken linear convection was oriented nearly perpendicular to the line, similar to the 1800 UTC simulation (arrows in Fig. 5b), unlike the observed reflectivity. Again, there was little stratiform precipitation associated with the 0000 UTC simulation.

In the simulation initialized at 0600 UTC 29 November, there was an NCFR in northern England at 1300 UTC (circled in Fig. 5c). However, the NCFR did not extend as far northeast or southwest as that in the observed reflectivity (Fig. 2). The simulated NCFR broke down into smaller segments at 1400, 1500, and 1600 UTC (Fig. 5c), rather than remaining a long, nearly-continuous line of precipitation (Fig. 2). The segments of the broken linear convection at all times were oriented nearly parallel to the line (examples shown by arrows in Fig. 5c), more similar to the observed reflectivity than the 1800 UTC and 0000 UTC simulations. There was still very little stratiform precipitation in the 0600 UTC simulation.

The simulation initialized at 1200 UTC 29 November produced an NCFR in northern England that had a similar location and extent as the observed reflectivity at 1300, 1400, 1500, and 1600 UTC (Fig. 5d). The NCFR did not turn into broken linear convection, like the other initialization times. The broken linear convection that was present occurred south and east of the NCFR at 1400, 1500, and 1600 UTC (Fig. 5d), similar to observed reflectivity (Fig. 2). However, the leading convective line, especially at 1600 UTC (circled in Fig. 5d), was located much farther east of the NCFR than in the observed reflectivity. Most of the broken linear convection south of the NCFR was oriented nearly parallel to the line, similar to the observed reflectivity. Along the NCFR, the simulation showed more bowing segments than observed reflectivity at 1400 UTC (shown by arrows in Fig. 5d). There was more stratiform precipitation in the simulation initialized at 1200 UTC, but it was still less widespread than observed reflectivity (Fig. 2).

There were only small differences in the 2-meter temperatures between the initialization time simulations (Fig. 6). The air ahead of the front in the simulated reflectivity was not as warm in the simulations as observed with the 12–14°C contour being lest widespread as in the observed (Fig. 3a compared with Fig. 6). The air behind the front was similar in temperature to the observed of 4–6°C. The 10-meter wind speeds and directions and the sea-level pressure were similar between the different initialization times and between the simulations (Fig. 6) and observed (Fig. 3c). The relative humidity for the simulation initialized at 1200 UTC 29 November (Fig. 7d) was slightly different than the other initialization times (Fig. 7a, b, and c). In the simulation initialized at 1200 UTC, there was a curved appearance in the line of relative humidity between 80–90% and 90–100% (Fig. 7d), rather than a jagged straight line in the other simulations (Fig. 7a, b, and c). Otherwise, the relative humidity was very similar between the initialization times. The air ahead of the front was more humid in the simulations than the observed reflectivity, with a widespread contour of 90–100% relative humidity (Fig. 7 compared to Fig. 3b).

All initialization times tested produced an NCFR with broken linear convection, even if the NCFR was located

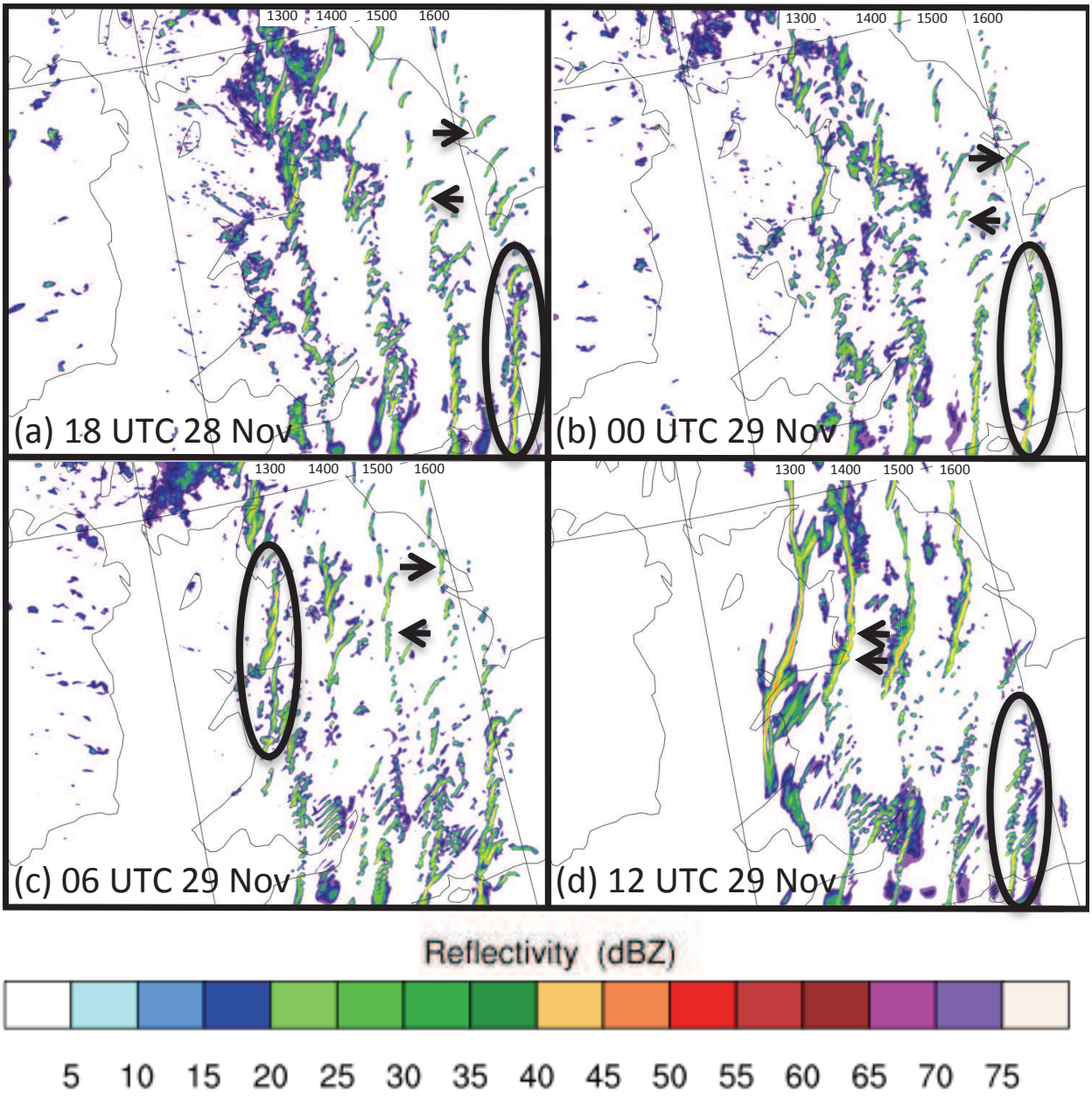

FIG. 5. Changes in model-simulated radar reflectivity due to different initialization times for simulations valid at 1300, 1400, 1500, and 1600 UTC 29 November 2011. Simulations were initialized (a) 1800 UTC 28 November, (b) 0000 UTC 29 November, (c) 0600 UTC 29 November, and (d) 1200 UTC 29 November. All panels used Five-Layer Thermal Diffusion land-surface physics, Mellor-Yamada-Janjic planetary boundary layer, Thompson et al. microphysics, and 2-way nesting. See text for more information on the circles and arrows.

too far south when compared to observed reflectivity. The differences between the simulations were mostly in the location, extent, shape, and longevity of the NCFR. The simulations initialized at 1800 UTC 28 November and 0000 UTC 29 November produced broken linear convection that merged into NCFRs in southern England valid at 1500 and 1600 UTC, rather than in northern England like the observed reflectivity. The NCFRs were segmented with broken linear convection oriented perpendicular to the line, unlike in the observed reflectivity. The simulation initialized at 0600 UTC, valid at 1300 UTC, produced an NCFR in northern England, but the NCFR was short and seg-

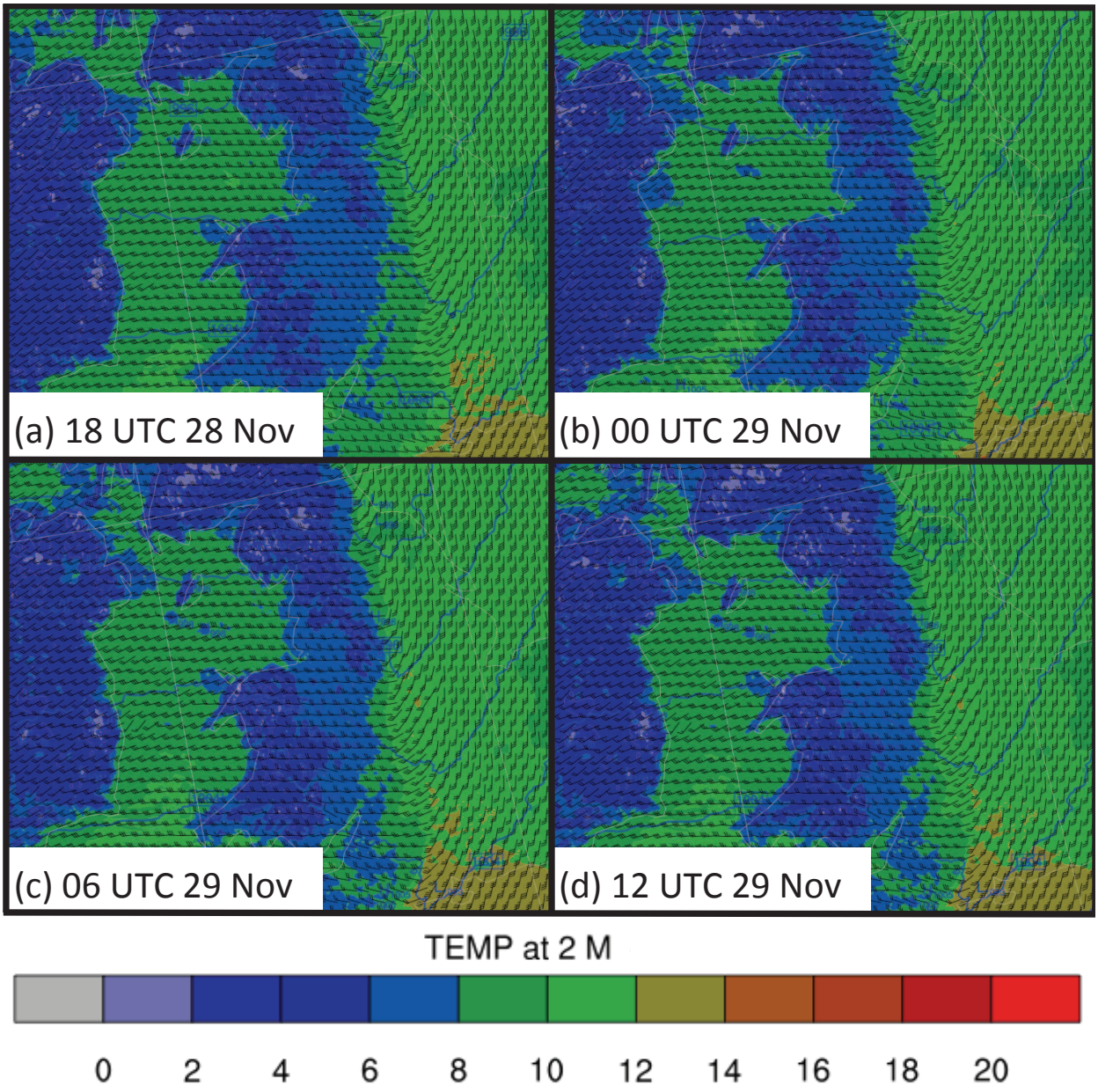

FIG. 6. Same as Fig. 5, but showing temperature at 2 meters above ground level in °C. Wind speed (knots) and direction at 10m above ground level are shown as the black wind barbs. All parameters are valid at 1500 UTC.

mented and did not extend as far as that in the observed reflectivity. Additionally, the NCFR segmented into broken linear convection at 1400, 1500, and 1600 UTC. The simulation initialized at 1200 UTC 29 November had more bulges than the other initialization times, but the NCFR was simulated in the correct location and was similar in length as the observed reflectivity. In addition, the broken linear convection associated with the simulation initialized at 1200 UTC was oriented nearly parallel to the line. Comparing the four initialization times, it is clear that the 1200 UTC simulation was the most successful of those tested, likely because the initial conditions are proximate in time to the analysis, meaning the model could not run away with spurious solutions. Previous literature has also found that initialization of the WRF model closest to analysis time was most accurate in simulations for a flooding event in the UK (Champion and Hodges 2014) and for snowbands over the English Chanel (Norris et al. 2013).

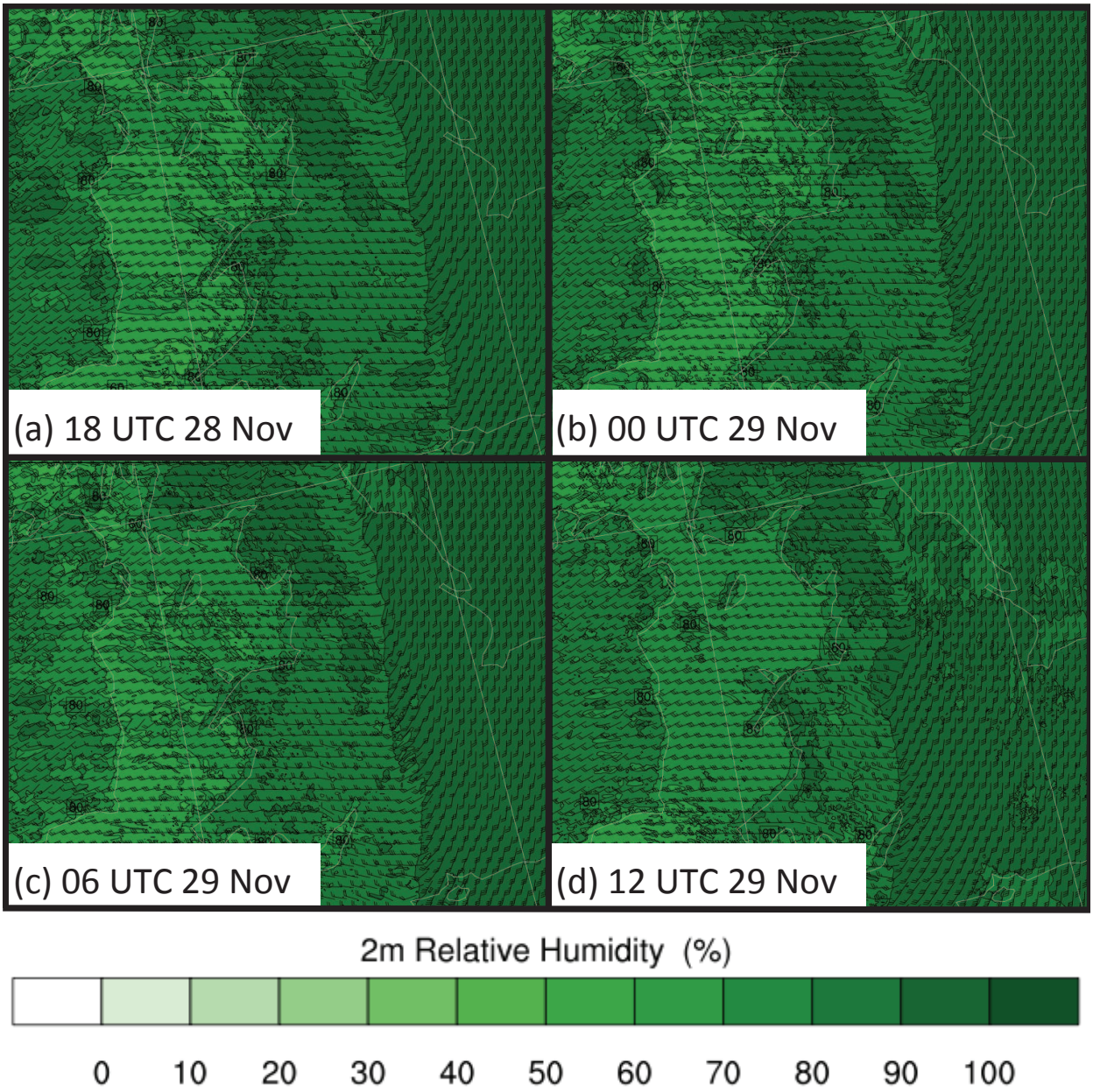

FIG. 7. Same as Fig. 5, but showing relative humidity at 2 meters above ground level. Wind speed (knots) and direction at 10m above ground level are shown as the black wind barbs. All parameters are valid at 1500 UTC.

To assess if the simulation initialized at 1200 UTC 29 November had adequate time to spin up, radar reflectivity at 1215, 1245, 1315, and 1345 were analyzed (Fig. 8). At 1215 UTC, fifteen minutes after model initialization, no precipitation had been resolved (Fig. 8a). Starting at 1245 UTC, a uniform line of precipitation formed along the front over the Irish sea, extreme western Wales, and northern England (Fig. 8c). At 1315 UTC, the NCFR developed bulges along the line (examples shown by arrows in Fig. 8e) and pre-frontal convection began to form in southeastern Wales (circled in Fig. 8e). The shape of the prefrontal convection appeared to be an artifact of model spin up as the observed radar data (Fig. 8f) did not have dozens of bands of pre-frontal precipitation. At 1345 UTC, the pre-frontal precipitation began to break up and the NCFR developed more bulges (Fig. 8g). Stratiform precipitation in northern England west of the NCFR began developing at this time as well.

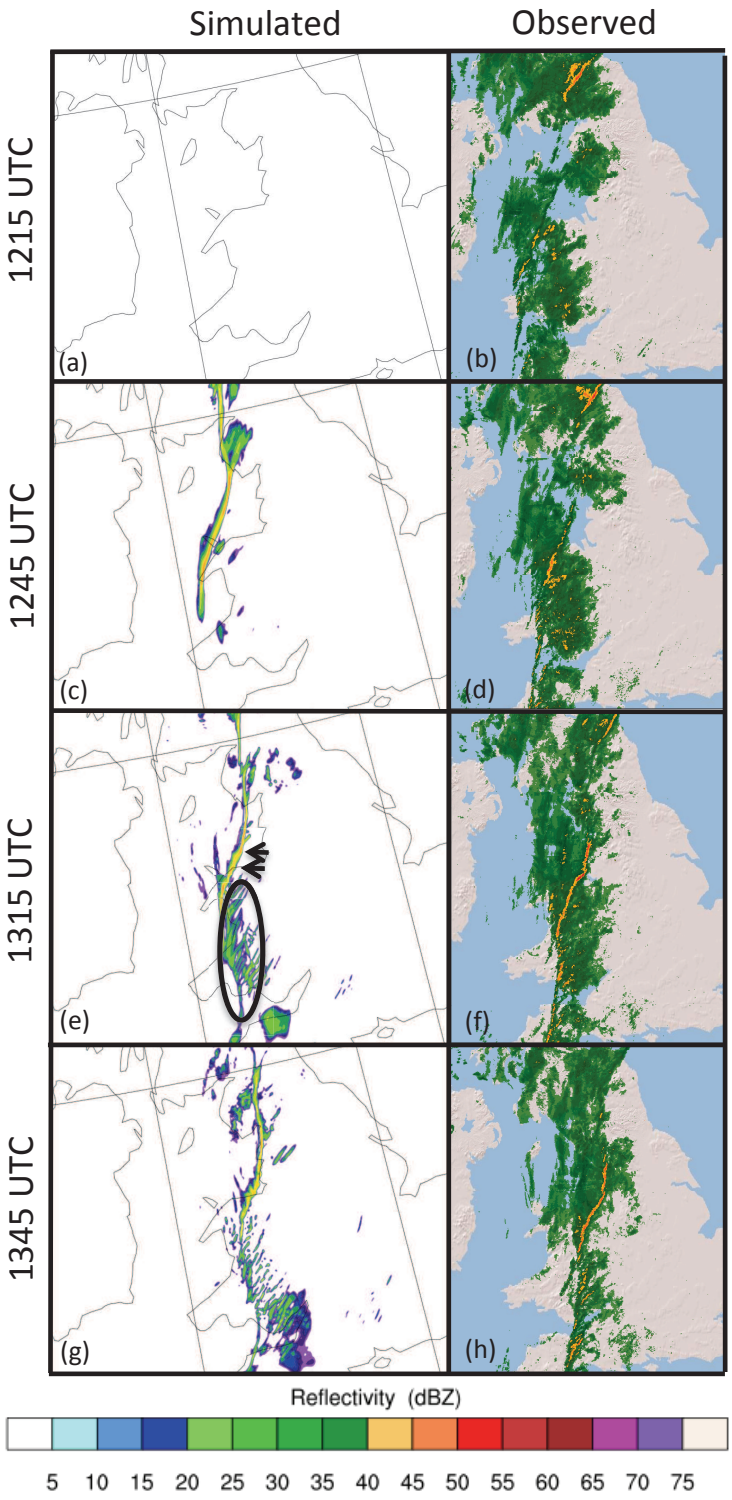

FIG. 8. Model-simulated over time from the model initialized at 1200 UTC 29 November and observed radar reflectivity valid at (a) and (b) 1215 UTC, (c) and (d) 1245 UTC, (e) and (f) 1315 UTC, and (g) and (h) 1345 UTC. Model-simulated reflectivity is shown in (a), (c), (e), and (g). Observed reflectivity is shown in (b), (d), (f), and (h). The model also used Five-Layer Thermal Diffusion land-surface physics, Mellor-Yamada-Janjic planetary boundary layer, Thompson et al. microphysics, and 2-way nesting. See text for more information on the arrows and circles.

Because the shape of the NCFR changed from a uniform line of precipitation into an NCFR with bulges, post-frontal stratiform precipitation, and broken linear convection to the south, it appeared that the model had adequate time to spin up. Previous literature about spin-up times is sparse. The WRF users' frequently asked questions suggests allowing 6–12 hours of spin-up time, but that high-resolution simulations, which therefore include more time steps, have faster spin up time `http://www2.mmm.ucar.edu/wrf/users/FAQ_files/FAQ_wrf_physics.html`. Bryan and Morrison (2012) verified that higher resolution models spin up faster than lower resolution models.

4. Planetary Boundary Layer

The planetary boundary layer (PBL) scheme determines heat, moisture, and momentum fluxes between the boundary layer and surface as well as determining vertical diffusion in the column of the atmosphere. The mixing caused by the PBL scheme can also have an effect on the wind shear, potentially impacting the resulting storm morphology and intensity.

Two PBL schemes were tested here: the Yonsei University (YSU) and the Mellor-Yamada-Janjic (MYJ) schemes, have both been used to simulate severe weather (Janjić 1994; Hong et al. 2006). These two schemes differ in that YSU uses diagnostic, non-local turbulent mixing, meaning the scheme accounts for vertical gradients both in neighboring grid cells and throughout the vertical column. Therefore, in the YSU scheme, small eddies and eddies the size of the PBL are accounted for (Hong et al. 2006). In other words, non-local mixing means adjacent layers can mix as well as non-adjacent layers by small and large eddies, respectively. On the other hand, the MYJ uses prognostic, local turbulent kinetic energy, meaning only adjacent layers can mix (Janjić 1994). As determined in Section 3, the initialization time that best modeled the NCFR was 1200 UTC 29 November. Therefore, the PBL schemes were only compared for the simulations initialized at 1200 UTC.

Both PBL schemes produced NCFRs in northern England (Fig. 9a and b, discussions of c and d are in Section 6), although the NCFRs extended farther north than the observed reflectivity (Fig. 2). The simulations also produced broken linear convection in southern England. However, the broken linear convection extended farther east than the observed reflectivity. Additionally, both simulations produced less widespread pre- and post-frontal stratiform precipitation than what was present in the observed reflectivity. The differences between the PBL simulations were based on the shape of the NCFR, whether or not broken S patterns were simulated, and the magnitudes of temperature and humidity ahead of and behind the front.

The NCFR in the YSU simulation at 1300 UTC was straight with few gaps (Fig. 9a). As the simulation progressed to 1400, 1500, and 1600 UTC, there were more bulges in the NCFR (examples shown by arrows in (Fig. 9a). These bulges were inconsistent with the observed reflectivity (Fig. 2). South of the YSU NCFR, there was a small line of broken linear convection (Fig. 9a), similar to the observed reflectivity (Fig. 2). Additionally, the northern sections of the simulated NCFR were not connected with a broken-S pattern as seen in observed reflectivity.

The NCFR in the MYJ simulation looked similar to the YSU simulation at 1300 UTC (Fig. 9a compared to b). At 1400 UTC, bulges formed in the MYJ simulation, similar to the YSU simulation (examples shown by arrows at 1400 UTC in Fig. 9b). However, by 1500 and 1600 UTC, the NCFR straightened out again and had similar shape to observed radar reflectivity (Fig. 9b compared to Fig. 2). Similar to the observed radar reflectivity, the MYJ simulation produced two broken-S signatures (shown by the arrows at 1500 and 1600 UTC in Fig. 9b), similar to the observed reflectivity (Fig. 2). The bulges at 1400 UTC appeared to turned into the broken S patterns seen in 1500 and 1600 UTC (Fig. 9b), which did not occur in the YSU simulation (Fig. 9a).

The temperature at 2 meters was overall warmer in the YSU simulation, with more widespread temperatures between 12–14°C than the MYJ (Fig. 10a compared to b). The widespread warmer temperatures in the YSU simulation were more similar to the observed temperatures (Fig. 3a). Additionally, the YSU simulation (Fig. 11a) was less humid than the MYJ simulation (Fig. 11b), especially ahead of the front. The less humid environment of the YSU simulation was more similar to the observed relative humidity (Fig. 11a compared to Fig. 3b). The sea-level pressure, wind speed, and wind direction in both the YSU and MYJ simulations were similar to what was observed (Fig. 10a and b compared to Fig. 3b and c).

Because this simulation had 90 vertical levels, there was high vertical resolution in the model. Therefore, using the MYJ PBL scheme (which uses only local mixing) should adequately resolve non-local boundary layer turbulence. An additional consideration was that non-local PBL schemes (like YSU) have been found to overpredict CAPE more than local PBL schemes (like MYJ) (Cohen et al. 2015). Tornadic NCFRs in the British Isles typically occur in low-CAPE, high-shear environments (e.g., Smart and Browning 2009) so an gross overestimation of CAPE could yield unrealistic simulations.

Overall, there were few, subtle differences between the YSU and MYJ models. This is likely because the PBL changes more over a full diurnal cycle than over a couple hours, as presented here. However the different schemes had different solutions to daytime PBL mixing, which produced the subtle changes here. The YSU temperature and relative humidity were more similar to the observed, however that resulted in an NCFR with more bulges in radar

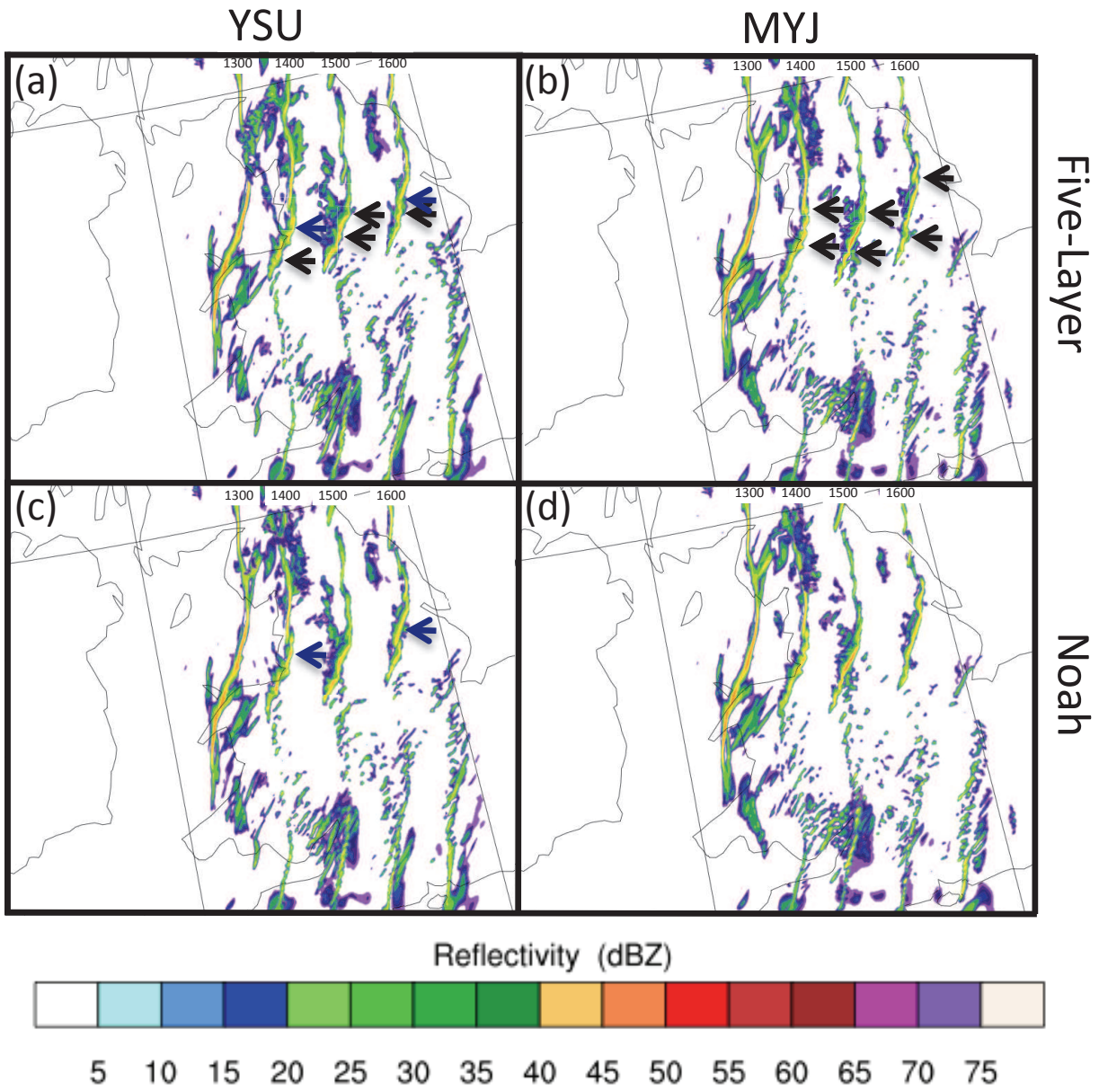

FIG. 9. Changes in model-simulated radar reflectivity due to different PBL and land-surface schemes for simulations valid at 1300, 1400, 1500, and 1600 UTC 29 November 2011. For (a) and (c), the Yonsei University PBL scheme was used. For (b) and (d), the Mellor-Yamada-Janjic PBL scheme was used. (a) and (b) used the Five-Layer Thermal Diffusion land-surface scheme. (c) and (d) used the Noah Land-Surface land-surface scheme. All panels were initialized 1200 UTC 29 November and used Thompson et al. microphysics and 2-way nesting. See text for more information on the arrows and circles.

reflectivity than the observed. Although the MYJ simulation had cooler temperatures and higher relative humidity ahead of the front, the shape of the NCFR in the radar reflectivity had fewer gaps and bulges and simulated broken-S patterns, more similar to the observed radar reflectivity.

5. Microphysics

Microphysics schemes model precipitation, water vapor, and cloud processes (Skamarock et al. 2008) and therefore affect the resulting shape and structure of the NCFR and any leading or trailing stratiform precipitation. Addi-

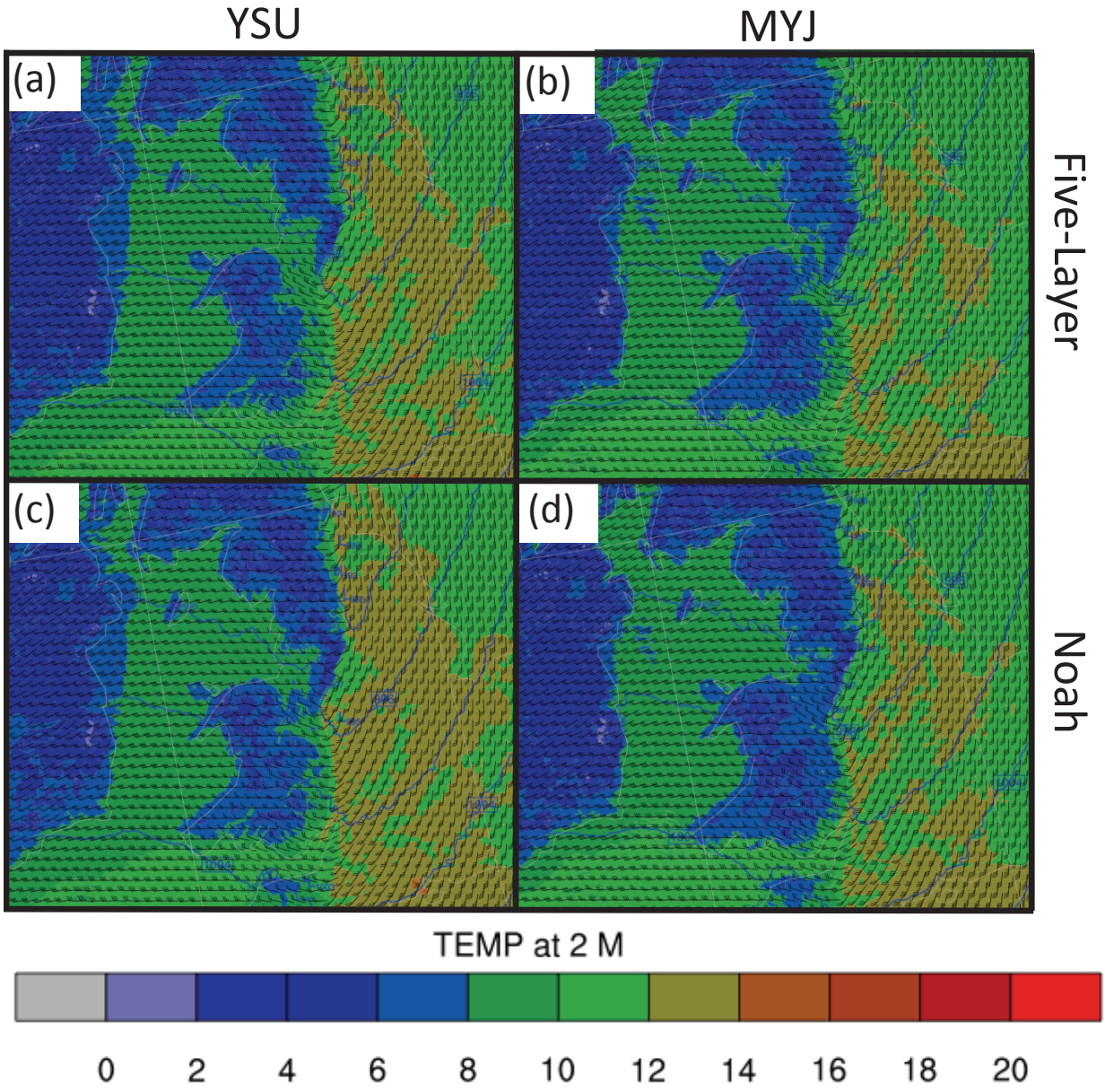

FIG. 10. Same as Fig. 9, but showing temperature at 2 meters above ground level in °C. Wind speed (knots) and direction at 10m above ground level are shown as the black wind barbs. All parameters are valid at 1500 UTC.

tionally, the microphysics scheme, which determines latent heating due to evaporation, can affect the dynamics of the NCFR. For example, the downdraft may be enhanced by hydrometeor melting (e.g., Rutledge et al. 1988). Additionally, the microphysics scheme can affect the strength of the cold pool, which then affects the organization and longevity of the NCFR (Morrison et al. 2015b). Modeled radar reflectivity is based upon the size of hydrometeors modeled, and therefore resulting radar reflectivity relies heavily on the microphysics scheme.

Three microphysics schemes were tested: the WRF Single-Moment 6-class (WSM6), Morrison 2-moment (Morrison), and Thompson et al. (Thompson). The main differences between the schemes are number of precipitation classes and whether they are single- or double-moment. WSM6 has six classes (Hong and Lim 2006) whereas Morrison (Morrison et al. 2009) and Thompson (Thompson et al. 2008) have five classes of liquid and ice particles. Mor-

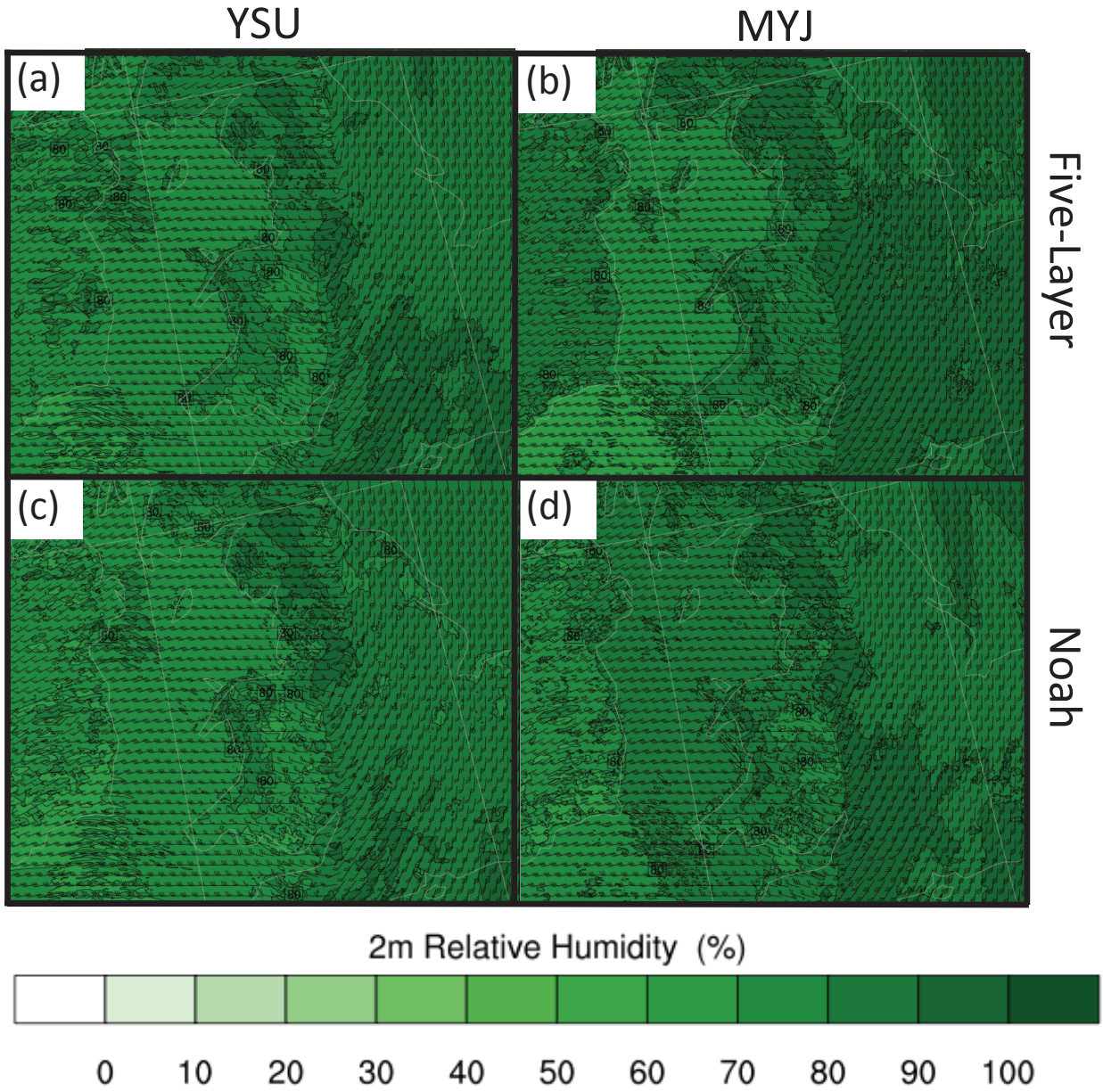

FIG. 11. Same as Fig. 9, but showing relative humidity at 2 meters above ground level. Wind speed (knots) and direction at 10m above ground level are shown as the black wind barbs. All parameters are valid at 1500 UTC.

rison is double-moment, which includes number concentration in addition to mixing ratios for all liquid and ice classes, whereas WSM6 and Thompson are single-moment (only predicting mixing ratio), except for a double-moment cloud-ice variable in Thompson. All three microphysics schemes allow for mixed-phase processes, where interaction between ice and water particles, such as riming, are allowed. The microphysics simulations shown here were all initialized at 1200 UTC 29 November and used the MYJ PBL scheme because these parameters were determined to produce more successful simulations in Sections 3 and 4, respectively.

All three microphysics simulations produced an NCFR in northern England with broken linear convection in the south of England (Fig. 12a, b, and c, land-surface physics are discussed in Section 6), similar to observed reflectivity (Fig. 2). The NCFRs were maintained from 1300 to 1600 UTC. They all had bulges in the NCFR and

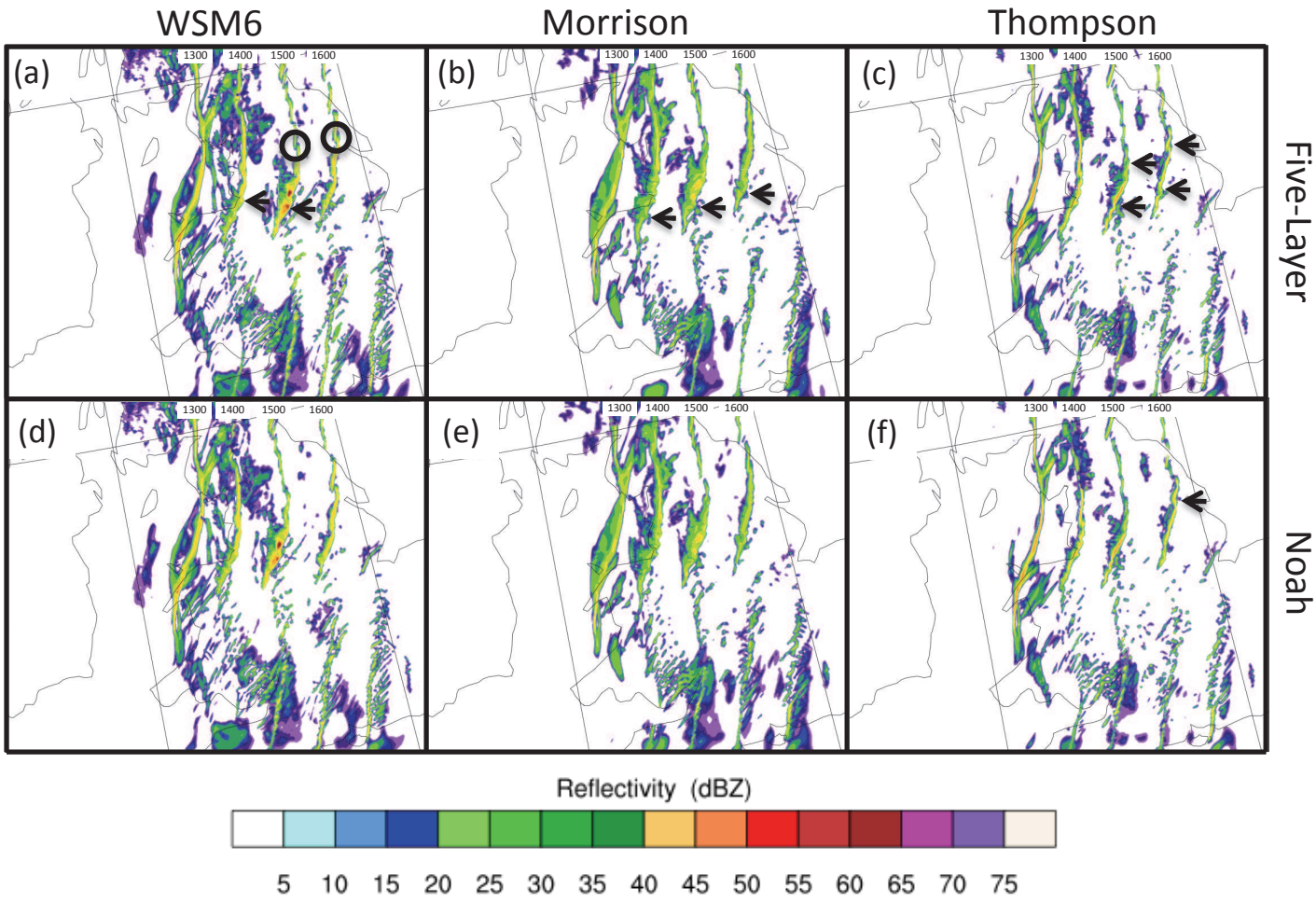

FIG. 12. Changes in model-simulated radar reflectivity due to different microphysics and land-surface physics schemes for simulations valid at 1300, 1400, 1500, and 1600 UTC 29 November 2011. Microphysics schemes used were (a) and (d) WRF Single-Moment 6-class scheme, (b) and (e) Morrison 2-moment scheme, and (c) and (f) Thompson et al. scheme. Land-surface physics schemes were (a), (b), and (c) Five-Layer Thermal Diffusion and (d), (e), and (f) Noah Land-Surface. All panels were initialized 1200 UTC 29 November and used MYJ PBL schemes and 2-way nesting. See text for more information on the arrows and circles.

gaps in the heavy precipitation (Fig. 2). All three simulations failed to produce the broken linear convection directly south of the NCFR (Fig. 12). The differences between the three microphysics simulations were the width and shape of the NCFR, intensity of precipitation, and the extent of the stratiform precipitation. The temperature, relative humidity, sea-level pressure, wind speed, and wind direction had only subtle differences between the microphysics schemes (Figs. 13 and 14).

At 1300 UTC, the NCFR in the WSM6 simulation extended farther north than the observed reflectivity (Fig. 12a compared to Fig. 2). As the simulation progressed, bulges and gaps in the precipitation formed at 1400 and 1500 UTC (examples shown by arrows in Fig. 12a). At 1500 UTC, a maximum in radar reflectivity of up to 65 dBZ formed, but disappeared at 1600 UTC. By 1600 UTC, there were few gaps in the reflectivity and the bulges became less defined. At 1500 and 1600 UTC, a broken S signature formed north of the NCFR (circled in Fig. 12a), similar to the observed reflectivity (Fig. 2). However, the WSM6 NCFR was much wider than the observed NCFR at 1500 UTC. Additionally, there were more bulges and gaps in the WSM6 NCFR at 1500 and 1600 UTC (Fig. 12a) than the observed NCFR (Fig. 2). Stratiform precipitation east and west of the front was present in the WSM6 simulation (Fig. 12a), but the stratiform precipitation was

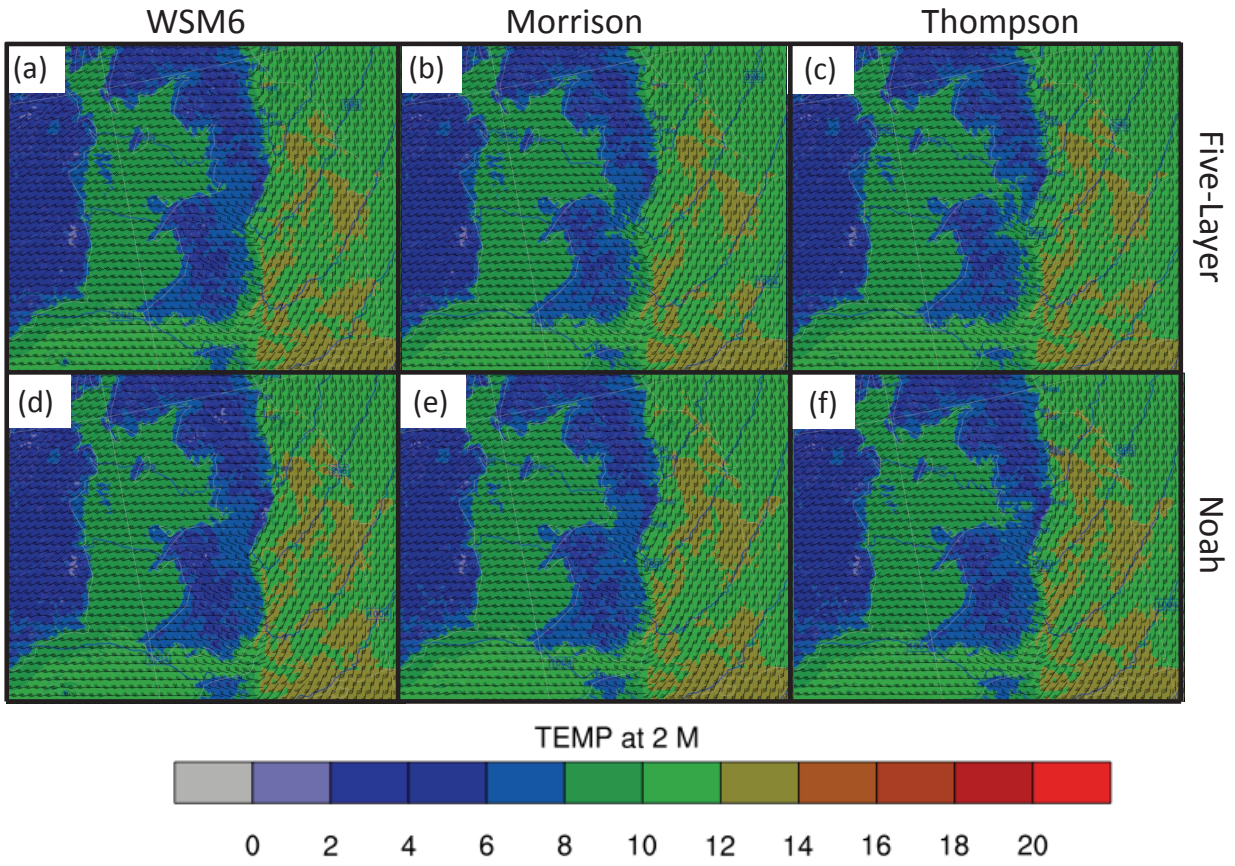

FIG. 13. Same as Fig. 12, but showing temperature at 2 meters above ground level in °C. Wind speed (knots) and direction at 10m above ground level are shown as the black wind barbs. All parameters are valid at 1500 UTC.

not as widespread as the observed reflectivity.

The NCFR in the Morrison simulation was wider than the observed NCFR at all time steps (Fig. 12b compared to Fig. 2). There were not as many bulges in the Morrison simulation as the WSM6 simulation (Fig. 12b compared to a), but the Morrison simulation developed many gaps in the highest radar reflectivity, especially at 1400 and 1500 UTC (Fig. 12b). There was a broken S pattern on the south end of the NCFR at 1400, 1500, and 1600 UTC, similar to observed reflectivity (shown by arrows in Fig. 12b). The maximum reflectivity in the Morrison simulation was 50 dBZ (Fig. 12b), less than the maximum reflectivity in the observed reflectivity (Fig. 2). Additionally, the maximum reflectivity was less extensive in the Morrison simulation than the observed reflectivity (Fig. 12b compared to Fig. 2). The Morrison simulation did, however, have more stratiform precipitation behind the NCFR (green shading in Fig. 12b) than the other two microphysics schemes (Fig. 12a and c).

The Thompson simulation (Fig. 12c) produced an NCFR that was thinner than those in the WSM6 and Morrison simulations (Fig. 12a and b, respectively). At 1500 and 1600 UTC, the Thompson NCFR did not extend as far to the northeast or southwest as the WSM6, Morrison, or observed reflectivity (Fig. 12c compared to Fig. 12a, b and Fig. 2). The Thompson simulation had many bulges at 1400 UTC, which smoothed into a straight NCFR by 1500 and 1600 UTC (Fig. 12c). Because the NCFR in the Thompson simulation was thinner than the WSM6 and Morrison simulations, the bulges appeared more prominent. There were fewer gaps between the regions of heaviest precipitation in the Thompson simulation than in the observed reflectivity at 1500 and 1600 UTC (Fig. 12 compared to Fig. 2). The broken-S pattern on the northern and southern side of the NCFR in observed reflectivity (Fig. 2) were present in the Thompson simulation at 1500 and 1600 UTC (shown by arrows in Fig. 12c). Over the four time periods, the Thompson simulation, compared to the other microphysics schemes, had the strongest reflectivity (up to 55 dBZ) for the largest extent (Fig. 12c), similar to the observed reflectivity (Fig. 2).

Cross sections in the east-west direction of radar re-

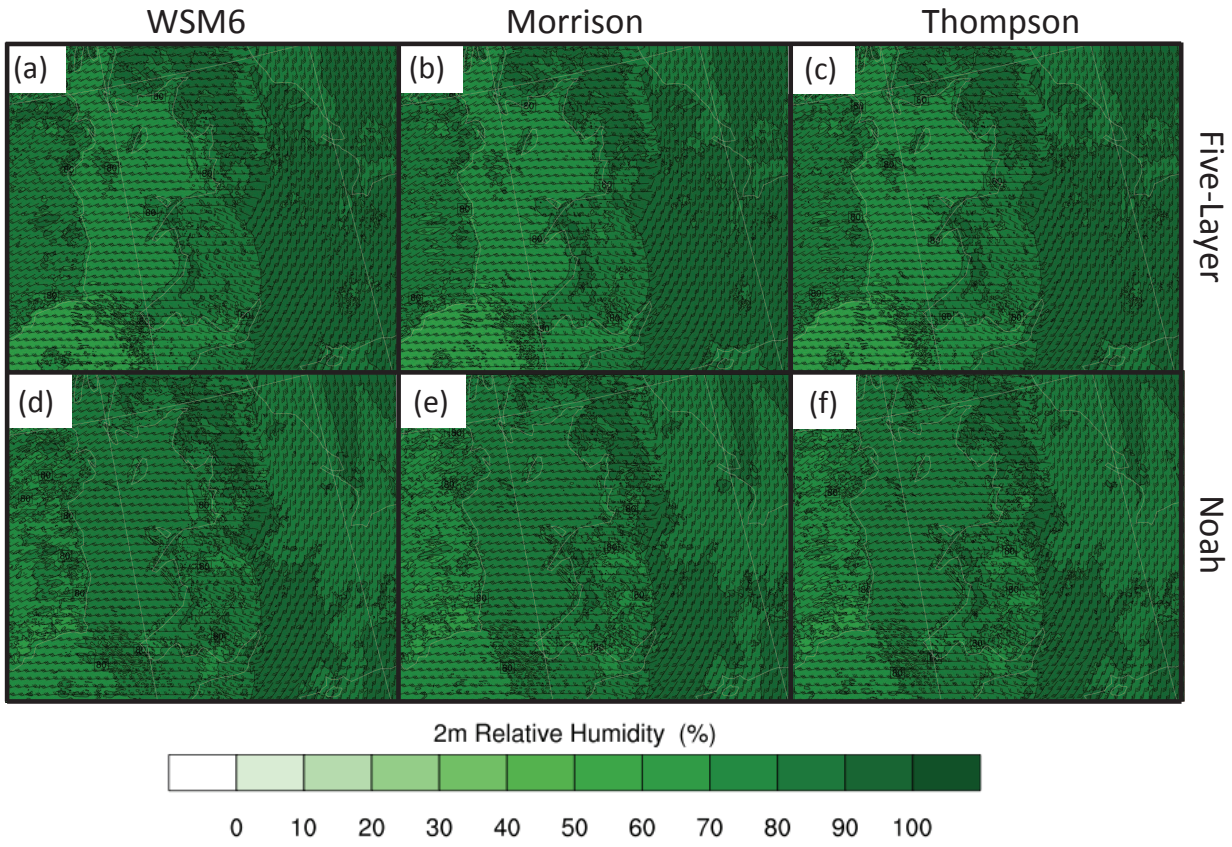

FIG. 14. Same as Fig. 12, but showing relative humidity at 2 meters above ground level. Wind speed (knots) and direction at 10m above ground level are shown as the black wind barbs. All parameters are valid at 1500 UTC.

flectivity were created for the three microphysics schemes to verify there were no unrealistic features in the vertical direction. For comparison, the conceptual model of a mature quasi-linear convective system (of which NCFRs are a subtype) is presented in Fig. 15 (Houze et al. 1989). An observed radar reflectivity cross section of the NCFR was not available for this case. Focusing only on the radar reflectivity (unshaded with the bold outline, and shaded contours, darker indicating higher reflectivity), the heaviest precipitation occurs along the front with high reflectivity occurring at the surface (annotated as a mature cell in Fig. 15). Ahead of the mature cell, a new cell is shown as high reflectivity aloft. Behind the mature cell, an old cell can be seen as high reflectivity from the surface, but not extending as high as the mature cell. As the quasi-linear convective system propagates, new cells develop into mature cells, which turn into old cells. These cells are considered the convective precipitation. None of the microphysics scheme parameterization tests showed the new cell, mature cell, old cell structure as presented by Houze et al. (1989) (Fig. 16). In the conceptual model, regions of lower reflectivity (lower reflectivity extends to the bold line in Fig. 15, which is annotated as the radar echo boundary) and a region of heavy stratiform rain aloft behind the cells (shaded region aloft behind the old cell in Fig. 15) are located behind the new, mature, and old cells. The heavy stratiform rain is caused by the melting of ice particles (trajectories of the ice particles shown in the dashed lines in Fig. 15).

The WSM6 scheme produced a wide region of high reflectivity values, locally up to 65 dBZ, which extended to the surface (Fig. 16a). The region of high reflectivity in the WSM6 cross section was much wider than shown in the conceptual model (Fig. 15). There was more convective precipitation than stratiform, unlike the conceptual model (Fig. 16a compared to Fig. 15).

The Morrison scheme again produced a convective region wider than proposed by Houze et al. (1989) (Fig. 16b compared to Fig. 15). The convective region of the Morrison simulation was also shorter than the other microphysics schemes, only extending to approximately 2 kilometers above sea level (Fig. 16b). The heaviest precipita-

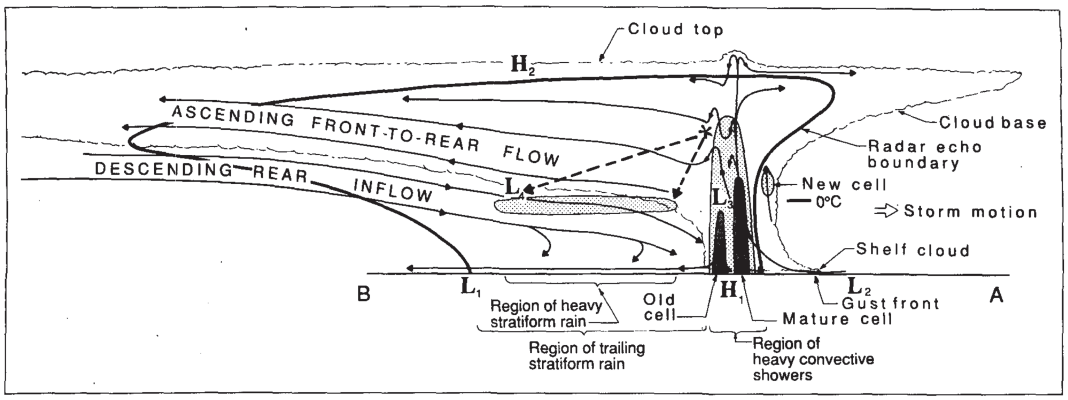

FIG. 15. Conceptual model of a quasi-linear convective system with trailing stratiform precipitation from Houze et al. (1989). The cloud is outlined in thin black lines. The dark bold outline shows weaker reflectivity. Darker shaded contours show regions of higher radar reflectivity.

tion (up to 50 dBZ) did not extend to the surface. There was a region of heavy trailing stratiform precipitation in the Morrison simulation, which was not produced by any other microphysics scheme.

The Thompson scheme produced the skinniest convective region of the three microphysics schemes (Fig. 16c), similar to the findings of (Morrison et al. 2015a). The heaviest convective precipitation, up to 50 dBZ, extended to the surface, unlike the Morrison simulation (Fig. 16c compared to b). The convective region most closely resembled the conceptual model (Fig. 15). However, the stratiform region was relatively weak and not continuous like that in the Morrison simulation (Fig. 16b).

The underestimation of stratiform precipitation has been documented in previous studies of mesoscale convection (e.g., Adams-Selin et al. 2013; Hagos et al. 2014; Morrison et al. 2015a). The stratiform region depends upon smaller hydrometeors being advected by the wind field of the storm (e.g., Parker and Johnson 2004; Luo et al. 2010), in this case the NCFR. Smaller hydrometeors are more likely to evaporate or sublimate, which would make the stratiform region disappear.

Previous studies have opted for two-moment microphysics schemes (like Morrison) over one-moment schemes (like WSM6) because they are more meteorologically robust in simulating the real-world environment (e.g. Bryan and Morrison 2012). However, double-moment schemes are more computationally expensive. In this case, the Morrison and Thompson simulations produced NCFRs more like the observed reflectivity, however the Thompson scheme, although computationally simpler compared to Morrison, produced a narrow, nearly linear NCFR with few gaps and broken-S patterns on the northern and southern section of the NCFR. Therefore, the Thompson microphysics scheme was chosen as the most successful. When comparing the same schemes, Rajeevan et al. (2010) also found that the Thompson scheme more accurately simulated a severe thunderstorm event.

6. Land Surface

The WRF-ARW land-surface scheme affects the land-atmosphere interactions. The land-surface scheme calculates heat and moisture fluxes over land and sea-ice based on radiative and precipitation forcing from the microphysics scheme, and surface variables such as soil moisture, surface temperature, and snow cover. Output from the land-surface scheme is used as the lower-boundary condition for vertical transport in the PBL schemes. Two land-surface schemes were tested here: the Noah Land-Surface Model and Five-Layer Thermal Diffusion. The Noah scheme includes four layers of soil moisture and temperature and also includes snow cover and physics dealing with frozen soil. The Noah scheme also includes vegetation processes such as evapotranspiration. The Five-Layer scheme only includes soil temperatures, as the name suggests, over five layers and does not explicitly model vegetation processes (Skamarock et al. 2008). The land-surface simulations shown were initialized at 1200 UTC 29 November. Because of the interaction between the land-surface scheme and the PBL and microphysics schemes, the changes in radar reflectivity and near-surface temperature, humidity, wind speed, wind direction, and sea-level pressure based on land-surface scheme were compared across PBL and microphysics schemes.

Both the Noah and Five-Layer simulations produced NCFRs in northern England with broken linear convection in southern England (Figs. 9 and 12). Both simulations had nearly the same location and intensity of stratiform precipitation. All of these features were similar to the observed reflectivity (Fig. 2). Differences between the land-

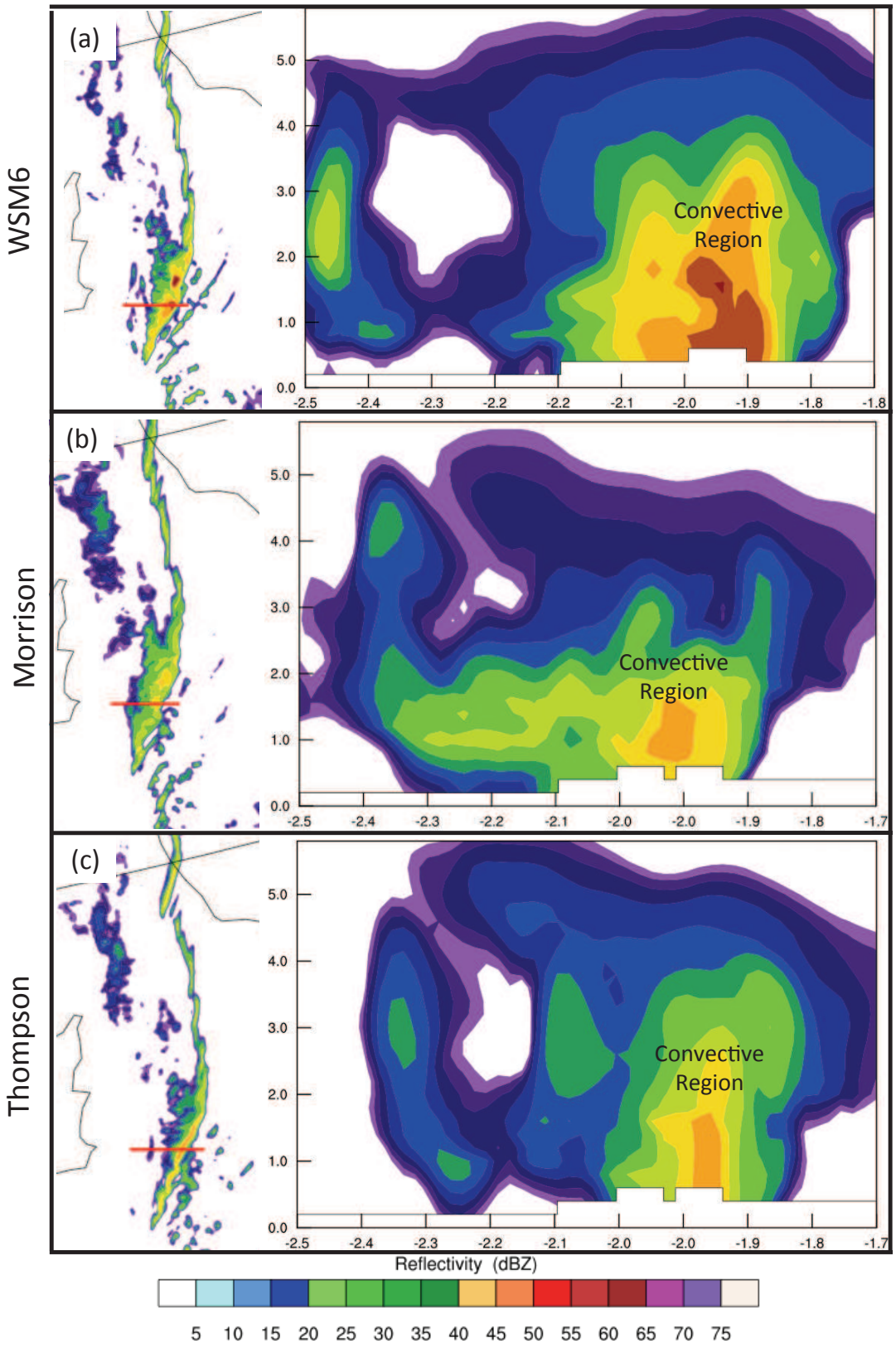

FIG. 16. Cross section showing reflectivity in dBZ of (a) WSM6, (b) Morrison, and (c) Thompson microphysics schemes. All panels were initialized 1200 UTC 29 November and used MYJ PBL schemes and 2-way nesting and are valid at 1500 UTC.

surface schemes were subtle and depended upon the PBL and microphysics schemes.

The differences between the land-surface simulations across PBL schemes were subtle (Fig. 9). In the YSU simulations, the Five-Layer scheme NCFR (Fig. 9a) was less linear than the Noah scheme (Fig. 9c), exhibiting more bulges and more gaps (examples marked in blue arrows), especially after 1300 UTC. This was not the case for the MYJ simulations, where the two land-surface simulations produced NCFRs with similar shapes and similar numbers and locations of bulges and gaps (Fig. 9b and d). The difference in the two land-surface schemes in the MYJ simulations was the magnitude of precipitation. Reflectivity of up to 55 dBZ was more widespread in the Five-Layer land-surface scheme (Fig. 9b), especially at 1300 UTC, more similar to the observed radar reflectivity than the Noah scheme (Fig. 9d). Controlling for PBL schemes, there was little difference in the temperature, relative humidity, sea-level pressure, wind speed, and wind direction between the two land-surface schemes (Figs. 10 and 11). Comparing the PBL and land-surface scheme options, the MYJ, Five-Layer combination was more like the observed reflectivity.

Similarly to the differences across PBL schemes, the differences between the land-surface schemes across microphysics schemes were subtle (Fig. 12). Keeping the microphysics scheme constant, the land-surface schemes produced the same shape of NCFR at all time steps (Fig. 12a and d, compared to b and e, compared to c and f). The only relatively major difference between land-surface schemes was for the Thompson microphysics scheme. At 1600 in the Five-Layer scheme, there was a pronounced broken S pattern on the north side of the NCFR (shown by the arrow in Fig. 12c). In the Noah scheme, there was an S present, but it was not broken (shown by the arrow in Fig. 12f). Besides this, there were few differences in radar reflectivity between land-surface schemes with respect to microphysics scheme.

Keeping microphysics scheme constant, there was little difference in temperature, sea-level pressure, wind direction, and wind speed between the two land-surface schemes (Fig. 13). There was, however, a difference in relative humidity between the land-surface schemes. The Five-Layer scheme had more widespread relative humidity between 90–100% (Fig. 14a, b, and c) compared to the Noah scheme (Fig. 14d, e, and f). The Noah scheme more closely resembled the observed relative humidity (Fig. 3).

Land-surface schemes make a bigger difference in model output over longer simulation periods, for example the 13-month simulation tested by Jin et al. (2010). The effect of the land-surface schemes in this short-term, 6-hour simulation was minimal. Indeed, the two land-surface schemes were very similar in terms of radar reflectivity, temperature, sea-level pressure, wind direction, and wind speeds. Looking at the differences in land-surface scheme for the Thompson microphysics scheme (because the Thompson microphysics scheme was already chosen as more representative), again the Five-Layer scheme was more representative by producing a broken S pattern, even though the relative humidity was higher than observed. Additionally, the Five-Layer scheme was simpler and therefore less computationally expensive. Because the land-surface scheme made little difference to the shape and structure of the NCFR, the simpler of the two was chosen.

7. Summary

This article compared different parameterization schemes for modeling a tornadic narrow cold frontal rainband using WRF-ARW. Analysis detailed the shape and longevity of the storm through radar reflectivity, both in the x–y and x–z directions and near-surface temperature, relative humidity, wind speed, wind direction, and sea-level pressure. As the initialization time approached the time of analysis, the NCFR switched from forming in the southern to the northern domain. Additionally, the simulation initialized at 1200 UTC 29 November 2011 had a long-lived NCFR, similar to the observed reflectivity. The MYJ PBL scheme produced fewer bulges and gaps than the YSU scheme. The WSM6 and Morrison microphysics schemes produced more gaps and thicker NCFRs than the Thompson scheme. Finally, when testing land physics schemes, the Five-Layer scheme produced an NCFR with more widespread higher reflectivity the Noah scheme, however the differences between the schemes were subtle overall.

For the reasons listed above, the parameterization scheme chosen for the case study was initialized 1200 UTC 29 November 2011 using MYJ PBL, Thompson microphysics, Five-Layer Thermal Diffusion land-surface scheme, and 2-way nesting. This combination of parameterization schemes most closely resembled observed radar reflectivity in this case. However, this combination of parameterization schemes is not necessarily representative of all cases in the UK at all times. Therefore, further sensitivity studies are recommended for future cases.

Acknowledgments.

We thank the British Atmospheric Data Centre and the UK Met Office for providing Nimrod system radar data and surface observations. We thank Matt Clark for help with the surface observations. Simulations were performed on the ARCHER UK National Supercomputing Service. Mulder was funded by a scholarship from the Faculty of Engineering and Physical Sciences, University of Manchester.

REFERENCES

Adams-Selin, R. D., S. C. van den Heever, and R. H. Johnson, 2013: Sensitivity of bow-echo simulation to microphysical parameterizations. *Wea. Forecasting*, **28**, 1188–1209.

Bryan, G. H. and H. Morrison, 2012: Sensitivity of a simulated squall line to horizontal resolution and parameterization of microphysics. *Mon. Wea. Rev.*, **140**, 202–225.

Champion, A. J. and K. Hodges, 2014: Importance of resolution and model configuration when downscaling extreme precipitation. *Tellus*, **66 (1–16)**.

Clark, M. R., 2011: Doppler radar observations of mesovortices within a cool-season tornadic squall line over the UK. *Atmos. Res.*, **100**, 749–764.

Clark, M. R. and D. J. Parker, 2014: On the mesoscale structure of surface wind and pressure fields near tornadic and nontornadic cold fronts. *Mon. Wea. Rev.*, **142**, 3560–3585, doi:10.1175/MWR–D–13–00 395.1.

Cohen, A. E., S. M. Cavello, M. C. Coniglio, and H. E. Brooks, 2015: A review of planetary boundary layer parameterization schemes and their sensitivity in simulating Southeastern U.S. cold season severe weather environments. *Wea. Forecasting*, **30**, 591–612, doi:10.1175/WAF–D–14–00 105.1.

Colle, B. A., B. F. Smull, and M. Yang, 2002: Numerical simulations of a landfalling cold front observed during COAST: Rapid evolution and responsible mechanisms. *Mon. Wea. Rev.*, **130**, 1945–1966.

Dean, A. R. and R. S. Schneider, 2008: Forecast challenges at the NWS Storm Prediction Center relating to the frequency of favorable severe storm environments. *Preprints, 24th Conf. on Severe Local Storms, Savannah, GA, Amer. Meteor. Soc.*, [Available online at https://ams.confex.com/ams/pdfpapers/ 141743.pdf.].

Grams, J. S., R. L. Thompson, D. V. Snivley, J. A. Prentice, G. M. Hodges, and L. J. Reames, 2012: A climatology and comparison of parameters for significant tornado events in the United States. *Wea. Forecasting*, **27**, 106–123, doi:10.1175/WAF–D–11–00 008.1.

Hagos, S., Z. Feng, C. D. Burleyson, K.-S. S. Lim, C. N. Long, D. Wu, and G. Thompson, 2014: Evaluation of convective-permitting model simulations of cloud populations associated with the Madden-Julian Oscillation using data collected during the AMIE/DYNAMO field campaign. *Geophys. Res. Atmos.*, **119**, 12,052–12,068, doi:10.1002/2014JD022 143.

Hill, F. F., K. A. Browning, and M. J. Bader, 1981: Radar and raingauge observatoins of orographic rain over south Wales. *Quart. J. Roy. Meteor. Soc.*, **107**, 643–670.

Hong, S.-Y. and J.-O. J. Lim, 2006: The WRF single-moment 6-class microphysics scheme (WSM6). *J. Korean Meteor. Soc.*, **42**, 129–151.

Hong, S. Y., Y. Noh, and J. Dudhia, 2006: A new vertical diffusion package with an explicit treatment of entrainment processes. *Mon. Wea. Rev.*, **134**, 2318–2341, doi:10.1175/MWR3199.1.

Houze, R. A., S. A. Rutledge, M. I. Biggerstaff, and B. F. Smull, 1989: Interpretation of Doppler weather radar displays of midlatitude mesoscale convective systems. *Bulletin of the American Meteorological Society*, **70 (6)**, 608–619.

Janjić, Z. I., 1994: The step-mountain Eta coordinate model: Further developments of the convection, viscous sublayer, and turbulence closure schemes. *Mon. Wea. Rev.*, **122**, 927–945, doi:10.1175/1520–0493(1994)122<0927:TSMECM>2.0.CO;2.

Jin, J., N. L. Miller, and N. Schlegel, 2010: Sensitivity study of four land surface schemes in the WRF Model. *Advances in Met.*, **2010**, 1–11, doi:10.1155/2010/167 436.

Jones, R., 2013: The effect of a coastline and orography on the mesoscale and misoscale dynamics of a cold front. M.S. thesis, University of Leeds.

Jorgensen, D. P., Z. Pu, P. O. G. Persson, and W. K. Tao, 2003: Variations associated with cores and gaps of a Pacific narrow cold frontal rainband. *Mon. Wea. Rev.*, **131**, 2705–2729, doi:10.1175/1520–0493(2003)131<2705:VAWCAG>2.0.CO;2.

Kain, J. S., 2004: The Kain-Fritsch convective parameterization: An update. *J. Applied Met.*, **43**, 170–181, doi:10.1175/1520–0450(2004)043<0170:TKCPAU>2.0.CO;2.

Kawashima, M., 2011: Numerical study of horizontal shear instability waves along narrow cold frontal rainbands. *J. Atmos. Sci.*, **68**, 878–903, doi:10.1175/2010JAS3599.1.

Luo, Y., Y. Wang, H. Wang, Y. Zheng, and H. Morrison, 2010: Modeling convective-stratiform precipitation processes on a Mei-Yu front with the Weather Research and Forecasting model: Comparison with observations and sensitivity to cloud microphysics parameterizations. *J. Geophys. Res.*, **115**, D18 117, doi:10.1029/2010JD013 873.

McAvoy, B. P., W. A. Jones, and P. D. Moore, 2000: Investigation of an unusual storm structure associated with weak to occasionally strong tornadoes over the eastern United States. *Preprints, 20th Severe Local Storms Conference, Orlando, FL*, Amer. Meteor. Soc., 182–185.

Morrison, H., J. A. Milbrandt, G. H. Bryan, K. Ikeda, S. A. Tessendorf, and G. Thompson, 2015a: Parameterization of cloud microphysics based on the prediction of bulk ice particle properties. Part II: Case study comparisons with observations and other schemes. *J. Atmos. Sci.*, **72**, 312–339.

Morrison, H., A. Morales, and C. Villanueva-Birriel, 2015b: Concurrent sensitivities of an idealized deep convective storm to parameterization of microphysics, horizontal grid resolution, and environmental static stability. *Mon. Wea. Rev.*, **143**, 2082–2104.

Morrison, H., G. Thompson, and V. Tatarskii, 2009: Impact of cloud microphysics on the development of trailing stratiform precipitation in a simulated squall line: Comparison of one- and two-moment schemes. *Mon. Wea. Rev.*, **137**, 991–1007, doi:10.1175/2008MWR2556.1.

Mulder, K. J. and D. M. Schultz, 2015: Climatology, storm morphologies, and environments of tornadoes in the British Isles: 1980–2012. *Mon. Wea. Rev.*, **143**, 2224–2240, doi:10.1175/MWR–D–14–00 299.1.

Norris, J., G. Vaughan, and D. M. Schultz, 2013: Snowbands over the English Channel and Irish Sea during cold-air outbreaks. *Quart. J. Roy. Meteor. Soc.*, **139**, 1747–1761.

Parker, M. D. and R. H. Johnson, 2004: Structures and dynamics of quasi-2D mesoscale convective systems. *Journal of the Atmospheric Sciences*, **61 (5)**, 545–567.

Rajeevan, M., A. Kesarkar, S. B. Thampi, T. N. Rao, B. Radhakrishna, and M. Rajaskhar, 2010: Sensitivity of WRF cloud microphysics to simulations of a severe thunderstorm event over Southeast India. *Ann. Geophys.*, **28**, 603–619.

Rutledge, S. A., R. A. Houze, M. I. Biggerstaff, and T. Matejka, 1988: The Oklahoma-Kansas mesoscale convective system of 10–11 June 1985: Preceipitation structure and single-Doppler radar analysis. *Mon. Wea. Rev.*, **116**, 1409–1430.

Skamarock, W. C., et al., 2008: A description of the Advanced Research WRF Version 3. Tech. Note TN–475+STR, 113 pp., NCAR.

Smart, D. J. and K. A. Browning, 2009: Morphology and evolution of cold-frontal misocyclones. *Quart. J. Roy. Meteor. Soc.*, **135**, 381–393, doi: 10.1002/qj.399.

Thompson, G., P. R. Field, R. M. Rasmussen, and W. D. Hall, 2008: Explicit forecasts of winter precipitation using an improved bulk microphysics scheme. Part II: Implementation of a new snow parameterization. *Mon. Wea. Rev.*, **136**, 5095–5115, doi:10.1175/2008MWR2387.1.

Trapp, R. J., S. A. Tessendorf, E. S. Godfrey, and H. E. Brooks, 2005: Tornadoes from squall lines and bow echoes. Part I: Climatological distribution. *Wea. Forecasting*, **20**, 23–34, doi:10.1175/WAF–835.1.

Trapp, R. J. and M. L. Weisman, 2003: Low-level mesovortices within squall lines and bow echoes. Part II: Their genesis and implications. *Mon. Wea. Rev.*, **131**, 2804–2823, doi:10.1175/1520–0493(2003)131<2804:LMWSLA>2.0.CO;2.

[Blank page]

Chapter 4

Paper 3: The case for multiple growth mechanisms of misovortices along a tornadic cold front

[Blank page]

The case for multiple growth mechanisms of misovortices along a tornadic cold front

Kelsey J. Mulder * and David M. Schultz

Centre for Atmospheric Science, School of Earth, Atmospheric and Environmental Sciences, University of Manchester, United Kingdom

ABSTRACT

On 29 November 2011, a narrow cold-frontal rainband (NCFR) traversed Wales and northern England, producing at least seven observed tornadoes. Two tornadoes were associated with a broken S reflectivity pattern, one with a bowing segment, and one with a core and gap radar reflectivity pattern. The remaining three vortices had no apparent reflectivity pattern, likely due to radar resolution. To determine the mechanisms responsible for vortexgenesis and vortex maturity, the NCFR was simulated using WRF-ARW. Five vortices were chosen at maturity (defined as producing strong near-surface horizontal winds). The vortices were associated with wave, hook, bowing segment, core and gap, and broken S radar reflectivity signatures. Vortexgenesis occurred by the roll-up of preexisting vorticity, intensified by stretching. There was, however, tilting present in the wave, hook, bulging, and broken S vortices at genesis. There were two mechanisms responsible for vortex maturity, the first was collocation of stretching and tilting and the intensification of stretching in the vortex, responsible for the wave and core and gap vortices. The second was vortex splitting by strong downdrafts. This occurred for the hook, bulging, and broken S vortices. Results from this study suggest that it is possible for multiple growth mechanisms to be responsible for misovortex intensification along an NCFR.

1. Introduction

Quasi-linear convective systems, including narrow cold-frontal rainbands (NCFRs), were found to be the most common parent storm type for tornadoes and tornado outbreaks in the British Isles (Mulder and Schultz 2015). This is in contrast to the United States during 1998–2000, when only 18% of tornadoes occurred from linear storms compared to 79% from isolated storms (Trapp et al. 2005).

Not only are tornadoes along NCFRs common in the UK, but they also pose a tricky operational forecasting challenge. Misocyclones, or vorticity maxima with diameters between 1–4 km (Fujita 1981) associated with strong winds and tornadoes (e.g., Wakimoto and Wilson 1989; Smart and Browning 2009; Clark and Parker 2014) along NCFRs can be short-lived, appearing and disappearing within tens of minutes. Additionally, it is difficult to predict where along the NCFR vortices are most likely, making forecasting tornadoes and strong straight-line winds difficult. An additional threat of NCFRs is they are capable of producing large-scale tornado outbreaks (Clark 2012; Mulder and Schultz 2015).

Similar to the hook echo being associated with tornadoes in supercells, four radar reflectivity signatures have been associated with damaging straight-line winds and tornadoes along NCFRs: broken S, bow echoes, hooks, and core and gap. The broken S signature begins as a bulge in the NCFR, which evolves into an S-shaped signature. This S shape breaks into two line segments at or shortly after its associated vortex reaches maturity (McAvoy et al. 2000; Clark 2011). Bow echoes occur when a segment of the line accelerates forward, creating a bow shape in the radar reflectivity signature. Tornadic vortices along bowing segments typically occur at or near the apex of the bow (e.g., Funk et al. 1999; Clark 2011). The hook structure resembles a supercell hook echo, with a hook-shaped appendage extending from the NCFR (Carbone 1982; Clark 2011). The core and gap structure occurs when there are segments of the NCFR with heavy precipitation separated by segments (or gaps) of weaker precipitation (e.g., James and Browning 1979; Kawashima 2011).

The core and gap structure has been associated with horizontal shearing instability (HSI, e.g. Kawashima 2011). HSI occurs when a sheet of preexisting vertical vorticity, often formed by the wind shift across a boundary such as a cold front, breaks down into vortices due to perturbations along the line (e.g., Lee and Wilhelmson 1997b). Tornadogenesis occurs when the vortices strengthen due to stretching from conservation of angular momentum (Brady and Szoke 1989; Wakimoto and Wilson 1989; Lee and Wilhelmson 1997b).

The process of vortexgenesis and tornadogenesis associated with HSI differs from supercell tornadogenesis (Markowski and Richardson 2014) and bow echo tornadogenesis (Weisman and Davis 1998; Trapp and Weisman 2003; Atkins

and St. Laurent 2009), which both require tilting in addition to stretching. In supercell tornadogenesis, the mesocyclone forms as horizontal streamwise vorticity is tilted into the vertical. Downdraft air then acquires baroclinic crosswise vorticity, which tilts upwards as it approaches the ground. The resulting vertical vorticity is then stretched to tornado strength by conservation of angular momentum (Markowski and Richardson 2014).

There are three hypotheses about bow echo vortexgenesis. The first hypothesis is that bow echo mesovortices form by downward tilting of baroclinically-induced horizontal crosswise vorticity, creating a cyclonic vortex on the south side of the downdraft and an anticyclonic vortex on the north side of the downdraft (Trapp and Weisman 2003). The second hypothesis is that bow echo vortices form by upward tilting of either baroclinically- (Atkins and St. Laurent 2009) or vertical shear- (Weisman and Davis 1998) induced horizontal vorticity by an updraft. The vorticity couplet formed in this hypothesis has an anticyclonic vortex to the south and a cyclonic vortex to the north of the downdraft, opposite of those in Trapp and Weisman (2003). The third hypothesis is similar to that of supercells: horizontal streamwise vorticity, created by vertical wind shear, is tilted upwards. Then, baroclinically-induced crosswise vorticity is tilted upwards by the updraft. Stretching intensified the vortex (Atkins and St. Laurent 2009).

What mechanism, then, is responsible for vortexgenesis and vortex strengthening when there are multiple reflectivity signatures associated with vortices along the same NCFR? What about when core and gap (associated with HSI), hooks (associated with supercells) and bow echoes occur on the same line? Would vortexgenesis and vortex strengthening occur with the same mechanism or can there be different growth mechanisms along the same NCFR?

To address these questions, we present a case study of a tornadic NCFR in the United Kingdom which exhibited multiple radar reflectivity signatures associated with tornadoes. Section 2 gives details about the case presented herein. Section 3 presents the methods used. Section 4 examines the results of analyzing vortices at genesis and at maturity. These results include cross sections and trajectory analysis. A discussion of the results is given in Section 5. The article ends with a summary of the findings in Section 6.

2. Case Description

On 29 November 2011, an NCFR formed in association with an extratropical cyclone and traversed across Ireland and the United Kingdom. At 0600 UTC 29 November 2011, there were two cold fronts associated with the 985 hPa low: one across the eastern coast of Ireland and the other trailing closely behind (Fig. 1a). Over the next twelve hours, the two fronts merged, the pressure center dropped to 978 hPa (Fig. 1b), and a narrow rainband associated with the fronts formed (not shown). As the cold front passed the Whitworth Observatory in Manchester, winds gusted to nearly 40 mph. Wind direction changed from south before the front to west after the front, quite a substantial wind shift. The temperature decreased from 14°C to 9°C in only a few minutes. Rainfall rates were recorded up to 110 mm (4.33 inches) per hour (Data available at: www.cas.manchester.ac.uk/restools/whitworth/). At 18 UTC 29 November 2011, the front moved past the UK and over the North Sea (Fig. 1c).

Seven tornadoes ranging from T1 to T4 (F0 to F2) were observed along the NCFR (Fig. 2). One tornado (rated T3–4 or F1–2) damaged six caravans in North Wales. Another tornado knocked a chimney to the ground in Greater Manchester, injuring one person. The remainder of the tornadoes damaged buildings, cars, and trees (Brown and Meaden 2012). The media attributed two further instances of damage to tornadoes. However, upon further investigation by the Tornado and Storm Research Organisation (TORRO), the damage could not be differentiated from the widespread straight-line winds associated with the front and therefore were not verified as caused by tornadoes (Brown and Meaden 2012).

The radar reflectivity of the NCFR exhibited broken S patterns (producing Tornadoes 2 and 5), a bulging segment (producing Tornado 6), and core and gap (producing Tornado 7) structures (Fig. 2). There were no apparent reflectivity patterns for Tornadoes 1, 3, and 4, but a small wave (inflection) or hook could have been present, but not visible due to coarse radar resolution. This article will analyze a simulated NCFR with multiple radar reflectivity signatures associated with tornadoes. Vortices along the NCFR associated with a wave, hook, bow echo or bulge, core and gap, and broken S radar reflectivity patterns will be compared at vortexgenesis and vortex maturity to determine their structure and the mechanisms responsible for creating the vortices.

3. Methods

The Advanced Research Weather and Forecasting Model version 3.4.1 (WRF-ARW, Skamarock et al. 2008) was used to model vortexgenesis in the tornadic NCFR on 29 November 2011. The model was initialized using European Centre for Medium-Range Weather Forecasting (ECMWF) analysis data interpolated onto a Lambert conformal grid. The simulation was tested for sensitivity with respect to initialization time, interactive nesting, surface physics scheme, microphysics scheme, and planetary boundary layer scheme. The initialization time and microphysics schemes created the most variations in the model. The simulation setup used the Five-Layer thermal diffusion surface physics scheme, Thompson microphysics scheme (Thompson et al. 2008),

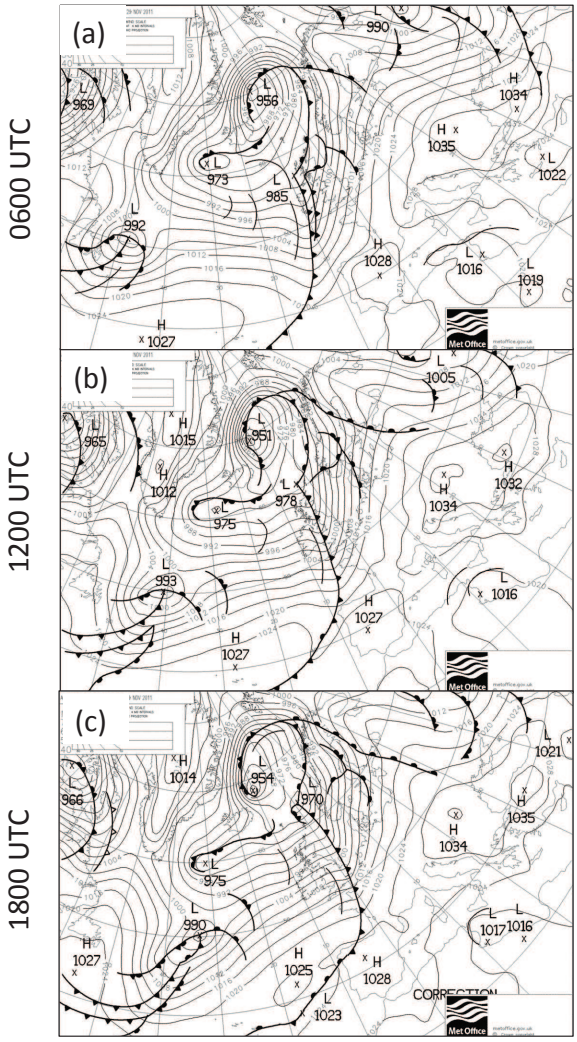

FIG. 1. Surface analysis every six hours on 29 November 2011 from 0600 UTC until 1800 UTC.

Mellor-Yamada-Janjic boundary layer scheme (Janjić 1994), and two-way nesting. This simulation was most similar to surface observations and radar reflectivity.

Four domains, all with 90 vertical levels extending up to 50 hPa, were used to create a high-resolution simulation for the vortices (Fig. 3). The largest domain, D01, had 25-km horizontal grid spacing to capture synoptic scale processes and covered the North Atlantic Ocean, the United Kingdom, and part of Eastern Europe. The Kain–Fritsch cumulus parameterization scheme was used on D01 (Kain 2004), but was turned off in subsequent domains because convection was explicitly resolved. The next largest domain, D02, had 5-km horizontal grid spacing to model the mesoscale. D03, with 1-km horizontal grid spacing was designed both to resolve mesoscale features and as a stepping stone to finer resolution. The smallest domain, D04, had 200-m horizontal grid spacing, sufficient to resolve the vortices. All domains were initialized at 1200 UTC 29 November 2011 and run until 1800 UTC 29 November 2011. Outputs from D04 were saved every 10 seconds for analysis.

At 1300 UTC, the model produced a well-defined NCFR from Northern England through Wales (Fig. 4a), similar to observed reflectivity (Fig. 4b) with wind shifting from the south ahead of the front to the west behind the front (not shown in observed reflectivity). The model at this time poorly resolved the pre- and post-frontal stratiform precipitation. Additionally the modeled NCFR was traveling slower than the observed NCFR (Fig. 4a, b). Two hours later, at 1500 UTC, the modeled NCFR appeared to have the same shape and extent as the observed NCFR in the northern half of the domain (Fig. 4c, d), but again the model did not resolve stratiform precipitation and the

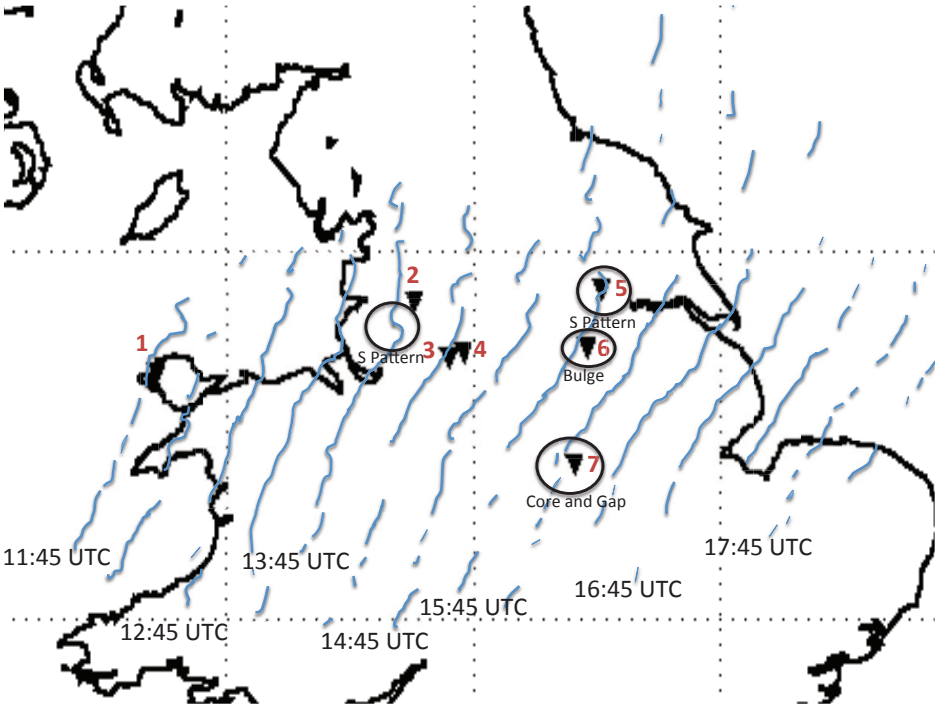

FIG. 2. Map showing the shape and location of the 10–15 mm hr^{-1} rain rate from Nimrod radar 5-minute composite rainfall rates every 30 minutes (solid blue lines) as well as the locations of the tornadoes (inverted black triangles).

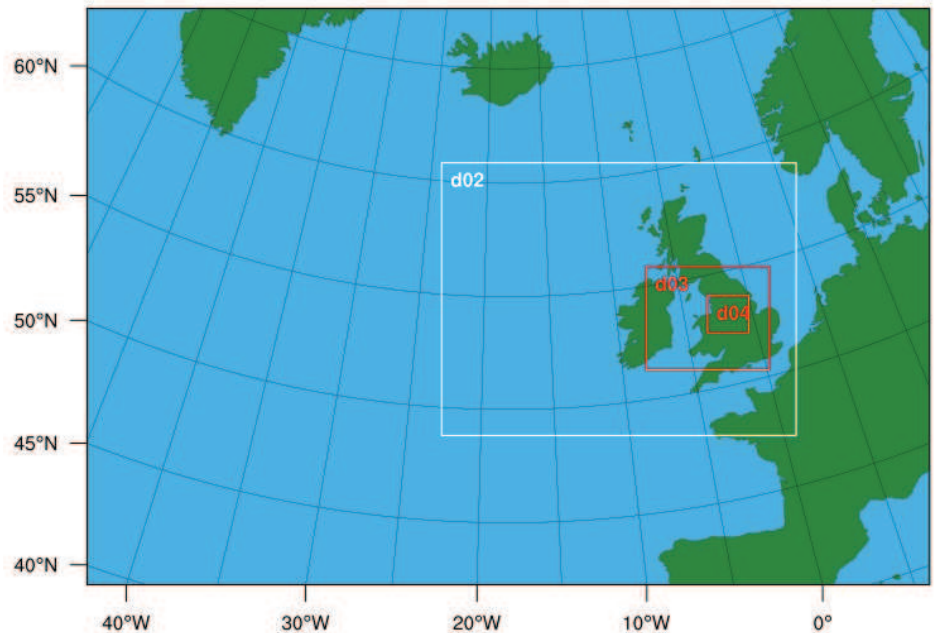

FIG. 3. Map showing the domains used in this analysis. D01 covers the entire map shown. The horizontal resolution of D01, D02, D03, and D04 was 25 km, 5 km, 1 km, and 200 m, respectively.

NCFR was slightly slower and was therefore farther east of the observed reflectivity. In the southern domain, broken linear convection was modeled both south of the NCFR and in a line parallel to and southeast of the NCFR, similar to the observed reflectivity (circled in Fig. 4c, d). Finally, at 1700 UTC, the modeled and observed NCFRs (Fig. 4e and f, respectively) moved over the North Sea. The modeled NCFR had approximately the same shape and extent as the observed NCFR. The observed NCFR at 1700 UTC (Fig. 4f) was aligned more toward the northwest than the model (Fig. 4e). Overall, the model underrepresented stratiform precipitation, but modeled the shape and extent of the NCFR well.

The vortices analyzed herein were chosen by locating relative vorticity (ζ) maxima where $\zeta \geq 10^{-2}$ s^{-1} in regions of radar reflectivity where there was a (1) wave, (2) hook, (3) bulge, (4) core and gap, and (5) broken S radar reflectivity signature (Fig. 5a, b, c, d, and e, respectively). All vortices were between 1–4 km in diameter, classifying them as misovortices (Fujita 1981).

The wave signature was a small inflection point along the NCFR (Fig. 5a at 1610 UTC), which could have been responsible for Tornadoes 1, 3, and 4 from Fig. 2. Throughout the evolution of the wave vortex, there was only a slight inflection in the radar reflectivity, making the vortex hard to detect. The hook, which also could have been responsible for Tornadoes 1, 3, and 4, resembled a hook similar to those associated with supercells (Fig. 5b at 1555 UTC). At genesis, the hook began as a wave with a small vortex (beginning of the green dashed line in Fig. 5b), which grew into a hook (Fig. 5b from 1555 UTC). The bulge differed from the hook because the whole reflectivity was bowed eastward (Fig. 5c at 1530 UTC), rather than the wrapped reflectivity of the hook (Fig. 5b at 1555 UTC). At genesis, however, the bulge began as a hook (beginning of the purple dashed line in Fig. 5c at 1510 UTC). Over the evolution of the vortex, the radar reflectivity pattern bulged outward (Fig. 5c). The core and gap vortex had a region of lighter reflectivity between two heavy cores of precipitation with the vortex located in the gap (Fig. 5d at 1515 UTC). At vortexgenesis for the core and gap vortex, there was no inflection, wave, hook, bulge, or any other signature (beginning of the red dashed line in Fig. 5d at 1435 UTC). The vorticity strengthened at 1455 UTC (Fig. 5d). The gap in the reflectivity formed where the vorticity strengthened (circled in Fig. 5d at 1505–1515 UTC). Finally, the broken S pattern differed from the core and gap in that the northern portion of higher reflectivity was farther west than the southern portion of higher reflectivity, resembling the letter "S" (Fig. 5e at 1540 UTC). At vortexgenesis for the broken S vortex, there was no inflection, wave, hook, or bulge (Fig. 5e at 1430 UTC). As the vortex developed, a bulge developed in the radar reflectivity (circled in Fig. 5e at 1450 UTC). The radar reflectivity deformed around the vorticity maximum, forming the broken S signature (Fig. 5e at 1510–1540 UTC).

These vortices were chosen at the peak of their strength, hereafter referred to as "mature." Vortex maturity was defined as the peak strength of the 10-m AGL horizontal wind. The broken S and gap vortices had 10-m horizontal wind of at least 30 m s^{-1}, the lower threshold for EF0 tornadoes (Glickman 2000). At 200-m grid spacing, we cannot resolve whether or not a tornado was occurring at the ground. Regardless of whether the horizontal winds were caused by tornadic or straight-line winds, the vortex was potentially damaging.

4. Results

Before the NCFR traveled into D04, a vortex sheet formed along the NCFR. This vortex sheet formed inflection points and, over approximately an hour, rolled up into individual vortices (Fig. 6). The progression of the vortex sheet spinning up into individual vortices was indicative of HSI (Lee and Wilhelmson 1997b).

As the NCFR entered D04, many strong vortices, up to 0.05 s^{-1}, were present (Fig. 7). Previous simulations of vortices in different storm types have produced vortices of near this magnitude. For supercells, Adlerman et al. (1999) found vorticity up to 0.054 s^{-1}. For bow echoes, vorticity magnitudes ranged from 0.009 to 0.02 s^{-1} (Trapp and Weisman 2003; Wheatley and Trapp 2008; Atkins and St. Laurent 2009). For NCFRs, Smart and Browning (2009) found vorticity up to 0.04 s^{-1}. The range of vorticity magnitudes certainly depends on the case, but also depends on model grid spacing with higher-resolution models producing higher vorticity values.

The vortex that eventually formed the wave and hook signatures originated at 1530 UTC before it split (Fig. 7). The right side vortex developed into a wave reflectivity signature, strongest at 1610 UTC and the left side vortex developed into a hook signature, strongest at 1555 UTC. The vortex eventually forming the bulging vortex began at 1505 UTC. The vortex merged with a larger vortex before the bulging signature and strongest near-surface horizontal wind speeds occurred at 1530 UTC. The strengthening of vortices due to mergers has been noted previously by Lee and Wilhelmson (1997a,b). The mature vortex associated with the bulging reflectivity signature was located just to the north of the apex of the bulge (Fig. 5c). The vortex associated with the core and gap reflectivity pattern began at 1430 UTC. This vortex also appeared to merge with a vortex directly south of it between 1450 and 1500 UTC. The vortex reached peak near-surface horizontal wind speeds at 1515 UTC. The longest lived of the vortices studied in depth here was the broken S vortex, which began at 1425 UTC and reached peak horizontal wind speeds at 1540 UTC. The vortex continued to propagate 30 minutes longer

before exiting the domain. This vortex did not experience any mergers or splits in its lifecycle.

a. Cross sections

At vortexgenesis, the wave and hook, bulging, and broken S vortices had the same structure (Fig. 8). The area of strongest positive vorticity (filled contours in yellow, orange, and red) was at the eastern edge of the front (high gradient of potential temperature contours, shown in green), collocated with the wind shift line (Fig. 8a, c, g). The vorticity maximum sloped upwards and away from the surface up to 2 km in height toward the west along the isentropes (Fig. 8a, c, g) and up to 2.5 km to the north (Fig. 8b, d, h). The sloping of vertical vorticity to the north was likely due to vorticity advection by the ambient winds from the south ahead of the front. The updraft was collocated with the vorticity maxima with the maximum vertical velocity near 1.5 km (black contours in Fig. 8a, c, g). Negative vertical velocity was located at the surface just to the west (Fig. 8a and c) and north (blue filled contours in Fig. 8b and d) of the vorticity maxima for the wave and hook and bulging vortices, likely associated with the rear inflow jet. The broken S vortex did not have negative vertical velocity at the surface west (Fig. 8g) and north (Fig. 8h) of the vorticity maxima, but the magnitude of positive velocity decreased in those locations. The vorticity maxima were associated with positive stretching for all vortices at vortexgenesis (blue contours in Fig. 8b, d, f, and h). There was positive tilting on the south side of the vorticity maxima for the wave and hook, bulging, and broken S vortices (green contours in Fig. 8b, d, and h).

At vortexgenesis, the core and gap vortex (Fig. 8e, f) was different in structure than the wave and hook, bulging, and broken S vortices. The cyclonic vorticity was concentrated toward the surface and only extended to 1 km in the east–west cross section (filled contours in red, orange, and yellow in Fig. 8e) and up to 2 km in the south–north cross section (Fig. 8f). There were two regions of anticyclonic vorticity: one directly above the vorticity maxima from 1.2–1.8 km (filled blue contours in Fig. 8e and f) and the other aloft and to the west between 2–4 km (Fig. 8e). The cyclonic vorticity maximum was associated with positive vertical velocity and the anticyclonic vortices were associated with negative vertical velocity (solid and dashed black contours, respectively in Fig. 8e, f). There was additional downward motion near the surface west and east of the cyclonic vorticity maximum (Fig. 8e).

The broken S vortex also exhibited anticyclonic vorticity, albeit weak, at the surface directly west of the cyclonic vorticity, perhaps indicating the tilting of streamwise vortex lines upward along the front then downwards behind by weaker or slightly downward vertical winds (Fig. 8g).

At maturity, the wave vortex did not change shape or structure (filled contours in Fig. 9a and b) from vortexgenesis (Fig. 8a and b). Again, there was vorticity up to approximately 2 km with peak vorticity associated with the updraft (black solid contours). Vorticity bent away from the surface to the west (Fig. 9a) and north (Fig. 9b). Maximum vertical velocity was directly above the maximum in vertical vorticity (Fig. 9a). Weak downward motion was located just west of the vorticity maximum (dashed black contours). Weak positive stretching and tilting were collocated the maximum vorticity (blue and green contours, respectively Fig. 9a and b).

The mature hook vortex, on the other hand, changed shape and structure from vortexgenesis. However, the vorticity still sloped upward to the east and slightly to the north (red, orange, and yellow filled contours in Fig. 9c, d). Instead of one vorticity maximum along the front, there were two vorticity maxima: one along the front between 600 m and 1 km and the other farther east at the surface (Fig. 9c). Between the two vorticity maxima, there was a downdraft with maximum downdraft winds from the surface up to approximately 1.5 km (dashed black contours in Fig. 9c). This downdraft was also located to the south of the vorticity maximum (Fig. 9d), where the strong horizontal winds associated with the vortex occurred (Fig. 5b). At genesis, the vorticity maximum was associated with upward vertical velocity. At maturity, the eastern vorticity maximum was collocated with the updraft–downdraft interface with positive stretching and negative tilting within the updraft and negative stretching and positive tilting within the downdraft. The eastern vorticity maximum was associated only with upward motion. The western vorticity maximum had negative stretching (dashed blue contours) and positive tilting (solid green contours) from 400 m to 1 km above and slightly east of the vorticity maximum and positive stretching (solid blue contours) and negative tilting (dashed green contours) aloft and to the west of the vorticity maximum (Fig. 9c). The downdrafts were associated with weak stretching or tilting and therefore were not conducive to vorticity intensification. The mature hook vortex also had a region of weak anticyclonic vorticity at 1–1.8 km, south of the cyclonic vorticity. This anticyclonic vorticity appeared to be indicative of vortex line tilting by a localized updraft (Fig. 9d), similar to Atkins and St. Laurent (2009).

At maturity, the bulging vortex resembled the mature hook vortex with a cyclonic vorticity maximum above the surface along the front at 400 m to 2 km, a secondary vorticity maximum at the surface to the west, and a downdraft between them (Fig. 9e). In addition, there was a strong vorticity maximum, up to 0.06 s^{-1}, aloft from 1–2.5 km between the two low-level vorticity maxima. Both the low-level vorticity to the east along the front and the vorticity maximum aloft were associated with the updraft–downdraft interface (Fig. 9e). The eastern low-level vorticity maximum was associated with positive stretching and

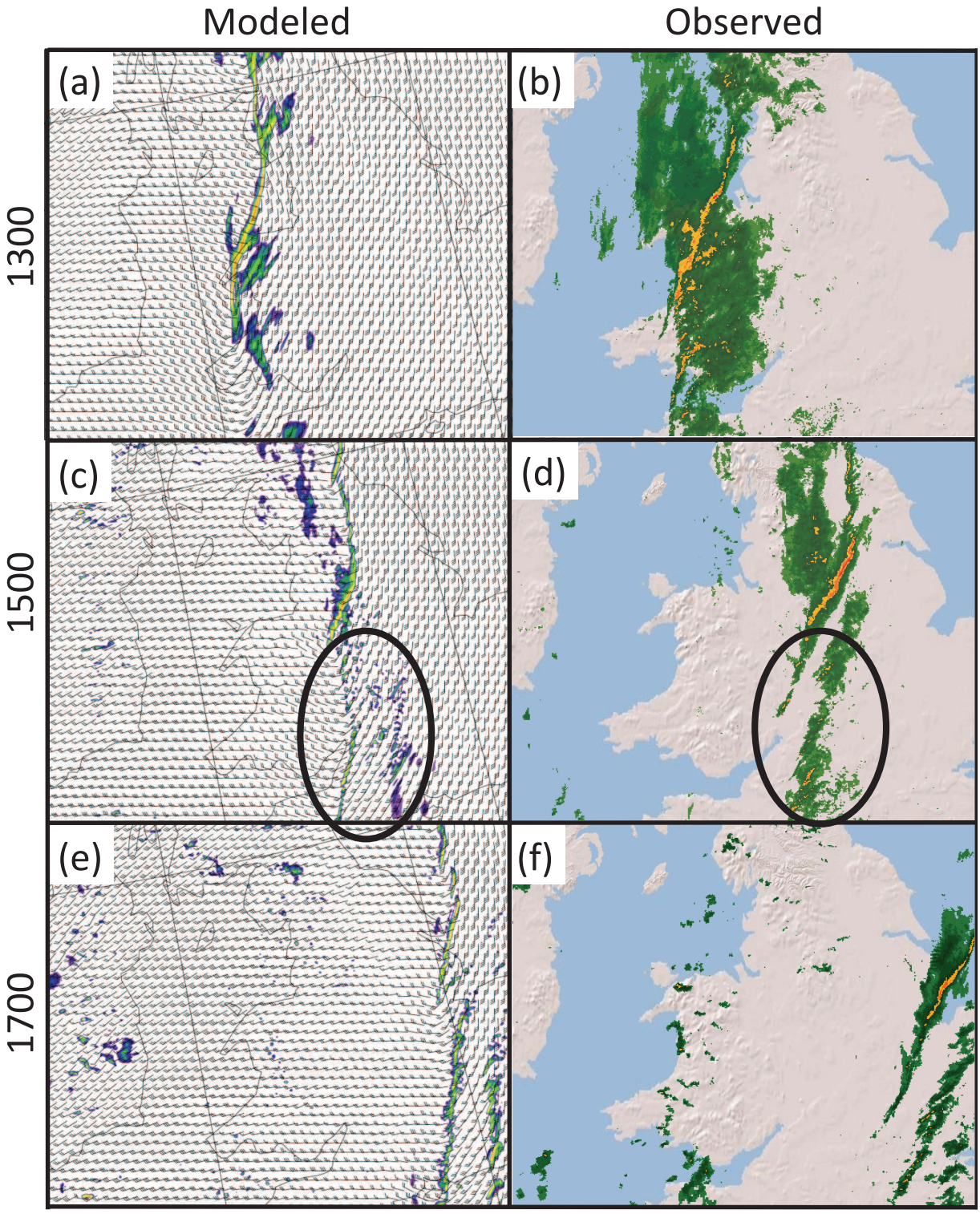

FIG. 4. Comparison between modeled radar reflectivity from D03 (1-km grid spacing) at (a) 1300 UTC, (b) 1500 UTC, and (c) 1700 UTC and observed radar reflectivity at (d) 1300 UTC, (e) 1500 UTC, and (f) 1700 UTC from Nimrod radar 5-minute composite rainfall rates.

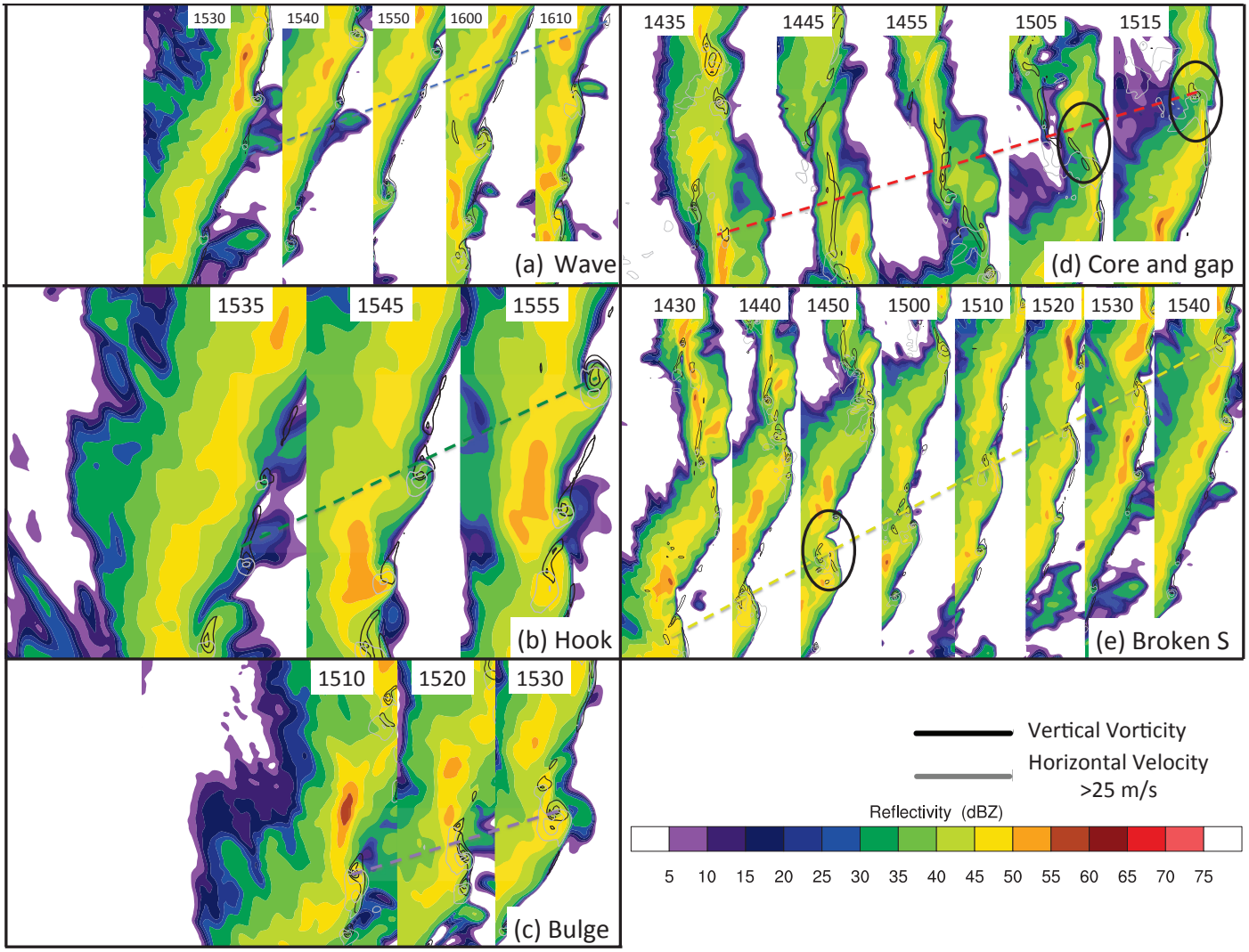

FIG. 5. Modeled radar reflectivity (colored contours) of the vortices chosen for further analysis from D04 (200-m grid spacing) showing evolution over time starting at genesis (far left of each panel) to maturity (far right of each panel). Relative vorticity contoured every 0.01 s^{-1} from 0.02 s^{-1} (black contours) and horizontal velocity at 10 m AGL contoured every 5 m s^{-1} starting at 20 m s^{-1} are shown for (a) wave (1530–1610 UTC), (b) hook (1525–1555 UTC), (c) bulge (1430–1530 UTC), (d) core/gap (1435–1515 UTC), and (e) broken S (1430–1540 UTC) vortices. The approximate location of the vortex over time is shown by the dashed lines.

FIG. 6. Modeled relative vorticity at 500 m (colored contours) from D03 (1-km grid spacing) from 1240 UTC until 1400 UTC at the beginning of the model simulation.

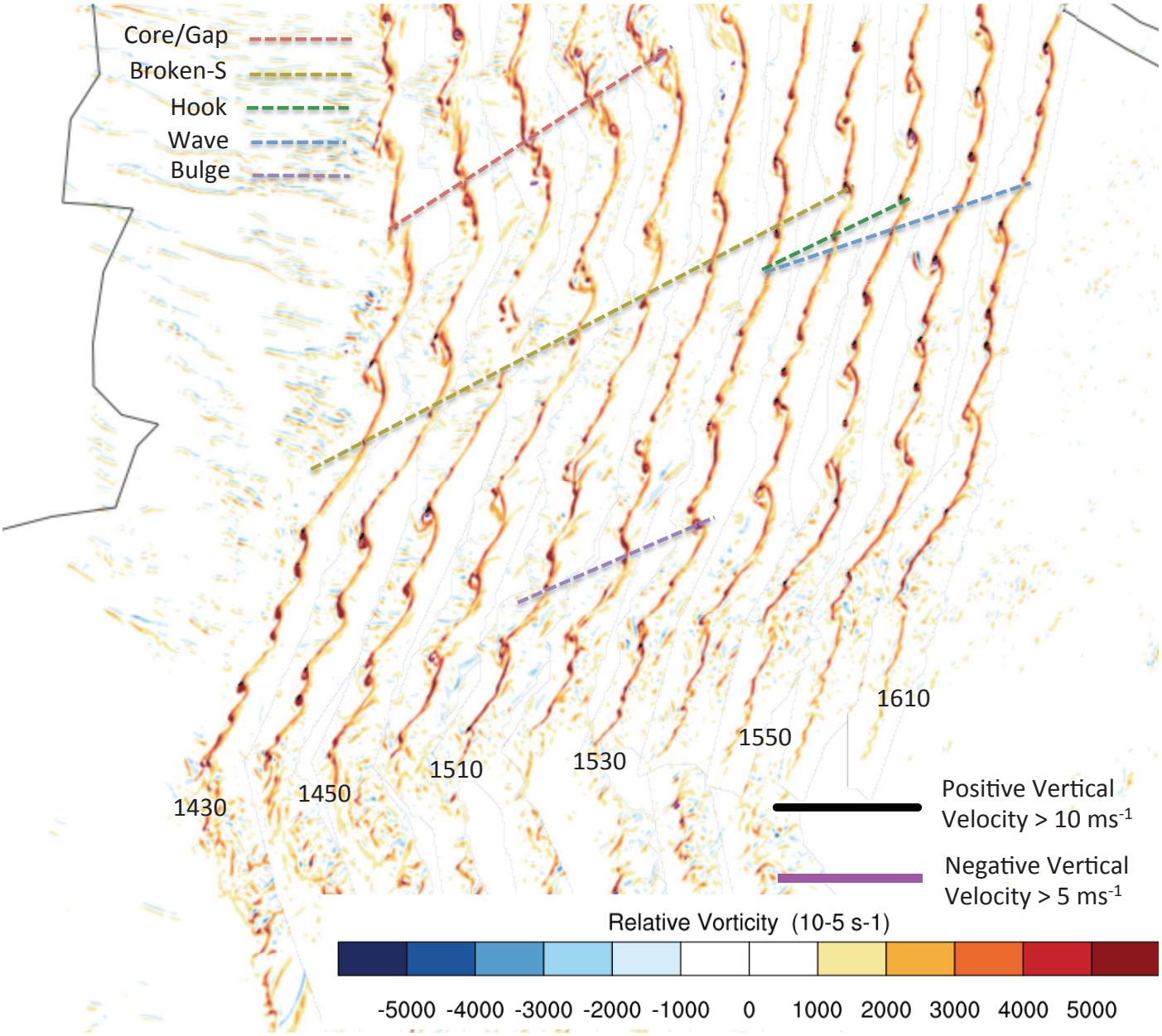

FIG. 7. Modeled relative vorticity at 500 meters (colored contours) from D04 (200-m grid spacing) over time as the NCFR traverses across northern England. Horizontal velocity is shown in black contours at 10 m AGL contoured every 5 m s^{-1} starting at 20 m s^{-1}. Approximate vortex paths are shown in dashed lines for wave (blue), (b) bulge (purple), (c) core/gap (red), (d) hook (green), and (e) broken S (yellow) vortices. The vortices may propagate beyond the dashed vortex paths, but the dashed paths end at the peak of horizontal wind speed at 10m (not shown).

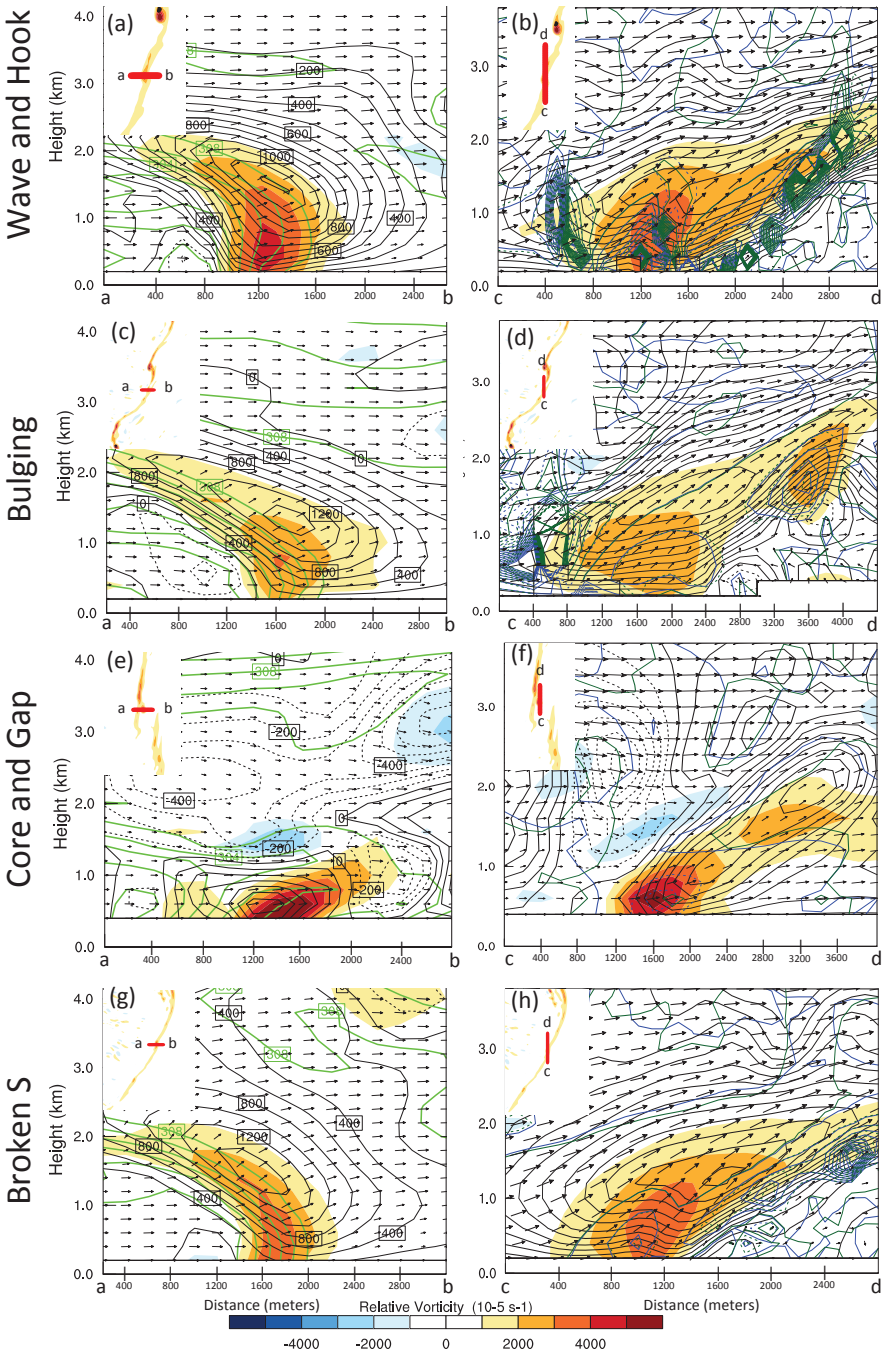

FIG. 8. Cross sections of the vortices at genesis showing relative vorticity (colored contours), positive vertical velocity (solid black contours every 5 cm s^{-1}) and negative vertical velocity (dashed black contours every 5 cm s^{-1}) (a), (c), (e), and (g) east–west cross sections and (b), (d), (f), and (h) south–north cross sections. In the east–west cross sections, equivalent potential temperature is shown in light green contours (every 2 K). For south–north cross sections, tilting is shown in dark green contours (-.1 to .1 by .01 s^{-2}) and stretching in dark blue contours (-.1 to .1 by .01 s^{-2}). Unphysical large values of stretching and tilting were removed, comprising of 3% of all data points. Cross sections are (a) and (b) wave and hook vortex, (c) and (d) bulging vortex, (e) and (f) core and gap vortex, and (g) and (h) broken S vortex. Locations of the cross sections are shown in the insets (red line).

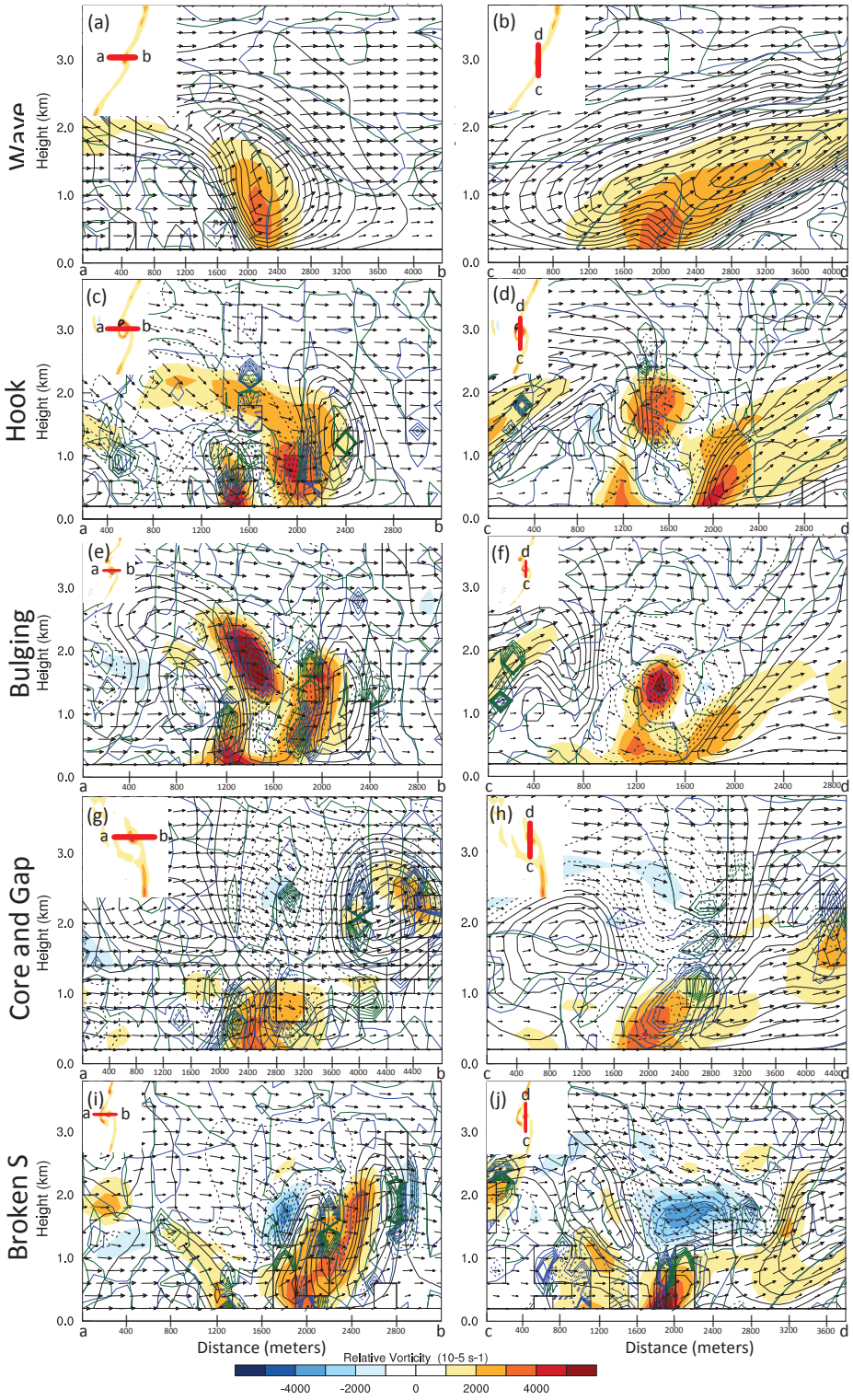

FIG. 9. Cross sections of the vortices at maturity showing relative vorticity (filled colored contours), vertical velocity (black contours every 5 cm s^{-1}, solid for positive values and dashed for negative values), stretching (blue contours, every 0.25 s^{-2}, solid for positive values and dashed for negative values), and tilting (green contours, every 0.25 s^{-2}, solid for positive values and dashed for negative values) for (a), (c), (e), and (g) east–west cross sections and (b), (d), (f), and (h) south–north cross sections. Cross sections are (a) and (b) wave and hook vortex, (c) and (d) bulging vortex, (e) and (f) core and gap vortex, and (g) and (h) broken S vortex. Locations of the cross sections are shown in the insets (red line).

negative tilting on the east side and aloft from 400 m to 2 km and negative stretching and positive tilting on the west side from 400 m to 1 km (Fig. 9e). The vorticity maximum aloft was collocated with positive stretching and negative tilting except for the top from 2–2.5 km where there was positive tilting and negative stretching (Fig. 9e). The surface vorticity maximum to the west was associated with a localized updraft, positive tilting, and zero stretching at the surface and negative stretching up to 1 km (Fig. 9e). Conversely to the hook vortex, there was no region of anticyclonic vorticity in the mature bulging vortex (Fig. 9e, f). The downdraft extended south of the vortex (Fig. 9f), where the strong horizontal winds were located (Fig. 5c).

The mature core and gap vortex had a surface vorticity maximum along an updraft–downdraft interface (Fig. 9g, h). The vorticity maximum was associated with positive stretching and near-zero tilting with positive stretching and negative tilting east of the vortex and negative stretching and positive tilting west of the vortex up to 1 km (Fig. 9g). The vorticity was concentrated below 1 km with weaker vorticity bending aloft to the north (Fig. 9h). There was downward motion to the south of the vorticity maximum, where the strong horizontal winds were located (Fig. 9g).

At maturity, the broken S vortex had two surface vorticity maxima (Fig. 9i), similar to the mature hook and bulging vortices. The western vorticity maximum was stronger, up to 0.6 s^{-1}, and was associated with an updraft, not a updraft–downdraft interface, like the mature hook, bulging, and core and gap vortices. The western vorticity maximum was associated with positive stretching on the west side and positive tilting on the east side of the vortex (Fig. 9i). There was negative vertical velocity south of the vorticity maximum (Fig. 9j), where the strong horizontal winds were located (Fig. 5e). There was a cyclonic and anticyclonic vorticity couplet aloft, between 1–2 km. The cyclonic vortex was associated with an updraft and the anticyclonic was associated with a downdraft (Fig. 9i). The cyclonic vorticity aloft was associated with positive tilting and the anticyclonic vorticity was associated with negative tilting, suggesting tilting of the streamwise vorticity upward to create cyclonic vorticity along the front and downward for anticyclonic vorticity behind the front (Fig. 9i). The secondary surface vorticity maximum of up to 0.3 s^{-1} only extended to approximately 1.5 km and was associated with weak vertical motion, positive stretching to the west of the maximum and positive tilting collocated with the vorticity maximum (Fig. 9i). The secondary vortex also appeared to have weak anticyclonic vorticity to the west at approximately 1 km.

b. Trajectory analysis

To further understand the evolution of vorticity, backward trajectories were calculated every ten seconds for ten minutes, located every 200m within the vortex from 500 meters in height. Backward trajectories were calculated both at vortexgenesis and when the vortex reached maturity. To calculate vorticity tendency along the trajectories, the Lagrangian vorticity equation was used:

$$\frac{\partial \zeta}{\partial t} = \omega_h \cdot \bigtriangledown w + \zeta \frac{\partial w}{\partial z} + k \cdot (-c_p \bigtriangledown \theta_\rho \times \bigtriangledown \pi) + R \quad (1)$$

where ζ is the vertical component of relative vorticity, ω_h is the horizontal component of vorticity, w is the vertical wind, c_p is the specific heat at constant pressure, θ_ρ is the total density potential temperature, π is the nondimensional pressure, and R is the residual. The terms on the right hand side of Equation (1) represent tilting, stretching, baroclinic generation, and the residual, respectively. The turbulent mixing and diffusion terms were not calculated, but were accounted for in the residual term. Although the baroclinic term was calculated along the trajectories, the result was many orders of magnitude too small to make a difference and therefore was not included in the analysis.

There were two main trajectory paths for all vortices: one moving parallel to the NCFR from the south into the NCFR and the other moving from west to east into the vortex (Fig. 10). There were no inflow trajectories from the east side of the front.

There were three types of trajectories. The first type was a descending trajectory. These trajectories descended for the majority of their path before ascending into the vortex (for example, see the black line in Fig. 11c). The second type was an oscillating vortex, which eventually ascended into the vortex. The third type were ascending trajectories, which originated near the ground and ascended through most of their lifetime.

The trajectory representing the wave and hook vortex was an oscillating trajectory (Fig. 11a). At the peak of the parcel's first ascent, vorticity was slightly positive due to tilting, but was negative for the remainder of the trajectory. As the parcel began ascending again, stretching increased, thus increasing the vorticity to approximately 0.004 s^{-1}. This increase in vorticity was due to stretching alone.

The trajectory traveling into the bulging vortex originated to the west of the vortex and was also an oscillating trajectory (Fig. 11b). Tilting was small and positive for most of the first six minutes of the trajectory. After that, tilting became negative. Negative stretching kept vorticity negative until stretching became positive just before the trajectory began ascending into the vortex, thereby increasing the total vorticity to approximately 0.0028 s^{-1}.

The core and gap trajectory originated southwest of the vortex and was a descending trajectory (Fig. 11c). The trajectory began at approximately 470 m, descended to 250 m, and ascended into the vortex. With the final ascent, the vorticity increased to nearly 0.006 s^{-1}, solely by stretching. Tilting was near zero or negative throughout the trajectory and became more negative over time.

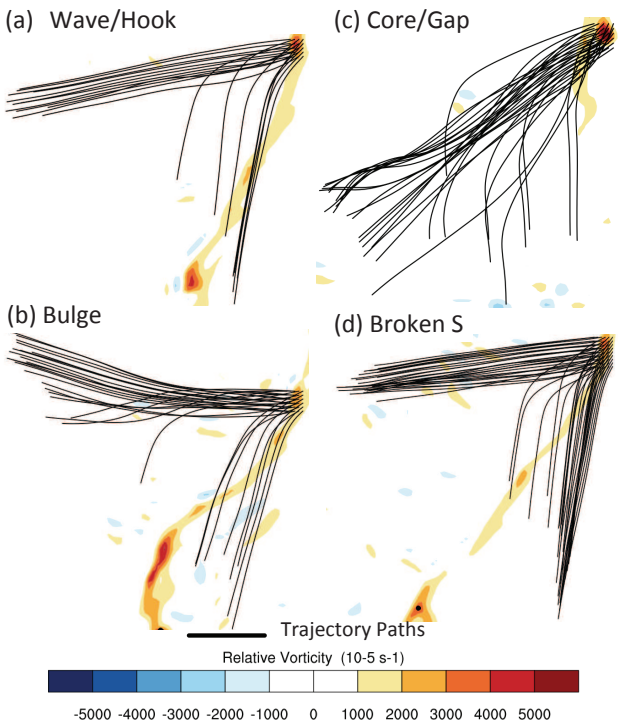

FIG. 10. Paths of backwards trajectories from vortices at vortexgenesis (black lines) overlaid onto relative vorticity (filled contours) for the (a) wave and hook, (b) bulge, (c) core and gap, and (d) broken S vortices.

Two trajectories represented the broken S trajectory; one a descending trajectory originating from west of the vortex (Fig. 11d) and the other an ascending trajectory originating south of the vortex (Fig. 11e). The descending trajectory had negative tilting throughout the trajectory and near-zero or negative stretching until just before the trajectory began its final ascent, when stretching increased the vorticity up to approximately 0.004 s^{-1}. The ascending trajectory remained near the surface until the last three minutes (Fig. 11e). Before its ascent, the vorticity was nearly zero. As the parcel began to ascend, tilting increased. Tilting continued to increase as the trajectory ascended, but stretching increased faster, which strengthened the vorticity to 0.0026 s^{-1}.

Backward trajectories were also calculated for mature vortices. The mature wave vortex trajectory was a descending vortex (Fig. 12a). During the parcel's descent, tilting was small but positive. At the end of the descent, tilting turned negative and grew more negative until the end of the trajectory. As the parcel ascended into the vortex, the vorticity originally created by tilting strengthened due to stretching alone.

The mature hook vortex trajectory shown was also a descending trajectory (Fig. 12b), which ended in the west-side surface vorticity maximum in Fig. 9c. The vorticity was nearly zero for the majority of the descent with any positive vorticity solely due to tilting. However, as the trajectory neared the bottom of its descent, the stretching increased, which increased the vorticity. Tilting became negative as the stretching increased.

The mature bulging vortex trajectory was also descending (Fig. 12c) and also ended in the west-side surface vorticity maximum in Fig. 9e. Near the bottom of the trajectory's descent, the stretching term increased substantially from slightly negative to over 0.003 s^{-1}. There was small positive tilting at the beginning of the parcel's descent and negative tilting over the rest of the trajectory.

A trajectory originating to the southwest of the mature core and gap vortex was also descending (Fig. 12d). The vorticity increase was attributed solely to stretching because tilting remained near zero for the majority of the trajectory. As the trajectory finished its descent, tilting decreased and became more negative in the final three minutes of the trajectory.

The trajectory entering the mature broken S vortex oscillated into the more intense vorticity maximum to the northeast (Fig. 12f). The increase of vorticity was dominated by tilting (Fig. 12f). Tilting increased until the very end when the parcel began ascending and the tilting decreased slightly. Stretching began near zero and became

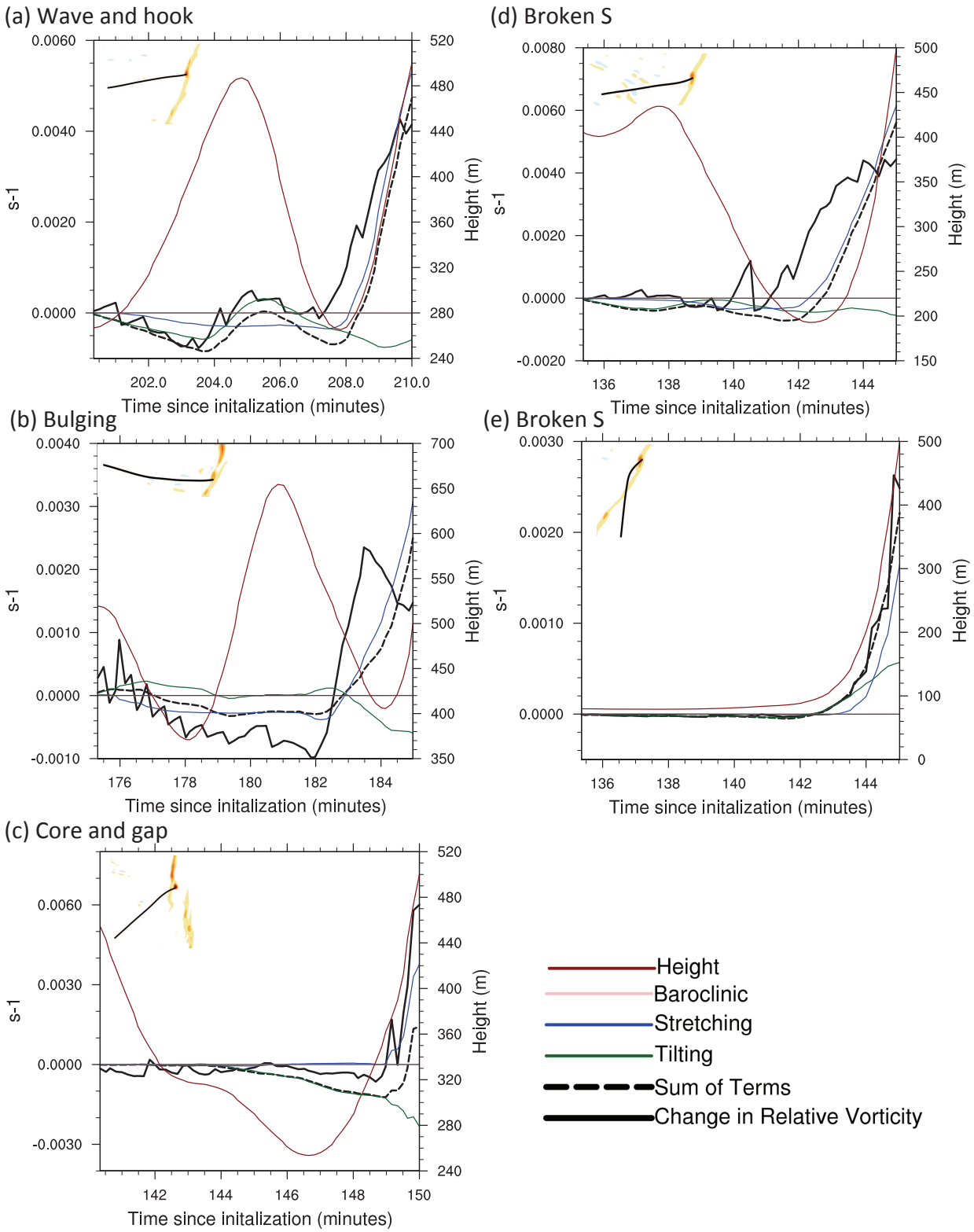

FIG. 11. Plots showing time integrated relative vorticity, stretching, and tilting terms for the wave and hook vortex at genesis. Relative vorticity is shown as the black solid line, stretching in blue, tilting in green, and the sum of stretching, tilting, and baroclinicity as the black dashed line. Relative vorticity and the terms are associated with the left hand axis. Height of the trajectory is the red line corresponding to the right hand axis. The path of the trajectories are shown in the insets. The trajectory plots are for the following vortices: (a) wave and hook, (b) bulging, (c) core and gap, and (d) and (e) broken S.

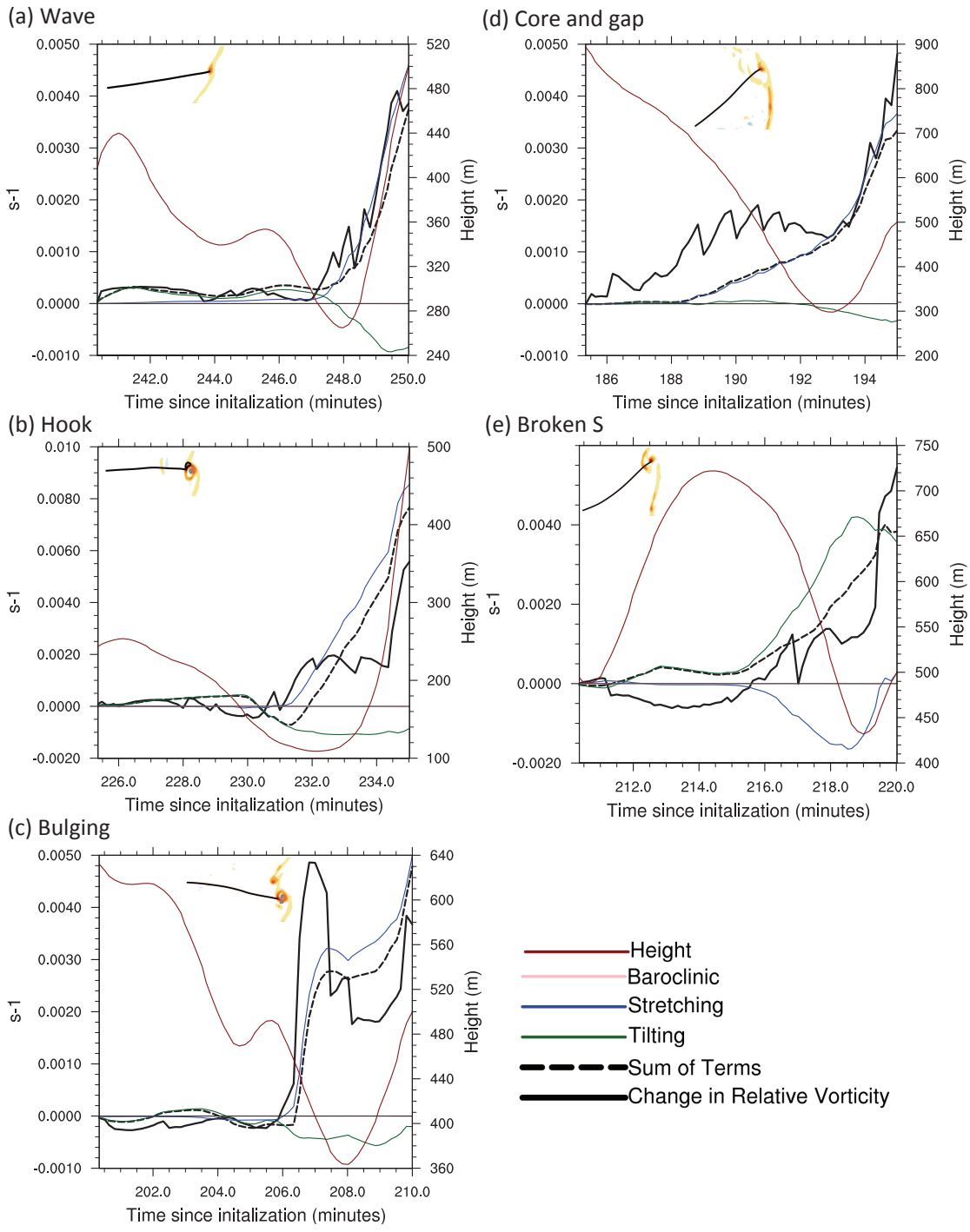

FIG. 12. Same as Fig. 11 but for mature vortices: (a) wave, (b) hook, (c) bulging, (d) core and gap, and (e) broken S.

negative until the final ascent into the vortex, when it became less negative, then slightly positive.

5. Discussion

At vortexgenesis, all of the vortices had similar structures an updraft at the east side the front associated with positive vertical vorticity and, in the case of the wave, hook, bulging, and core and gap vortices, cold air descending in the downdraft behind the front. The broken S vortex had weak upward vertical motion behind the front. Wind was southerly to the east of the front and advected the positive vorticity away from the ground, upwards and to the north. Trajectory analysis showed that the core and gap vortex at vortexgenesis strengthened via stretching alone by the localized updrafts, similar to Lee and Wilhelmson (1997b). On the south side of the wave and hook, bulging, and broken S vortices, there was cyclonic vertical vorticity due to tilting of horizontal vorticity by the southerly wind, verified by the trajectory analysis. Lee and Wilhelmson (1997b) hypothesized that stretching by the updraft was primarily responsible for intensifying vortices from vortexgenesis and that tilting was not substantial. These results verify that stretching was the primary source of intensification of vorticity at vortexgenesis, but that tilting of horizontal vorticity plays a role as well in some vortices, contrary to the hypothesis by Lee and Wilhelmson (1997b).

The wave and core and gap vortices at maturity had the same structure as they did at vortexgenesis. Positive stretching and tilting were separated in space at vortexgenesis for the wave vortex. At maturity, the positive stretching and tilting were collocated. The core and gap vortex also had collocation of stretching and tilting as well as an intensification of stretching at maturity.

The mature hook, bulging, and broken S vortices were broken into two distinct vorticity maxima, an eastern maximum aloft and a western maximum at the surface, separated by a downdraft or a weak updraft. Within the downdraft or weak updraft, there was negative tilting and weak stretching, making the downdraft not conducive to vorticity production. As a result, the vorticity was split into two parts. The hook and bulging vortices had stronger vorticity in the western vortex, where both tilting and stretching were occurring whereas the stronger vorticity in the broken S pattern was in the western vortex, which also had both stretching and tilting. Stretching was the dominant mechanism in the hook and bulging vortices and tilting was the dominant mechanism in the broken S vortex, as determined by the trajectory analysis.

The strength and size of the vorticity maxima made it possible to deform the reflectivity field into its respective shapes. The hook vortex likely formed from wrapping of the hydrometeors around the vortex. The broken S pattern likely formed in a similar way with wrapping of hydrometeors around the vortex. The gap in the broken S reflectivity was associated with the vortex itself which has also been observed in previous literature (Grumm and Glazewski 2004; Smart and Browning 2009). The strong rear inflow jet (Smull and Houze 1987), some of which reached the surface, in the bulging vortex likely pushed the convective line forward, creating the bowing appearance, as proposed by (Fujita 1981). The same mechanism was likely responsible for the appearance of the wave pattern in reflectivity as well. It is possible that the mature hook, bulging, and broken S vortices are part of the same evolution, but at different phases because the reflectivity signatures associated with the vortices studied herein changed morphologies over their lifetime.

Although the vortices had varying structure at maturity, they all had a downdraft south of the vorticity maximum, collocated with the strong horizontal winds near the surface, indicating the advection of higher momentum air to the surface, as suggested by Smart and Browning (2009). The implication for tornadogenesis is an increase in stretching and tilting by the downdraft, therefore increasing vorticity. Additionally, this location just south of the vortex is where westerly winds would form in a tornado (the south side of a cyclonically rotating tornado has westerly winds), which are collocated with the motion of the NCFR. This would make the southern edge of the vortex the location with the strongest winds, which is indeed what was simulated. The exact dynamics of this relationship is an area for further study.

To summarize, a conceptual model of vortexgenesis and maturity is presented. Cyclonic vertical vorticity (orange filled contour) is pre-existing along the front due to the large shift in wind direction across the front (black arrows in Fig. 13a). This vorticity rolls up into discrete vorticity maxima (orange and red filled contours) due to inhomogeneities along the front with an updraft ahead of the front and downdraft behind the front (red and blue arrows, respectively in Fig. 13b). Tilting of horizontal vorticity and stretching of preexisting vorticity occurs east of the front associated with the updraft (green and blue filled contours, respectively Fig. 13c). This stage is considered vortexgenesis. Two mechanisms can be responsible for vortex maturity. The first mechanism, responsible in this case for vortex maturity in the wave and core and gap vortices, is the collocation of tilting and stretching with the updraft and intensification of the stretching within the vortex (due to conservation of angular momentum) while maintaining the same vortex shape and structure (Fig. 13d). The second mechanism is vortex splitting by a strong downdraft with both stretching and tilting dominating vorticity increase in both vorticity maxima (Fig. 13e). The second mechanism was responsible for vortex maturity in the hook, bulging, and broken S signatures in this case. In both mechanisms, the downdraft strengthens, bringing high mo-

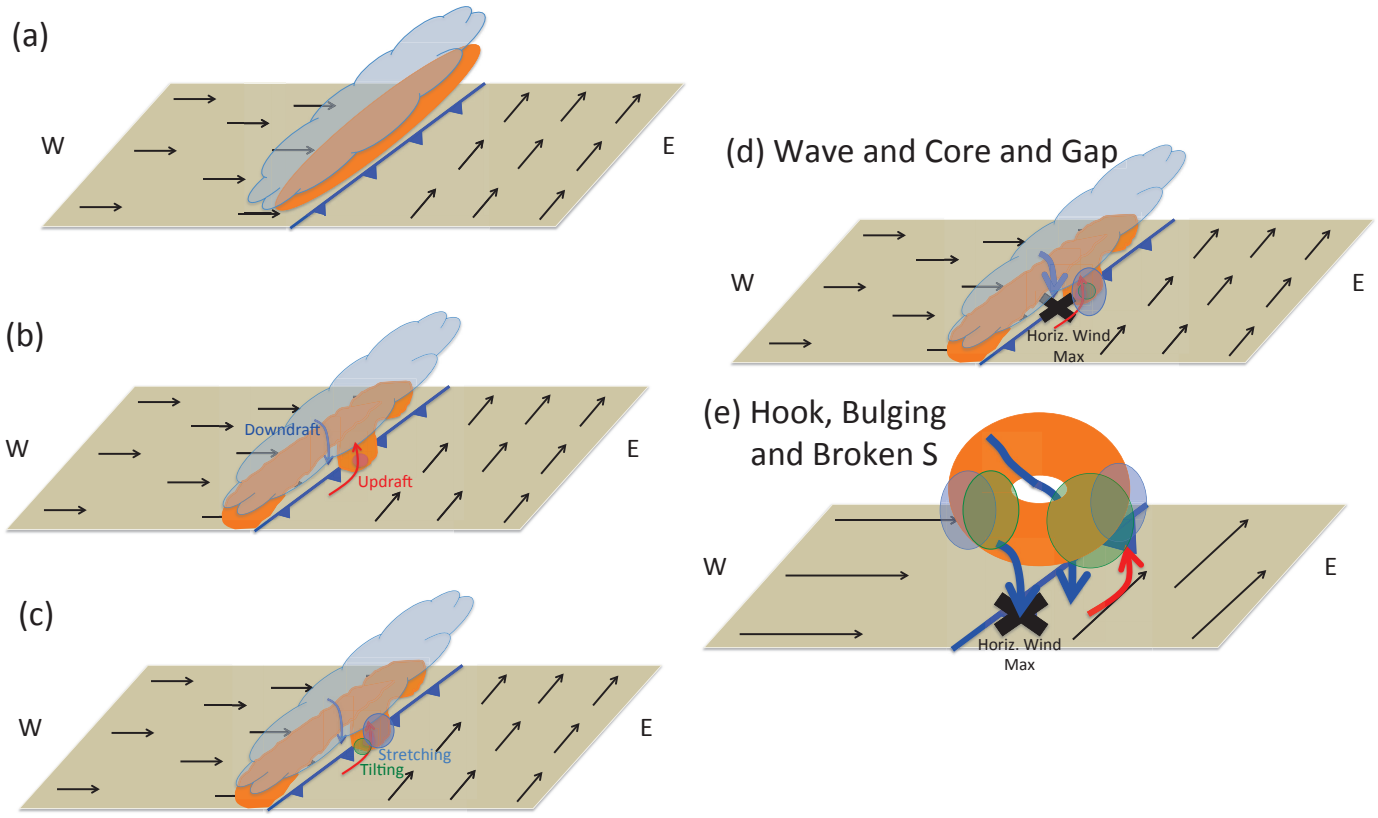

FIG. 13. Conceptual model for vortexgenesis. (a) Cyclonic vertical vorticity (orange) is formed by wind-shift (horizontal winds at surface in black arrows) across a cold front (blue hatched line). Convective precipitation is shown as the gray cloud. (b) Vortex sheet rolls up into discrete vortices by localized updrafts (red arrow). A downdraft (blue arrow) forms to the west of the front. (c) Tilting of horizontal vorticity east of the front (green circle) and stretching (blue circle) form in association with the updraft. This stage is considered vortexgenesis. (d) One outcome of vortex maturity is that tilting and stretching become collocated and more intense. (e) The other outcome of vortex maturity, zoomed in, is vorticity splitting by the downdraft with stretching dominating vortex intensification on the east-side vortex and tilting of horizontal vorticity and stretching dominating vortex intensification on the west-side vortex. In both (d) and (e), the downdraft intensifies (bolder blue arrows), leading to strong horizontal winds at the surface (black X).

mentum air to the surface, creating damaging winds (black X in Fig. 13d and e). This conceptual model at vortexgenesis corresponds to that posed in Lee and Wilhelmson (1997b), but at vortex maturity we found tilting more prominent.

The fact that some of the radar reflectivity signature morphologies changed over the lifetime of some of the vortices, e.g., the hook vortex originated as a wave and the bulging vortex originated as a hook, suggests that the two different mechanisms of vortex maturity could be two stages in maturation rather than two separate processes. In other words, a vortex could mature first by the collocation of stretching and tilting and then split into two vorticity maxima, a subject for future study.

6. Summary

The NCFR of 29 November 2011 produced seven tornadoes. Two of the tornadoes were associated with a broken S, one with a bowing segment, and one with core and gap reflectivity patterns. The other three tornadoes had no apparent reflectivity patterns, but there could have been, for example, a wave or a hook that was too small for the radar to resolve. Vortices producing strong, near-surface horizontal winds associated with a wave, hook, bulge, core and gap, and broken S radar reflectivity signature were analyzed at genesis and maturity. Some of these vortices changed morphologies in their lifetime. The hook vortex originated as a wave, the bulging vortex originated as a hook, and the broken S vortex originated as a bulge.

Using WRF-ARW to analyze the case, cross sections and backward trajectory analysis showed that the dominant mechanism at vortexgenesis for all vortices was stretching. Tilting also occurred at vortexgenesis for the wave, hook, bulging, and broken S vortices. At vortex maturity, there were two mechanisms responsible. For the wave and core and gap vortices, the areas of tilting and stretching were collocated and the vertical vorticity maximum remained the same shape as at vortexgenesis. For the hook, bulging, and broken S vortices, the vertical vorticity maximum was shaped like a doughnut with a downdraft in the middle. Both sides of the vortex were associated with stretching and tilting. This study showed that multiple mechanisms of vortex intensification can occur along the same NCFR.

Acknowledgments.

We thank TORRO, particularly Terence Meaden and Paul Brown, for providing data on British Isles tornadoes. We thank ARCHER UK National Supercomputing Service for hosting the simulations. We thank British Atmospheric Data Centre, Wetter3.de, and the UK Met Office for providing Nimrod system radar data and surface synoptic charts. We thank Chris Dearden for help with WRF setup. We thank Mulder's PhD Committee, Geraint Vaughan, Paul Connolly, and Alan Blythe for their comments. Mulder was funded by a scholarship from the Faculty of Engineering and Physical Sciences, University of Manchester.

REFERENCES

Adlerman, E. J., K. K. Droegemeier, and R. Davies-Jones, 1999: A numerical simulation of cyclic mesocyclogenesis. *J. Atmos. Sci.*, **56**, 2045–2069.

Atkins, N. T. and M. St. Laurent, 2009: Bow echo mesovortices. Part II: Their genesis. *Mon. Wea. Rev.*, **137**, 1514–1532, doi: 10.1175/2008MWR2650.1.

Brady, R. H. and E. J. Szoke, 1989: A case study of nonmesocyclone tornado development in Northeast Colorado: Similarities to waterspout formation. *Mon. Wea. Rev.*, **117**, 843–856.

Brown, P. R. and G. T. Meaden, 2012: TORRO Tornado Division report: November–December 2011. *Int. J. Meteor.*, **37**, 41–47.

Carbone, R. E., 1982: A severe frontal rainband. Part I. stormwide hydrodynamic structure. *J. Atmos. Sci.*, **39**, 258–279.

Clark, M. R., 2011: Doppler radar observations of mesovortices within a cool-season tornadic squall line over the UK. *Atmos. Res.*, **100**, 749–764, doi:10.1016/j.atmosres.2010.09.007.

Clark, M. R., 2012: Doppler radar observations of non-occluding, cyclic vortex genesis within a long-lived tornadic storm over southern England. *Quart. J. Roy. Meteor. Soc.*, **138**, 439–454, doi:10.1002/qj.924.

Clark, M. R. and D. J. Parker, 2014: On the mesoscale structure of surface wind and pressure fields near tornadic and nontornadic cold fronts. *Mon. Wea. Rev.*, **142**, 3560–3585, doi:10.1175/MWR–D–13–00 395.1.

Fujita, T., 1981: Tornadoes and downbursts in the context of generalized planetary scales. *J. of the Atmos. Sci.*, **38**, 1511–1534.

Funk, T. W., K. E. Darmofal, J. D. Kirkpatrick, V. L. DeWald, R. W. Przybylinski, G. K. Schmocker, and Y. J. Lin, 1999: Storm reflectivity and mesocyclone evolution associated with the 15 April 1994 squall line over Kentucky and southern Indiana. *Wea. Forecasting*, **14**, 976–993.

Glickman, T. S., 2000: *Glossary of Meteorology*. 2nd ed., American Meteorological Society.

Grumm, R. H. and M. Glazewski, 2004: Thunderstorm types associated with the "broken-S" radar signature. *Preprints, 22nd Conference on Severe Local Storms*, Vol. 4–8 October 2004, Hyannis, MA, Amer. Meteor. Soc., P7.1. [Available at `https://ams.confex.com/ams/11aram22sls/techprogram/paper_81537.htm`].

James, P. and K. A. Browning, 1979: Mesoscale structure of line convection at surface cold fronts. *Quart. J. Roy. Meteor. Soc.*, **105**, 371–382, doi:10.1002/qj.49710544 404.

Janjić, Z. I., 1994: The step-mountain Eta coordinate model: Further developments of the convection, viscous sublayer, and turbulence closure schemes. *Mon. Wea. Rev.*, **122**, 927–945, doi:10.1175/1520–0493(1994)122<0927:TSMECM>2.0.CO;2.

Kain, J. S., 2004: The Kain–Fritsch convective parameterization: An update. *J. Applied Met.*, **43**, 170–181, doi:10.1175/1520–0450(2004)043<0170:TKCPAU>2.0.CO;2.

Kawashima, M., 2011: Numerical study of horizontal shear instability waves along narrow cold frontal rainbands. *J. Atmos. Sci.*, **68**, 878–903, doi:10.1175/2010JAS3599.1.

Lee, B. D. and R. B. Wilhelmson, 1997a: The numerical simulation of non-supercell tornadogenesis. part

I: Initiation and evolution of pretornadic misocyclone circulations along a dry outflow boundary. *J. Atmos. Sci.*, **54**, 32–60, doi:http://dx.doi.org/10.1175/1520–0469(1997)054<0032:TNSONS>2.0.CO;2.

Lee, B. D. and R. B. Wilhelmson, 1997b: The numerical simulation of nonsupercell tornadogenesis. Part II: Evolution of a family of tornadoes along a weak outflow boundary. *J. Atmos. Sci.*, **54**, 2387–2415, doi: 10.1175/1520–0469(1997)054<2387:TNSONT>2.0.CO;2.

Markowski, P. and Y. Richardson, 2014: What we know and don't know about tornado formation. *Physics Today*, **67**, 26–31, doi: 10.1063/PT.3.2514.

McAvoy, B. P., W. A. Jones, and P. D. Moore, 2000: Investigation of an unusual storm structure associated with weak to occasionally strong tornadoes over the eastern United States. *Preprints, 20th Severe Local Storms Conference, Orlando, FL*, Amer. Meteor. Soc., 182–185.

Mulder, K. J. and D. M. Schultz, 2015: Climatology, storm morphologies, and environments of tornadoes in the British Isles: 1980–2012. *Mon. Wea. Rev.*, **143**, 2224–2240, doi:10.1175/MWR–D–14–00 299.1.

Skamarock, W. C., et al., 2008: A description of the Advanced Research WRF Version 3. Tech. Note TN–475+STR, 113 pp., NCAR.

Smart, D. J. and K. A. Browning, 2009: Morphology and evolution of cold-frontal misocyclones. *Quart. J. Roy. Meteor. Soc.*, **135**, 381–393, doi: 10.1002/qj.399.

Smull, B. F. and R. A. Houze, 1987: Rear inflow in squall lines with trailing stratiform precipitation. *Monthly Weather Review*, **115 (12)**, 2869–2889.

Thompson, G., P. R. Field, R. M. Rasmussen, and W. D. Hall, 2008: Explicit forecasts of winter precipitation using an improved bulk microphysics scheme. Part II: Implementation of a new snow parameterization. *Mon. Wea. Rev.*, **136**, 5095–5115, doi:10.1175/2008MWR2387.1.

Trapp, R. J., S. A. Tessendorf, E. S. Godfrey, and H. E. Brooks, 2005: Tornadoes from squall lines and bow echoes. Part I: Climatological distribution. *Wea. Forecasting*, **20**, 23–34, doi:10.1175/WAF–835.1.

Trapp, R. J. and M. L. Weisman, 2003: Low-level mesovortices within squall lines and bow echoes. Part II: Their genesis and implications. *Monthly Weather Review*, **131**, 2804–2823, doi:10.1175/1520–0493(2003)131<2804:LMWSLA>2.0.CO;2.

Wakimoto, R. M. and J. W. Wilson, 1989: Nonsupercell tornadoes. *Mon. Wea. Rev.*, **117**, 1113–1140, doi:10.1175/1520–0493(1989)117<1113:NST>2.0.CO;2.

Weisman, M. L. and C. A. Davis, 1998: Mechanisms for the generation of mesoscale vortices within quasi-linear convective systems. *Journal of the Atmospheric Sciences*, **55 (16)**, 2603–2622.

Wheatley, D. M. and R. J. Trapp, 2008: The effect of mesoscale heterogeneity on the genesis and structure of mesovortices within quasi-linear convective systems. *Mon. Wea. Rev.*, **136**, 4220–4241, doi:10.1175/2008MWR2294.1.

Chapter 5

Conclusions

Tornadic storms and tornadogenesis have been studied extensively in the United States including storm and tornado dynamics, forecasting techniques, and modeling (e.g., Rasmussen and Blanchard, 1998; Trapp and Weisman, 2003; Markowski et al., 2008; Atkins and St. Laurent, 2009; Smith et al., 2012). In the British Isles, the majority of research on tornadoes has focused on climatologies (e.g., Lacy, 1968; Kirk, 2014). The British Isles are an interesting place to study tornadoes because they occur in low-CAPE (convective available potential energy), high-shear environments and most commonly occur from linear storms, for example, narrow cold-frontal rainbands (e.g., Smart and Browning, 2009; Clark, 2013; Clark and Parker, 2014). Severe weather occurring in low-CAPE, high-shear environments is difficult to forecast and, in the United States, has resulted in high false alarm rates (Dean and Schneider, 2008).

The purpose of this thesis was to study tornadoes along narrow cold-frontal rainbands (NCFRs) in the British Isles. More specifically, there were three sets of research questions this thesis addressed:

1. Where, when, and from what storm types do British Isles tornadoes form? What sounding parameters distinguish tornadic from nontornadic environments? Which areas of the British Isles are most susceptible to tornadoes?

2. Which initialization time and combination of parameterizations lead to the most accurate simulation of a modeled NCFR?

3. What is the mechanism creating vortexgenesis in NCFRs with different radar reflectivity signatures? Is it possible for many mechanisms to be

present? Could tilting also be involved in vortexgenesis with horizontal shearing instability (HSI) present?

To address these research questions, this thesis was comprised of three papers. The first paper was a climatology of tornadoes in the British Isles from 1980–2012, which was published in the June edition of Monthly Weather Review. The second paper, which is not intended for publication, investigated the impacts of different parameterization scheme and initialization time combinations on radar reflectivity for a modeled NCFR that occurred 29 November 2011. The third paper, which is intended for submission to Monthly Weather Review, investigated vortexgenesis and vortex maturity along the modeled tornadic NCFR from the second paper. This chapter will summarize findings from each chapter of this thesis and then conclude with future work.

5.1 Summary of Results

The summary of results is organized by each research question listed above.

5.1.1 Which areas of the British Isles are most susceptible to tornadoes? Where do British Isles tornadoes form?

Previous tornado climatologies in the British Isles have discussed the locations of tornadoes, most commonly by plotting tornado locations on a map (e.g., Kirk, 2014) or by listing tornado frequencies by region (e.g., Holden and Wright, 2004). Spatially smoothed, gridded tornado frequencies, which more accurately portray locations where tornadoes are more likely to occur, have not been plotted since the 1980's (Meaden, 1985a). Therefore, using temporally and spatially smoothed, gridded tornado occurrence data, a tornado probability map was created for the British Isles (Chapter 2, Fig. 5). The locations with the highest probability of tornadoes were typically near cities, but more specifically in southern England between London and Reading, in southeastern England between London and Ipswitch, in the Midlands and Northwest from Bristol north to Manchester and along the south coast of Wales (Chapter 2). This updated probability of tornado occurrence based on location is useful to decision-makers, such as insurance agencies and the public, who have an interest in reducing damage costs.

5.1.2 When do British Isles tornadoes form?

Literature on the annual number of tornadoes (10.3–47.2 per year, Tyrrell, 2003; Kirk, 2014, respectively) and seasons during which tornadoes are most common (e.g., Lacy, 1968; Tyrrell, 2003; Holden and Wright, 2004; Kirk, 2014) in the British Isles have differed greatly. In fact, every season has been cited as having the most tornadoes. These discrepancies are likely due to climatologies including different time periods and covering different areas. Additional differences are due to whether or not waterspouts are included in the dataset. By removing all waterspouts (defined here as tornadoes that only occur over water) from the dataset to study tornadoes that could potentially damage land-based property, omitting tornadoes with uncertain dates, and omitting an unusually large tornado outbreak from 1981, the number of tornadoes per year from 1980–2012 ranged from 12–81 with a mean of 34.3 tornadoes per year (Chapter 2). Tornadoes were most common in the summer and autumn (Chapter 2, Fig. 9), similar to the findings of other recent tornado climatologies (Reynolds, 1999; Tyrrell, 2003; Kirk, 2007, 2014). Tornado outbreaks, or days in which three or more tornadoes occurred, were most common in the autumn (Chapter 2, Fig. 15). Climatologies that cited seasons during which tornadoes most frequently occur other than the summer and autumn were conducted many decades ago (e.g., Lacy, 1968) or spanned only a few years (e.g., Holden and Wright, 2004).

Tornadoes in the British Isles were also found to occur throughout the year with less of a peak during the summer and autumn months than the central United States has in their peak tornado season, spring (Chapter 2, Fig. 10 compared to Fig. 11). This finding is interesting from a forecasting and publicity standpoint. In the United States, forecasters and the public are aware of the threat of tornadoes during the spring. There is typically publicity about tornado safety leading up to the central United States "tornado season." In the British Isles, however, tornadoes are a threat year-round, making it more difficult on both the forecasters and the public as tornadoes are always a threat.

5.1.3 What sounding parameters distinguish tornadic from nontornadic environments?

In the United States, forecasters have found a set of forecast parameters to help them distinguish potentially tornadic from nontornadic days. For example, at

least 10 m s^{-1} of low-level (0–1 km) shear and 20 m s^{-1} of deep-layer (0–6 km) shear were found to be a threshold for significant (F2 or stronger) tornadoes in the United States (Craven and Brooks, 2004). This type of analysis has not been done in the British Isles. Therefore, I conducted a proximity sounding analysis, collecting soundings within 3 hours and 180 km of tornadoes and "null" days, that is days in which there were thunderstorms but no tornadoes. I also subdivided the tornadoes into outbreak days and significant tornadoes. Parameters derived from the soundings included low-level (0–1 km) shear, deep-layer (0–6 km) shear, convective available potential energy (CAPE), convective inhibition (CIN), lifting condensation level (LCL) height, and level of free convection (LFC). These parameters were compared between null, tornadic, outbreak, and significant tornadoes to determine if there were any clear thresholds that would help a forecaster determine a tornadic, outbreak, or significant tornado day from a day in which no tornadoes occur.

There was no statistically significant difference in low-level shear between null, tornadic, outbreak, and significant tornadoes and only 3 of the 7 significant tornadoes included in the analysis exceeded the 10 m s^{-1} threshold suggested by Craven and Brooks (2004) (Chapter 2, Fig. 17a). There was lower deep-layer shear in tornadic cases than null cases with a mean deep-layer shear in tornadic cases of 20.5 m s^{-1} compared to a mean of 23.3 m s^{-1} for null cases (significant at $p > 0.05$, Chapter 2, Fig. 17b). All but one significant tornado had deep-layer shear below the 20 m s^{-1} threshold cited for significant tornadoes in the United States (Craven and Brooks, 2004). However, the mean deep-layer shear value for null cases was higher than this threshold, signifying that there are higher shear environments in the British Isles than the United States and that deep-layer shear is not necessarily a good predictor of a tornadic day. Tornado and outbreak cases had statistically significantly higher CAPE than null cases ($p < 0.01$ and $p = 0.02$, respectively), however there were some tornadic soundings with zero CAPE and some null soundings with non-zero CAPE (Chapter 2, Fig. 17c). Overall, CAPE values were much lower in the British Isles than those in the United States. Significant tornadoes in the United States can had a median of approximately 1000 J Kg^{-1} but can have CAPE exceeding 4000 J Kg^{-1} (Grams et al., 2012). In the British Isles, the median CAPE for significant tornadoes was 39.7 J Kg^{-1} (Chapter 2, Fig. 17c). Although CAPE values were higher for tornado and outbreak cases, CAPE alone cannot be relied upon as a forecasting threshold

because some tornado cases occurred in zero CAPE conditions whereas some null cases had non-zero CAPE. There was no statistically significant difference in mean CIN between null and tornado cases, however there was less mean CIN in outbreak cases than all tornado cases ($p = 0.02$, Chapter 2, Fig. 17d). There was less CIN in tornado cases in the British Isles with a mean of 10 J Kg^{-1} compared to 30 J Kg^{-1} in the United States (Grams et al., 2012). The difference in CIN between null, tornadic, outbreak, and significant tornado cases were within a few J Kg^{-1} (Chapter 2, Fig. 17d). The difference in CIN between null, tornadic, outbreak, and significant tornado cases were within a few J Kg^{-1} (Chapter 2, Fig. 17d), meaning CIN is not a robust forecasting tool for predicting tornadic environments. Mean LCL heights in both tornado and outbreak cases were lower than in null cases ($p = 0.01$ for both) and the mean LCL heights for outbreak cases was lower than all tornado cases ($p < 0.01$, Chapter 2, Fig. 17e). In the United States, 75% of significant tornadoes occurred with LCL heights less than 1200 m above ground level (Craven and Brooks, 2004). In the British Isles, 90% of tornadic and 88% of null cases had LCL heights less than 1200 m above ground level, suggesting that the threshold in the United States was not applicable in the British Isles. Finally, the mean LFC height was not statistically different between the null, tornadic, outbreak, and significant tornado cases (Chapter 2, Fig. 17f). Overall, LFC heights in the British Isles were lower than those in the United States. The median LFC height in the United States for supercells producing F0–F1 tornadoes was 1871 m and 2338 m for nontornadic supercells (Davies, 2004). In contrast, 82% of tornado cases and 84% of tornado cases had LFC heights below 1871 m (Chapter 2, Fig. 17e), again meaning the threshold LFC height in the United States does not apply in the British Isles.

There were no clear thresholds in low-level shear, deep-layer shear, CAPE, convective inhibition, lifted condensation level, or level of free convection between null, tornadic, outbreak, or significant tornadoes (Chapter 2, Fig. 17). Additionally, the environments in which tornadoes occur in the British Isles are different from those in the United States. Tornadoes typically occur in low-CAPE, high-shear environments in the British Isles. Tornadoes occurring in low-CAPE, high-shear environments have been difficult to forecast and have caused high false alarm rates in the United States (Dean and Schneider, 2008). In addition, there were lower LCL and LFC heights in the British Isles than those in the United States. Overall, I found that the thresholds used for forecasting tornado days in

the United States are not applicable in the British Isles. This finding supports the notion that tornadoes in the British Isles typically occur in different environments than in the United States. Many idealized modeling studies are initialized using, for example, high CAPE values (e.g., 2200 J Kg^{-1} in Trapp and Weisman, 2003) that are not representative of the environments in the British Isles. Therefore, the results of the idealized simulations do not necessarily represent situation that occur in the British Isles. The results from the proximity sounding analysis emphasize the need for studies on tornadoes in low-CAPE, high-shear environments.

5.1.4 From what storm types do British Isles tornadoes form?

A parent storm analysis has not been conducted in the British Isles before. Previous research has anecdotally stated that most tornadoes occur from linear storms (e.g., Lacy, 1968; Elsom, 1985; Meaden, 1985a), but until now, this had not been systematically studied. To conduct a parent storm analysis, I analyzed radar reflectivity patterns from 254 tornadoes with known locations, dates, times, and that had corresponding radar reflectivity available (a subset of 20% of all the cases from the climatology in Chapter 2) and classified the reflectivity patterns as linear, isolated cell, nonlinear, or cluster (Chapter 2, Fig. 2). The most common parent storm type producing tornadoes was linear storms, producing 42% of tornadoes and 51% of tornado outbreaks (Chapter 2, Fig. 3). The second most common parent storm type was isolated cells, producing 28% of tornadoes (Chapter 2, Fig. 3). In the United States, the distribution is opposite with 18% of tornadoes produced by linear storms and 79% produced by isolated cells (Trapp et al., 2005).

Knowledge of the most common parent storm type producing tornadoes in the British Isles is helpful from a forecasting perspective. Not only does this information help forecasters as they examine radar imagery, but tornadoes from different parent storm types typically produce different strengths of tornadoes, have different storm environments (as investigated in the previous research question), and have different mechanisms of tornadogenesis (Agee and Jones, 2009). Knowing parent storm types also helps focus studies on the dynamics of tornadogenesis. The finding that linear storms are the most common parent storm type

focused the remaining research questions in this thesis to study tornadoes along linear storms, in particular narrow cold-frontal rainbands (NCFRs).

5.1.5 Which initialization time and combination of parameterizations lead to the most accurate simulation of a modeled NCFR?

To model the dynamics of tornadogenesis along NCFRs in the British Isles, it is necessary to have an accurate simulation. To determine which initialization time and combination of parameterizations most accurately simulate a modeled NCFR, I used a case study of a NCFR occurring on 29 November 2011, which produced 7 observed tornadoes across Wales and northern England (Chapter 3). I used the Advanced Research Weather and Forecasting Model (WRF-ARW Skamarock et al., 2008) to model the case using 96 combinations of initialization times, planetary boundary layer schemes, microphysics schemes, and land-surface schemes. The simulations were analyzed by the shape and longevity of the NCFR using radar reflectivity in the x–y and x–z directions and by near-surface temperature, relative humidity, wind speed, wind direction, and sea-level pressure (Chapter 3).

Initialization times further away from the time of analysis produced broken linear convection for most valid times rather than an NCFR (Chapter 3, Fig. 5). Additionally, when the earlier initialization times did produce an NCFR, they occurred in the wrong locations compared to the observed reflectivity (Chapter 3, Fig. 5 compared to Fig. 2). Therefore, the initialization time closest to the time of analysis was chosen as the best. Previous literature has also found that WRF models initialized closer to the analysis time were most accurate in both a UK flooding event (Champion and Hodges, 2014) and for snowbands over the English Channel (Norris et al., 2013).

The planetary boundary layer scheme only produced subtle differences in the simulations. Of the two planetary boundary layer schemes, the Mellor-Yamada-Janjic scheme (MYJ Janjić, 1994) produced an NCFR with a more similar shape to the observed reflectivity than the Yonsei University scheme (YSU Hong et al., 2006) (Chapter 3, Fig. 9a and b compared to Fig. 2). The model had 90 vertical levels for all 96 simulations. Because of the high vertical resolution, the MYJ scheme, which only allows neighboring layers to mix (called local mixing), should adequately resolve planetary boundary layer mixing. Additionally, schemes that

parameterize mixing like the YSU scheme have been found to over-predict CAPE more than local schemes like the MYJ (Cohen et al., 2015), which could yield an unrealistic model, especially in low-CAPE tornadic environments such as in the British Isles (Chapter 2). Therefore, the MYJ planetary boundary layer scheme was chosen as more representative for this case.

There were three microphysics schemes tested for the NCFR case study: the WRF Single-Moment 6-class (WSM6 Hong and Lim, 2006), Morrison 2-moment (Morrison et al., 2009), and the Thompson et al. (2008) schemes. The main difference between the microphysics schemes was whether it was single- or double-moment. A single-moment scheme (such as WSM6) only predicts the mixing ratios for liquid and ice classes. A double-moment scheme (such as Morrison) predicts the mixing ratios and number concentration of the liquid and ice classes. The Thompson scheme is considered single-moment except for a double-moment cloud-ice variable. All three microphysics schemes underestimated the extent of the stratiform rainfall (Chapter 3, Fig. 14), which has been documented in previous research (e.g., Adams-Selin et al., 2013; Hagos et al., 2014; Morrison et al., 2009). The Thompson scheme was found to produce an NCFR with the most similar shape and width as the observed reflectivity (Chapter 3, Fig. 14c compared to Fig. 2). Even though the Morrison scheme was more computationally complicated and therefore should produce more similar results to the observed (Bryan and Morrison, 2012), the resulting NCFR was not the most similar to observed and was more computationally expensive. Therefore, the Thompson et al. scheme was chosen as more suitable.

The two land-surface schemes tested in Chapter 3 were the Noah Land-Surface Model and the Five-Layer Thermal Diffusion scheme. Of the two, the Noah scheme is more complicated, including four layers of soil moisture and temperature as well as snow cover and frozen soil physics. The Five-Layer scheme, on the other hand, only includes soil temperatures over five layers. There was little difference between the land-surface schemes in terms of radar reflectivity, temperature, wind direction, wind speed, and sea-level pressure (Chapter 3, Figs. 9–14). This is likely because the NCFR simulation only lasted 6 hours, whereas land-surface schemes tend to make a bigger difference over long-term simulations. Because there was little difference between the schemes, the less computationally expensive scheme, the Five-Layer scheme, was chosen as more suitable.

The most accurate simulation of the NCFR occurring on 29 November 2011

was initialized at 1200 UTC and used the MYJ planetary boundary layer scheme, Thompson et al. microphysics scheme, and Five-Layer Thermal Diffusion land-surface scheme. One caveat of this study was that the combination of initialization time and parameterization schemes are not necessarily representative of all NCFRs in all locations at all times, just this particular case. By testing the different combinations of parameterizations and determining the most suitable combination, analysis of the dynamics associated with vortices along the NCFR (Chapter 4) were more reliable.

5.1.6 What is the mechanism creating vortexgenesis in NCFRs with different radar reflectivity signatures? Is it possible for many mechanisms to be present? Could tilting also be involved in vortexgenesis with HSI present?

Findings from Chapter 2 verified that the most common storm type that produces tornadoes in the British Isles was linear storms. This finding motivated the final research questions, which revolve around the central theme: what causes vortices along linear storms in the British Isles?

Vortices along NCFRs are associated with strong winds and tornadoes (e.g., Wakimoto and Wilson, 1989; Smart and Browning, 2009; Clark and Parker, 2014). These tornadoes can be short-lived, making them a tricky operational forecasting problem. Therefore, it is important to understand the mechanisms leading to vortexgenesis and vortex maturity.

Vortexgenesis and tornadogenesis have been studied extensively for supercells (e.g., Davies-Jones, 2014; Markowski and Richardson, 2014) and bow echoes (e.g., Trapp and Weisman, 2003; Atkins and St. Laurent, 2009). For a supercell tornado to form, there must first be a mesocyclone, or a rotating vortex 2–10 km in diameter located 3–7 km above the ground, which forms as horizontal vorticity is tilted upwards into the updraft, therefore becoming vertical vorticity. This causes the entire updraft to rotate. The second step is that downdraft air acquires horizontal vorticity due to temperature variations between the cooler air near the storm (through evaporation of rain and melting of hail and snow) and warm environmental air ahead of the storm. This horizontally rotating wind moves toward the surface and tilts upwards due to surrounding wind, creating vertical vorticity

near the ground. In the third and final step, the near-surface vertical vorticity is stretched by perturbation pressure gradient force-induced suction. This stretching increases vorticity due to conservation of angular momentum (Davies-Jones, 2014; Markowski and Richardson, 2014, for more details, see Chapter 1, Section 1.3 and Fig. 1.2). In the radar reflectivity, supercell tornadoes are often associated with a hook signature.

One hypothesis of vortexgenesis in bow echoes is the same as that of supercells (Atkins and St. Laurent, 2009, for more details, see Chapter 1, Section 1.4, and Fig. 1.5). Another hypothesis on the formation of vortices in bow echoes is that horizontal vorticity is created by temperature differences between the cooler air near the storm, cooled by evaporation of rain and melting of snow and hail, similar to the second step of tornadogenesis in supercells. This horizontal vorticity is tilted by the downdraft caused by the rain in the storm. The downward tilting of the horizontal vorticity causes a cyclonic and anticyclonic vertical vorticity couplet on the south and north sides of the downdraft, respectively. Stretching of planetary vorticity enhances the cyclonic vortex (Trapp and Weisman, 2003, for more details, see Chapter 1, Section 1.4, and Fig. 1.3). Conversely, another hypothesis of vortexgenesis in bow echoes states that preexisting horizontal vorticity either generated by vertical wind shear (Weisman and Davis, 1998) or temperature gradients (Atkins and St. Laurent, 2009) is tilted upwards by an updraft, creating vortex couplets in opposite positions of that proposed by Trapp and Weisman (2003): anticyclonic vortex south and cyclonic vortex to the north. Again, stretching and conservation of angular momentum strengthens the vorticity (Weisman and Davis, 1998; Atkins and St. Laurent, 2009, for more details, see Chapter 1, Section 1.4, and Fig. 1.4). Regardless of the mechanism, all bow echo vortexgenesis hypotheses require both tilting and stretching.

For NCFR tornadoes, vortexgenesis is often explained by horizontal shearing instability, or HSI. In these circumstances, there is preexisting vertical vorticity due to a change in wind direction, for example across a front. Inhomogeneities along the front, such as friction or temperature variations (Carbone, 1982; Lee and Wilhelmson, 1997b), helps concentrate the sheet of vertical vorticity into individual vortices. These vortices can interact and merge into larger vortices. The updraft along the front deepens the vorticity through advection of vertical vorticity. The updraft also strengthens the vorticity through stretching by conservation of angular momentum. The vortices are maintained by vorticity advection and

tilting of horizontal vorticity, but the tilting was not found to be a significant source of vorticity (Lee and Wilhelmson, 1997b, for more details, see Chapter 1, Section 1.5, and Fig. 1.6). In this mechanism, it is only stretching involved in vortexgenesis. Tilting that does occur is small and is only present to maintain the vortices.

Along NCFRs, four radar reflectivity signatures are known to be associated with tornadoes: the broken S (e.g., McAvoy et al., 2000; Clark, 2011), bow echoes (e.g. Funk et al., 1999; Clark, 2011), hook (e.g., Carbone, 1982; Clark, 2011), and core and gap (e.g., Kawashima, 2011). With all the different reflectivity patterns associated with tornadoes along NCFRs, it begs the question of what mechanism causes vortexgenesis along the NCFR, especially because hook echoes are associated both with NCFRs and supercells and that mechanisms involved in vortexgenesis along bow echoes differ from the HSI hypothesis of vortexgenesis. More specifically, tilting is a necessary mechanism in both supercell and bow echo vortexgenesis, but is not hypothesized as being significant in HSI vortexgenesis. So which vortexgenesis mechanism is present along an NCFR with multiple vortices? Could there be more than one mechanism along the same line? Is there tilting?

The NCFR on 29 November 2011 produced seven observed tornadoes associated with a broken S, bowing segment, and core and gap (Chapter 4, Fig. 2). There were three tornadoes, however, that had no apparent radar reflectivity signature and occurred along an apparently straight segment of the NCFR (Chapter 4, Fig. 2). It is possible that there was a small wave or hook present in the reflectivity, however due to the coarse radar resolution, it was not visible.

Using the model set-up from Chapter 3, the NCFR on 29 November 2011 was modeled to 200-meter horizontal grid spacing (model domains are in Chapter 4, Fig. 3). The simulated NCFR exhibited vortices associated with five different radar reflectivity signatures: wave, hook, bulge, core and gap, and broken S. Examples of a vortex associated with each radar reflectivity signature was chosen for analysis (Chapter 4, Fig. 5) both at vortexgenesis and vortex maturity, defined as when strong horizontal winds occurred at the surface. The resolution in this simulation was too coarse to resolve a tornado, therefore strong horizontal winds were used as a diagnostic, even though we do not know if a tornado would be associated with the vortex or not.

Cross sections of and backward trajectories from the vortices at genesis and

maturity were used to analyze the structure and mechanisms creating the vortices and leading to maturity. At vortexgenesis, all vortices looked similar with an updraft east of the front collocated with positive vertical vorticity. In all vortices except the broken S, there was negative vertical velocity at the surface west of the vorticity maxima. The vertical vorticity was tilted upward, away from the surface to the north (Chapter 4, Fig. 8). Backward trajectories showed that vortexgenesis for the core and gap vortex occurred by stretching alone, similar to Lee and Wilhelmson (1997b) (Chapter 4, Fig. 11). However, there was tilting on the south side of the wave, hook, bulging, and broken S vortices, verified by both cross section and backward trajectory analysis (Chapter 4, Figs. 8 and 11, respectively), which is contrary to the HSI vortexgenesis hypothesis (Lee and Wilhelmson, 1997b) because tilting is present. The positive tilting that was present, however, was separated in space from the positive stretching (Chapter 4, Fig. 8).

At vortex maturity, there were two morphologies present. The first occurred in the wave and core and gap vortices. In the first morphology, the positive vertical vorticity had the same shape and structure as in vortexgenesis, with vorticity tilting upward away from the surface toward the north. Positive stretching and tilting were collocated at maturity (Chapter 4, Fig. 9). This model is consistent with the hypothesis of HSI vortices from Lee and Wilhelmson (1997b), who stated that tilting was present after vortexgenesis to maintain the vortices.

The second morphology of vortex maturity was present in the mature hook, bowing, and broken S vortices. The positive vertical vorticity maxima in the second morphology was broken in two, separated by a downdraft or weak updraft (Chapter 4, Fig. 9). The downdraft or weak updraft was associated with negative tilting and weak stretching, making this region not conducive to vorticity production, explaining the gap in positive vertical vorticity. In the hook and bowing vortices, stretching was the dominant mechanism from the trajectory analysis, however both tilting and stretching was present in the cross section (Chapter 4, Figs. 12 and 9, respectively). Tilting was dominant in vortex maturity for the broken S vortex from the trajectory analysis, even though tilting and stretching were both present in the vortex in the cross section (Chapter 4, Figs. 12 and 9, respectively). The location of the trajectory from the backward trajectory analysis likely had an influence on these results. The importance of tilting in vortexgenesis and vortex maturity, especially in the broken S vortex, is contrary to the HSI

hypothesis from Lee and Wilhelmson (1997b) and points at a mechanism more similar to the mechanisms of bow echo vortexgenesis (Trapp and Weisman, 2003; Atkins and St. Laurent, 2009).

The results from Chapter 4 were combined to form a conceptual model for vortexgenesis and vortex maturity in the NCFR (Chapter 4, Fig. 13). The conceptual model for vortexgenesis is based on the hypothesis of HSI vortexgenesis from Lee and Wilhelmson (1997b). Initially, a vortex sheet formed as a result of horizontal directional wind shear across the cold front. The vortex sheet rolled up into discrete vortices do to inhomogeneities along the front and formed an updraft to the east of the front and a downdraft west of the front. At vortexgenesis, the vortices had positive vorticity along the updraft on the east side of the front. Stretching dominated vorticity production at vortexgenesis, although weak tilting on the south side of the wave, hook, bulging, and broken S vortices was also observed in the cross section and trajectory analyses.

Two different mechanisms were observed as the vortices reached maturity. The first mechanism, which was responsible for the maturity of the wave and core and gap vortices, was intensification and collocation of stretching and tilting, seen in both the cross section and trajectory analyses. The second mechanism, responsible for the maturity of the hook, bulging, and broken S vortices, involved vorticity maxima being split in two parts by the downdraft. Both sides of the positive vorticity maxima were associated with tilting and stretching (from the cross section analysis). It is unclear whether the two mechanisms are two separate mechanisms or if they are different stages of the same mechanism. Regardless of the mechanism for vortex maturity, all vortices at maturity had a strong downdraft south of the vortex maximum, which is likely responsible for the damaging horizontal winds at the surface by transporting high momentum air from the rear inflow jet of the NCFR downward. The relationship between this downdraft and the damaging horizontal winds near the surface is subject to further study.

The conceptual model presented in Chapter 4 at vortexgenesis is similar to the hypothesis presented by Lee and Wilhelmson (1997b) with stretching being the dominant mechanism. However, the findings in Chapter 4 suggest that tilting is present in some vortices at genesis, unlike the hypothesis from Lee and Wilhelmson (1997b). Although stretching is the dominant mechanism in vortex maturity in most vortices (similar to the hypotheses of Lee and Wilhelmson, 1997b; Trapp and Weisman, 2003; Atkins and St. Laurent, 2009), tilting appears to be required

to sustain the vortices over time.

From Chapter 4, a conceptual model for vortexgenesis and vortex maturity along a tornadic NCFR was produced. It is possible for many mechanisms to be responsible for tornadogenesis along the NCFR. Additionally, findings from Chapter 4 suggest that tilting is an important mechanism required for vortexgenesis and vortex maturity when HSI is present.

5.2 Future work

The research conducted for this thesis is far from comprehensive and has raised questions for future research. Because tornado climatologies are dependent upon tornado reports, an attempt to quantify tornado underreporting would be useful in determining how complete any given climatology is. This could be done by first analyzing the causes for underreporting, which would put climatologies into context. For example, it is hypothesized that tornadoes are underreported in areas with low population density (e.g. Minor et al., 1980; Dotzek, 2001; Setvák et al., 2003; Anderson et al., 2007; Brooks and Dotzek, 2008; Dias, 2011; Brázdil et al., 2012; Sioutas et al., 2013) and that an increase in tornado reports over the past decade could be due to increased availability of technology, such as the availability of high-quality cameras on cell phones (e.g., Dotzek, 2003; Dias, 2011; Gayà, 2011; Kron et al., 2012; Simeonov et al., 2013). Analyzing these factors over time could help us normalize the number of tornado reports. This type of analysis has been conducted previously in the United States based on population density (e.g., Anderson et al., 2007; Widen et al., 2013; Paulikas, 2014), but this analysis has not been conducted in the British Isles or with other proposed causes of underreporting such as the increase in technology.

One limitation of Chapter 4 is that it was a case study of a single NCFR with results not necessarily generalizable to all tornadic NCFRs. To help generalize the findings from Chapter 4, vorticity equation analysis comparing numerous simulated NCFRs is necessary. Additionally, comparison to terms of the vorticity equation from observed NCFRs would verify results from the simulations. Clark and Parker (2014) have used time-compositing of surface weather station data to calculate vertical vorticity and stretching. However furthering this analysis by including tilting would help verify the results from Chapter 4. Until December 2012, Doppler radar data were not available for the entire UK radar network. Now

that Doppler radars are fully operational, velocity analysis, from which terms of the vorticity equation can be derived, is now possible. These data can be used in addition to the surface weather observations from Clark and Parker (2014) in observational studies of vortices along NCFRs similar to the studies of Straka et al. (2007) and Markowski et al. (2008), for example.

Determining environments conducive to tornadogenesis along NCFRs is helpful from a forecasting perspective so that warnings and alerts can be issued with adequate lead time. One finding from Chapter 4 was that tilting of horizontal vorticity plays a role in vortexgenesis and vortex maturity along the simulated NCFR. Further investigation into the origin of the horizontal vorticity, whether it was crosswise or streamwise, would help complete the conceptual model presented and would help forecasters understand the environments more conducive to tornadogenesis as those conditions developed. Vortex line analysis would also verify the results from Chapter 4 by determining the location, direction, and evolution of vorticity as the vortices formed and matured, similar to studies conducted on supercells (e.g., Straka et al., 2007).

The comparison of tornadic and nontornadic NCFRs is also helpful from a forecasting perspective. Being able to determine if an NCFR is capable of producing tornadoes as it forms increases lead times for tornado warnings. Tornadic NCFRs tend to have larger differences in wind direction and temperature across the front when compared to nontornadic NCFRs (Wakimoto and Wilson, 1989; Lee and Wilhelmson, 1997a; Kawashima, 2011; Clark, 2013; Clark and Parker, 2014). A simulation of a nontornadic NCFR that analyzes the evolution of vorticity would provide further information on why an NCFR is nontornadic. Further, the same analysis of evolution of vorticity of a nontornadic vortex along a tornadic NCFR would be useful to see if there are particular dynamics or environments that promote or prevent tornadogenesis.

One finding from Chapter 4 was that the downdraft was instrumental in creating damaging horizontal winds at the surface, a similar finding to previous research (e.g., Smart and Browning, 2009). Previous studies on strong winds and tornadoes in NCFRs found that no uniform increase of vorticity occurred prior to the onset of strong winds or tornadogenesis (Smart and Browning, 2009; Clark and Parker, 2014). To further understand the role of the rear inflow jet in surface wind production and to perhaps identify a precursor for the onset of strong winds or tornadogenesis, a further study on tornadic misocyclones using

the momentum equation should be conducted. This study would be structured similar to Chapter 4. However the momentum equation would be used in place of the vorticity equation, similar to the studies of Rotunno and Klemp (1985) and Mahoney et al. (2009).

Finally, the results from Chatper 4 raised further questions about horizontal shearing instability (HSI). Two methods of diagnosing HSI have been used in previous literature. The first is assessing the distance between vortices along a line of convection (e.g., Jorgensen et al., 2003; Wheatley and Trapp, 2008; Smart and Browning, 2009; Clark and Parker, 2014). According to Miles and Howard (1964), the distance between the vortices should be approximately 7.5 times the width of the vortex sheet. Using scale analysis, any reasonable width of the vortex sheet or NCFR would result in distances between 5 and 30 km, all of which were reported in literature as the spacing between vortices and thus verification of HSI as a vorticity generation mechanism (e.g., Jorgensen et al., 2003; Wheatley and Trapp, 2008; Smart and Browning, 2009; Clark and Parker, 2014). Perhaps the distance diagnosis is not the most robust diagnosis of HSI. The other method of diagnosing HSI is the observation of single cyclonic vortices rather than cylconic-anticyclonic vorticity couplets (e.g., Trapp and Weisman, 2003; Wheatley and Trapp, 2008; Clark, 2011; Clark and Parker, 2014). According to Lee and Wilhelmson (1997b), vortexgenesis from HSI occurs from strengthening of preexisting vorticity due to stretching alone. Therefore, only cyclonic vortices would be produced, not cyclonic-anticyclonic vorticity couplets such as those observed in bow echoes (e.g., Trapp and Weisman, 2003; Atkins and St. Laurent, 2009). In Chapter 4, tilting was found to increase vorticity at vortexgenesis and vortex maturity, therefore anticylonic vortices could exist, and were observed in the broken S and core and gap vortices in Chapter 4. Further studies confirming the plausibility of cyclonic-anticyclonic vorticity couplets forming from HSI would prevent misdiagnosis of HSI. Perhaps future study into HSI would find a more suitable diagnostic for future studies to use.

Bibliography

Adams-Selin, R. D., S. C. van den Heever, and R. H. Johnson, 2013: Sensitivity of bow-echo simulation to microphysical parameterizations. *Wea. Forecasting*, **28**, 1188–1209.

Agee, E. and E. Jones, 2009: Proposed conceptual taxonomy for proper identification and classification of tornado events. *Wea. Forecasting*, **24**, 609–617, doi:10.1175/2008WAF2222 163.1.

Agee, E. M., 2014: A revised tornado definition and changes in the tornado taxonomy. *Wea. Forecasting*, **29**, 1256–1258, doi:10.1175/WAF–D–14–00 058.1.

Anderson, C. J., C. K. Wikle, Q. Zhou, and J. A. Royle, 2007: Population influences on tornado reports in the United States. *Wea. Forecasting*, **22**, 571–579.

Atkins, N. T. and M. St. Laurent, 2009: Bow echo mesovortices. Part II: Their genesis. *Mon. Wea. Rev.*, **137**, 1514–1532.

Brady, R. H. and E. J. Szoke, 1989: A case study of nonmesocyclone tornado development in Northeast Colorado: Similarities to waterspout formation. *Mon. Wea. Rev.*, **117**, 843–856.

Brázdil, R., K. Chromá, P. Dobrovolný, and Z. Černoch, 2012: The tornado history of the Czech Lands, AD 1119–2010. *Atmos. Res.*, **118**, 193–204.

Brooks, H. E. and C. A. Doswell III, 2001: Some aspects of the international climatology of tornadoes by damage classification. *Atmos. Res.*, **56**, 191–201, doi:10.1016/S0169–8095(00)00 098–3.

Brooks, H. E. and N. Dotzek, 2008: *The spatial distribution of severe convective storms and an analysis of their secular changes*, 35–53. Climate Extremes and Society, Cambridge University Press.

Brown, P. R., G. T. Meaden, and M. W. Rowe, 2012: Tornadoes in Great Britain and Ireland to 1960: Part1: Years AD 1054–1800. *Int. J. Meteorol.*, **37**, 145–154.

Bryan, G. H. and H. Morrison, 2012: Sensitivity of a simulated squall line to horizontal resolution and parameterization of microphysics. *Mon. Wea. Rev.*, **140**, 202–225.

Calhoun, K. M., T. M. Smith, D. M. Kingfield, J. Gao, and D. J. Stensrud, 2014: Forecaster use and evaluation of real-time 3DVAR analyses during severe thunderstorm and tornado warning operations in the Hazardous Weather Testbed. *Wea. Forecasting*, **29**, 601–613, doi:10.1175/WAF–D–13–00 107.1.

Carbone, R. E., 1982: A severe frontal rainband. Part I. stormwide hydrodynamic structure. *J. Atmos. Sci.*, **39**, 258–279.

Carbone, R. E., 1983: A severe frontal rainband. Part II: Tornado parent vortex circulation. *J. Atmos. Sci.*, **40**, 2639–2654.

Champion, A. J. and K. Hodges, 2014: Importance of resolution and model configuration when downscaling extreme precipitation. *Tellus*, **66 (1–16)**.

Clark, M. R., 2009: The southern England tornadoes of 30 December 2006: Case study of a tornadic storm in a low CAPE, high shear environment. *Atmos. Res.*, **93**, 50–65.

Clark, M. R., 2011: Doppler radar observations of mesovortices within a cool-season tornadic squall line over the UK. *Atmos. Res.*, **100**, 749–764.

Clark, M. R., 2012: Doppler radar observations of non-occluding, cyclic vortex genesis within a long-lived tornadic storm over southern England. *Quart. J. Roy. Meteor. Soc.*, **138**, 439–454, doi:10.1002/qj.924.

Clark, M. R., 2013: A provisional climatology of cool-season convective lines in the UK. *Atmos. Res.*, **123**, 180–186.

Clark, M. R. and D. J. Parker, 2014: On the mesoscale strucure of surface wind and pressure fields near tornadic and nontornadic cold fronts. *Mon. Wea. Rev.*, **142**, 3560–3585.

Cohen, A. E., S. M. Cavello, M. C. Coniglio, and H. E. Brooks, 2015: A review of planetary boundary layer parameterization schemes and their sensitivity in simulating Southeastern U.S. cold season severe weather environments. *Wea. Forecasting*, **30**, 591–612, doi:10.1175/WAF–D–14–00 105.1.

Craven, J. P. and H. E. Brooks, 2004: Baseline climatology of sounding derived parameters associated with deep moist convection. *Nat. Wea. Dig.*, **28**, 13–24.

Dahl, J. M. L., M. D. Parker, and L. J. Wicker, 2014: Imported and storm-generated near-ground vertical vorticity in a simulated supercell. *J. Atmos. Sci.*, **71**, 3027–3051, doi:10.1175/JAS–D–13–0123.1.

Davies, J. M., 2004: Estimations of CIN and LFC associated with tornadic and nontornadic supercells. *Wea. Forecasting*, **19**, 714–726, doi:10.1175/1520–0434(2004)019<0714:EOCALA>2.0.CO;2.

Davies-Jones, R., 2014: A review of supercell and tornaod dynamics. *Atmos. Res.*, **158-159**, 274–291, doi:10.1016/j.atmosres.2014.04.007.

Davies-Jones, R. and P. Markowski, 2012: Can a gust front tilt horizontal vortex lines to produce a tornado? Preprints, 26th Conference on Severe Local Storms, Nashville, TN, Amer. Meteor. Soc. [Available online at https://ams.confex.com/ams/26SLS/webprogram/Paper212 378.html].

Dean, A. R. and R. S. Schneider, 2008: Forecast challenges at the NWS Storm Prediction Center relating to the frequency of favorable severe storm environments. *Preprints, 24th Conf. on Severe Local Storms, Savannah, GA, Amer. Meteor. Soc.*, [Available online at https://ams.confex.com/ams/pdfpapers/141743.pdf.].

Dias, M., 2011: An increase in the number of tornado reports in Brazil. *Wea., Clim., and Soc.*, **3**, 209–217.

Doswell, C. A., H. E. Brooks, and R. A. Maddox, 1996: Flash flood forecasting: An ingredients-based methodology. *Wea. Forecasting*, **11**, 560–581.

Dotzek, N., 2001: Tornadoes in Germany. *Atmos. Res.*, **56**, 233–251.

Dotzek, N., 2003: An updated estimate of tornado occurrence in Europe. *Atmos. Res.*, **67–68**, 153–161.

Duda, J. D. and W. A. Gallus Jr., 2009: Spring and summer severe weather reports over the Midwest as a function of convective mode: A preliminary study. *Wea. Forecasting*, **25**, 190–206, doi:10.1175/2009WAF2222 338.1.

Elsom, D. M., 1985: Tornadoes in Britain: Where, when and how often. *J. Meteor. (UK)*, **10**, 203–211.

Elsom, D. M. and G. T. Meaden, 1984: Spatial and temporal distributions of tornadoes in the United Kingdom 1960-1982. *Weather*, **39**, 317–323, doi:10.1002/j.1477–8696.1984.tb06 727.x.

Elsom, D. M., G. T. Meaden, D. J. Reynolds, M. W. Rowe, and J. D. C. Webb, 2001: Advances in tornado and storm research in the United Kingdom and Europe: The role of the Tornado and Storm Research Organisation. *Atmos. Res.*, **56**, 19–29, doi:10.1016/S0169–8095(00)00 084–3.

Evans, J. S. and C. A. Doswell, 2001: Examination of derecho environments using proximity soundings. *Wea. Forecasting*, **16**, 329–342, doi:10.1175/1520-0434(2001)016⟨0329:EODEUP⟩2.0.CO;2.

Fujita, T., 1955: Results of detailed synoptic studies of squall lines. *Tellus*, **7**, 405–436.

Funk, T. W., K. E. Darmofal, J. D. Kirkpatrick, V. L. DeWald, R. W. Przybylinski, G. K. Schmocker, and Y. J. Lin, 1999: Storm reflectivity and mesocyclone evolution associated with the 15 April 1994 squall line over Kentucky and southern Indiana. *Weather and Forecasting*, **14 (6)**, 976–993.

Gallus Jr., W. A., N. A. Snook, and E. V. Johnson, 2008: Spring and summer severe weather reports over the Midwest as a function of convective mode: A preliminary study. *Wea. Forecasting*, **23**, 101–113, doi:10.1175/2007WAF2006 120.1.

Gayà, M., 2011: Tornadoes and severe storms in Spain. *Atmos. Res.*, **100**, 334–343.

Glickman, T. S., 2000: *Glossary of Meteorology*. 2nd ed., American Meteorological Society.

Goliger, A. M. and R. V. Milford, 1998: A review of worldwide occurrence of tornadoes. *J.of Wind Engineeri. and Ind. Aero.*, **74–76**, 111–121.

Grams, J. S., R. L. Thompson, D. V. Snivley, J. A. Prentice, G. M. Hodges, and L. J. Reames, 2012: A climatology and comparison of parameters for significant tornado events in the United States. *Wea. Forecasting*, **27**, 106–123, doi:10.1175/WAF–D–11–00 008.1.

Hagos, S., Z. Feng, C. D. Burleyson, K.-S. S. Lim, C. N. Long, D. Wu, and G. Thompson, 2014: Evaluation of convective-permitting model simulations of cloud populations associated with the Madden-Julian Oscillation using data collected during the AMIE/DYNAMO field campaign. *Geophys. Res. Atmos.*, **119**, 12,052–12,068, doi:10.1002/2014JD022 143.

Hobbs, P. V. and P. O. G. Persson, 1982: The mesoscale and microscale structure and organization of clouds and precipitation in midlatitude cyclones. Part V: The substructure of narrow cold-frontal rainbands. *J. Atmos. Sci.*, **39**, 280–295, doi:10.1175/1520–0469(1982)039<0280:TMAMSA>2.0.CO;2.

Holden, J. and A. Wright, 2004: UK tornado climatology and the development of simple prediction tools. *Quart. J. Roy. Meteor. Soc.*, **130**, 1009–1021, doi:10.1256/qj.03.45.

Hong, S.-Y. and J.-O. J. Lim, 2006: The WRF single-moment 6-class microphysics scheme (WSM6). *J. Korean Meteor. Soc.*, **42**, 129–151.

Hong, S. Y., Y. Noh, and J. Dudhia, 2006: A new vertical diffusion package with an explicit treatment of entrainment processes. *Mon. Wea. Rev.*, **134**, 2318–2341, doi:10.1175/MWR3199.1.

Houze, R. A., P. V. Hobbes, K. R. Biswas, and W. M. Davis, 1976: Mesoscale rainbands in extratropical cyclones. *Mon. Wea. Rev.*, **104**, 868–878.

Janjić, Z. I., 1994: The step-mountain Eta coordinate model: Further developments of the convection, viscous sublayer, and turbulence closure schemes. *Mon. Wea. Rev.*, **122**, 927–945, doi:10.1175/1520–0493(1994)122<0927:TSMECM>2.0.CO;2.

Johns, R. H. and C. A. I. Doswell, 1992: Severe local storms forecasting. *Wea. Forecasting*, **7**, 588–612.

Jorgensen, D. P., Z. Pu, P. O. G. Persson, and W. K. Tao, 2003: Variations associated with cores and gaps of a Pacific narrow cold frontal rainband. *Mon. Wea. Rev.*, **131**, 2705–2729, doi:10.1175/1520–0493(2003)131<2705:VAWCAG>2.0.CO;2.

Kawashima, M., 2011: Numerical study of horizontal shear instability waves along narrow cold frontal rainbands. *J. Atmos. Sci.*, **68**, 878–903, doi:10.1175/2010JAS3599.1.

Kirk, P., 2007: UK tornado climatology 1980–2004. *Int. J. Meteor.*, **32**, 158–172.

Kirk, P. J., 2014: An updated tornado climatology for the UK: 1981–2010. *Weather*, **69**, 171–175, doi:10.1002/wea.2247.

Klemp, J. B. and R. Rotunno, 1983: A study of the tornadic region within a supercell thunderstorm. *J. Atmos. Sci.*, **40**, 359–377.

Kron, W., M. Steuer, P. Löw, and A. Wirtz, 2012: How to deal properly with a natural catastrophe database - analysis of flood losses. *Nat. Haz. and Earth Syst. Sci.*, **12**, 535–550.

Lacy, R. E., 1968: Tornadoes in Britain during 1963-6. *Weather*, **23**, 116–124.

Lee, B. D. and R. B. Wilhelmson, 1997a: The numerical simulation of non-supercell tornadogenesis. part I: Initiation and evolution of pretornadic misocyclone circulations along a dry outflow boundary. *J. Atmos. Sci.*, **54**, 32–60, doi:10.1175/1520–0469(1997)054<0032:TNSONS>2.0.CO;2.

Lee, B. D. and R. B. Wilhelmson, 1997b: The numerical simulation of nonsupercell tornadogenesis. Part II: Evolution of a family of tornadoes along a weak outflow boundary. *J. Atmos. Sci.*, **54**, 2387–2415.

Lee, B. D. and R. B. Wilhelmson, 1997c: The numerical simulation of nonsupercell tornadogenesis. Part III: Parameter tests investigating the role of CAPE, vortex sheet strength, and boundary layer vertical shear. *J. Atmos. Sci.*, **57**, 2246–2261, doi:10.1175/1520–0469(2000)057<2246:TNSONT>2.0.CO;2.

Lemon, L. R. and C. A. Doswell, 1979: Severe thunderstorm evolution and mesocyclone structure as related to tornadogenesis. *Mon. Wea. Rev.*, **107**, 1184–1197.

Mahoney, K. M., G. M. Lackmann, and M. D. Parker, 2009: The role of momentum transport in the motion of a quasi-idealized mesoscale convective system. *Mon. Wea. Rev.*, **137**, 3316–3338.

Markowski, P., E. Rasmussen, J. Straka, R. Davies-Jones, Y. Richardson, and R. J. Trapp, 2008: Vortex lines within low-level mesocyclones obtained from pseudo-dual-Doppler radar observations. *Mon. Wea. Rev.*, **136**, 3513–3535, doi:10.1175/2008MWR2315.1.

Markowski, P. and Y. Richardson, 2014: What we know and don't know about tornado formation. *Physics Today*, **67**, 26–31, doi: 10.1063/PT.3.2514.

McAvoy, B. P., W. A. Jones, and P. D. Moore, 2000: Investigation of an unusual storm structure associated with weak to occasionally strong tornadoes over the eastern United States. *Preprints, 20th Severe Local Storms Conference, Orlando, FL*, Amer. Meteor. Soc., 182–185.

Meaden, G. T., 1985a: *A study of tornadoes in Britain with assessments of the general tornado risk potential and the specific risk potential at particular regional sites.* TORRO, and Health and Safety Executive, H.M. Nuclear Installations Inspectorate, Bradford-on-Avon, UK.

Meaden, G. T., 1985b: TORRO, The Tornado and Storm Research Organization: The main objectives and scope of the network. *J. Meteor. (UK)*, **10**, 182–185.

Meaden, G. T. and C. R. Chatfield, 2007: Tornadoes in Birmingham, England, in 1931 and 1946–2005, and inferences about Britain's tornado climatology. *4th European Conference on Severe Storms*, Trieste, Italy.

Miles, J. W. and L. N. Howard, 1964: Note on a heterogeneous shear flow. *J. Fluid Mech.*, **20**, 331–336.

Minor, J. E., R. E. Peterson, and R. S. Lourensz, 1980: Characteristics of Australian tornadoes. *Aust. Meteor. Mag.*, **28**, 57–78.

Morrison, H., G. Thompson, and V. Tatarskii, 2009: Impact of cloud microphysics on the development of trailing stratiform precipitation in a simulated squall line: Comparison of one- and two-moment schemes. *Mon. Wea. Rev.*, **137**, 991–1007, doi:10.1175/2008MWR2556.1.

Norris, J., G. Vaughan, and D. M. Schultz, 2013: Snowbands over the English Channel and Irish Sea during cold-air outbreaks. *Quart. J. Roy. Meteor. Soc.*, **139**, 1747–1761.

Paulikas, M. J., 2014: Examining population bias relative to severe thunderstorm hazard reporting trends in the Atlanta, GA metropolitan region. *Met. App.*, **21**, 494–503, doi:10.1002/met.1394.

Rasmussen, E. N. and D. O. Blanchard, 1998: A baseline climatology of sounding-derived supercell andtornado forecast parameters. *Wea. Forecasting*, **13**, 1148–1164.

Reynolds, D. J., 1999: A revised U.K. tornado climatology, 1960–1989. *J. Meteor. (UK)*, **24**, 290–321.

Rotunno, R. and J. Klemp, 1985: On the rotation and propagation of simulated supercell thunderstorms. *J. Atmos. Sci.*, **42 (3)**, 271–292.

Rowe, M., 1999: 'Work of the devil': Tornadoes in the British Isles to 1660. *J. Meteor. (UK)*, **24**, 326–338.

Setvák, M., M. Šálek, and J. Munzar, 2003: Tornadoes within the Czech Republic: From early Medieval chronicles to the "internet society". *Atmos. Res.*, **67–68**, 589–605.

Shafer, C. M., A. E. Mercer, C. A. Doswell III, M. B. Richman, and L. M. Leslie, 2009: Evaluation of WRF forecasts of tornadic and nontornadic outbreaks when initialized with synoptic-scale input. *Mon. Wea. Rev.*, **137**, 1250–1271, doi: 10.1175/2008MWR2597.1.

Simeonov, P., L. Bocheva, and I. Gospodinov, 2013: On space-time distribution of tornado events in Bulgaria (1956-2010) with brief analyses of two cases. *Atmos. Res.*, **123**, 490–497.

Sioutas, M., W. Szilagyi, and A. Keul, 2013: Waterspout outbreaks over areas of Europe and North America: Environment and predictability. *Atmos. Res.*, **123**, 167–179.

Skamarock, W. C., et al., 2008: A description of the Advanced Research WRF Version 3. Tech. Note TN–475+STR, 113 pp., NCAR.

Smart, D. J. and K. A. Browning, 2009: Morphology and evolution of cold-frontal misocyclones. *Quart. J. Roy. Meteor. Soc.*, **135**, 381–393, doi: 10.1002/qj.399.

Smith, B. T., R. L. Thompson, J. S. Grams, C. Broyles, and H. E. Brooks, 2012: Convective modes for significant severe thunderstorms in the contiguous United States. Part I: Storm classification and climatology. *Wea. Forecasting*, **27**, 1114–1135, doi:10.1175/WAF–D–11–00 115.1.

Snow, J. T. and A. L. Wyatt, 1997: Back to basics: The tornado, nature's most violent wind: Part I - World-wide occurrence and categorisation. *Weather*, **52**, 298–304.

Straka, J. M., E. N. Rasmussen, R. P. Davies-Jones, and P. M. Markowski, 2007: An observational and idealized numerical examination of low-level counter-rotating vortices in the rear flank of supercells. *Elec. J. of Severe Storms Meteor.*, **2**, 1–22.

Thompson, G., P. R. Field, R. M. Rasmussen, and W. D. Hall, 2008: Explicit forecasts of winter precipitation using an improved bulk microphysics scheme. Part II: Implementation of a new snow parameterization. *Mon. Wea. Rev.*, **136**, 5095–5115, doi:10.1175/2008MWR2387.1.

Thompson, R. L., B. T. Smith, J. S. Grams, A. R. Dean, and C. Broyles, 2012: Convective modes for significant severe thunderstorms in the contiguous United States. part II: Supercell and QLCS tornado environments. *Wea. Forecasting*, **27 (5)**, 1136–1154.

Trapp, R. J., E. D. Mitchell, G. A. Tipton, D. W. Effertz, A. I. Watson, D. L. Andra Jr., and M. A. Magsig, 1999: Descending and nondescending tornadic vortex signatures detected by WSR-88Ds. *Wea. Forecasting*, **14**, 625–639.

Trapp, R. J., S. A. Tessendorf, E. S. Godfrey, and H. E. Brooks, 2005: Tornadoes from squall lines and bow echoes. Part I: Climatological distribution. *Wea. Forecasting*, **20**, 23–34, doi:10.1175/WAF–835.1.

Trapp, R. J. and M. L. Weisman, 2003: Low-level mesovortices within squall lines and bow echoes. Part II: Their genesis and implications. *Mon. Wea. Rev.*, **131**, 2804–2823.

Tyrrell, J., 2003: A tornado climatology for Ireland. *Atmos. Res.*, **67-68**, 671–684, doi:10.1016/S0169–8095(03)00 080–2.

Wakimoto, R. M. and J. W. Wilson, 1989: Non-supercell tornadoes. *Mon. Wea. Rev.*, **117**, 1113–1140, doi:10.1175/1520–0493(1989)117<1113:NST>2.0.CO;2.

Weisman, M. L. and C. A. Davis, 1998: Mechanisms for the generation of mesoscale vortices within quasi-linear convective systems. *J. Atmos. Sci.*, **55**, 2603–2622.

Weisman, M. L. and J. B. Klemp, 1982: The dependence of numerically simulated convective storms on vertical wind shear and buoyancy. *Mon. Wea. Rev.*, **110**, 504–520.

Wheatley, D. M. and R. J. Trapp, 2008: The effect of mesoscale heterogeneity on the genesis and structure of mesovortices within quasi-linear convective systems. *Mon. Wea. Rev.*, **136**, 4220–4241, doi:10.1175/2008MWR2294.1.

Widen, H. M., et al., 2013: Adjusted tornado probabilities. *E. J. Severe Storms Met.*, **7**, 1–12.